Chair of Metal Forming

Doctoral Thesis

Investigation of the deformation and fracture behaviour of two steel grades under cold heading conditions

Dipl.-Ing. Philipp Stögner, BSc

November 2021

MONTANUNIVERSITÄT LEOBEN
www.unileoben.ac.at

EIDESSTATTLICHE ERKLÄRUNG

Ich erkläre an Eides statt, dass ich diese Arbeit selbständig verfasst, andere als die angegebenen Quellen und Hilfsmittel nicht benutzt, und mich auch sonst keiner unerlaubten Hilfsmittel bedient habe.

Ich erkläre, dass ich die Richtlinien des Senats der Montanuniversität Leoben zu "Gute wissenschaftliche Praxis" gelesen, verstanden und befolgt habe.

Weiters erkläre ich, dass die elektronische und gedruckte Version der eingereichten wissenschaftlichen Abschlussarbeit formal und inhaltlich identisch sind.

Datum 01.11.2021

Unterschrift Verfasser/in
Philipp Stögner

Acknowledgements

First, I wish to express my gratitude to my girlfriend Melanie Leitner for her patience and her strong support during the periods of hard work and difficult times during the project. I want to thank her for lots of fruitful discussions, which helped shape this work as well as my perspective in life.

Further, I would like to thank my supervisors, Prof. Bruno Buchmayr and Prof. Martin Stockinger from the Chair of Metal Forming for their support during the project and their confidence in me and my work. It saddens me that, due to his untimely death, Prof. Buchmayr can no longer witness the completion of this work.

I also want to thank my mentor Prof. Reinhold Ebner and my supervisors Dr. Marina Lukas and Dr. Gerald Ressel of the Materials Center Leoben (MCL) for supporting me with their knowledge. Their advice was invaluable for realizing this work.

Special thanks are owed to my colleagues from the Chair of Metal Forming, Andreas Schwarz and Clemens Cislo for the discussions and insights I gained. Furthermore, the assistance received by Ralph Ambrosch and Christian Stöckl is highly appreciated.

Moreover, I also want to thank my family for their continued support and confidence in my way of life.

Finally, I would like to thank voestalpine Wire Rod GmbH, especially Dr. Matthew Galler and Dr. Peter Gruber for the provision of materials as well as technical advice during the project. Further, I would like voestalpine Forschungsservicegesellschaft (FSG) for their support.

This work was made possible under the scope of the COMET program within the K2 Center „Integrated Computational Material, Process and Product Engineering (IC-MPPE)“. This program is supported by the Austrian Federal Ministries for Transport, Innovation and Technology (BMVIT) and for Digital and Economic Affairs (BMDW), represented by the Austrian research funding association (FFG), and the federal states of Styria, Upper Austria and Tyrol.

Abstract

The cold heading of steels is an important process in the manufacturing of screws and high strength fasteners. Therefore, it is vital to characterise the forming behaviour of low-alloyed steels, the class of materials deployed, under the predominant multiaxial stress states. The aim of this work is to describe the influences on the formability of two selected materials, a precipitation hardening ferritic-pearlitic steel, 27MnSiVS6, in as-rolled condition, and a quenching and tempering steel, 42CrMo4, annealed. In a first step, the forming behaviour is investigated on a sub-grain level using in-situ tensile testing with deformation examined using a SEM and novel digital image correlation (DIC) methods. This setup allowed a depiction of the localization of strain and deformation on a microstructural level. To complement the influence of the microstructure on formability, an application-oriented testing method is developed. This setup, which models the final heading step during industrial production of screws and fasteners, the cold heading test (CHT), is used to quantify the influence of stress-state on the deformation and damaging behaviour. The experiments are supported by a finite element (FE) simulation of the CHT to predict the damage accumulation and multiaxial stress state during forming. The combination of the aforementioned methods, as well as the high accuracy of the application-oriented testing setup concerning influences on workability enable a thorough characterisation of the influences on formability and the damaging behaviour of low-alloyed steels.

Kurzzusammenfassung

Das Kaltfließpressen ist ein wichtiger Prozess in der Herstellung von Schrauben und anderen hochfesten Verbindungselementen. Aus diesem Grund ist es von Bedeutung die Umformbarkeit von niedriglegierten Stählen unter den vorherrschenden mehrachsigen Spannungszuständen zu untersuchen. Das Ziel dieser Arbeit ist die Beschreibung der Einflüsse auf das Umformverhalten von zwei ausgewählten Werkstoffen, einem ausscheidungshärtenden ferritsch-perlitischem (AFP) Stahl, 27MnSiVS6, in walzhartem und einem Vergütungsstahl, 42CrMo4 in weichgeglühtem Zustand. In ersten Untersuchungen wird das Werkstoffverhalten auf mikrostruktureller Ebene mit Hilfe von in-situ Zugversuchen betrachtet. Die auftretenden Verformungen werden mittels neuartiger digitaler Bildverarbeitungsmethoden in einem REM aufgezeichnet und analysiert. Diese Versuche erlauben die Beschreibung von lokal auftretenden Spannungen und Dehnungen im Gefüge des untersuchten Werkstoffs. In Kombination zu den Untersuchungen des Werkstoffverhaltens auf mikrostruktureller Ebene wurde ein anwendungsnaher Versuchsaufbau zur Untersuchung des Einflusses des globalen Spannungszustandes auf die Umformbarkeit während des Kopfstauchens, der „Cold heading test“ (CHT), entwickelt. Dieser Versuch wurde mittels Massivumformsimulation nachgebildet um in Kombination mit den experimentellen Ergebnissen den Fortschritt der Schädigung und des mehrachsigen Spannungszustandes während der Umformung zu beschreiben. Die Verbindung aus standardisierten Methoden und anwendungsnahen Umformexperimenten mit Hilfe eines neuentwickelten Versuchsaufbaus erlauben eine grundlegende Beschreibung der Einflüsse auf die Umformbarkeit sowie das Verformungs- und Schädigungsverhalten von niedriglegierten Stählen.

Contents

1. Introduction

For thousands of years, steel and ferrous alloys, due to the variety of material properties, have been used in a broad field of applications. With the first known usages for weapons and decorative objects in 1500 B.C. to modern industrial applications such as the production of e.g. high performance steels for automotive parts or the manufacturing of high strength screws and fasteners [1]. An exemplary production process can be described by the route of raw iron processing by blast furnace, followed by secondary metallurgy in a steel mill, where the required steel quality is achieved by deoxidation and desulphurization procedures and alloying with elements such as Si, Mn, Cr and Ni [1–4]. Semi-finished products are then either produced by static casting or continuous casting processes of slabs, blooms or billets followed up by hot rolling processes. Intermediary products range from heavy and coiled sheet metal with thickness up to 25 mm to wire rods with diameters from 3,5 to 60 mm [1; 3; 5; 6]. On the basis of sheet metal or wire rods, finished products are fabricated by a broad range of hot and cold manufacturing processes, such as forging, rolling, heading or drawing. [7]

An important example is the manufacturing of screws and fasteners using cold heading. Due to high requirements concerning productivity as well as geometric and surface quality, cold forging and forming processes present an economic method of bulk forming [8]. This procedures have many advantages, for example reduced waste, realisation of complex shapes during forming operations as well as increased material strength due to cold working effects [9; 10]. An exemplary bolt manufacturing process using cold forming processes is shown in Figure 1. After shearing a piece from the wire rod (1), the material is fed into the first die (2) and roughly formed in a first upsetting step (3). The second and final deformation procedure is conducted after exchanging the heading die (4, 5) before the finished part is ejected from the main die (6). The number of forming steps depends on the complexity of the manufactured part and the strength of the material used. [11] Suitable for cold forming processes, e.g. the manufacturing of screws and fasteners, are all ductile metals such as carbon steels, aluminium and copper [7].

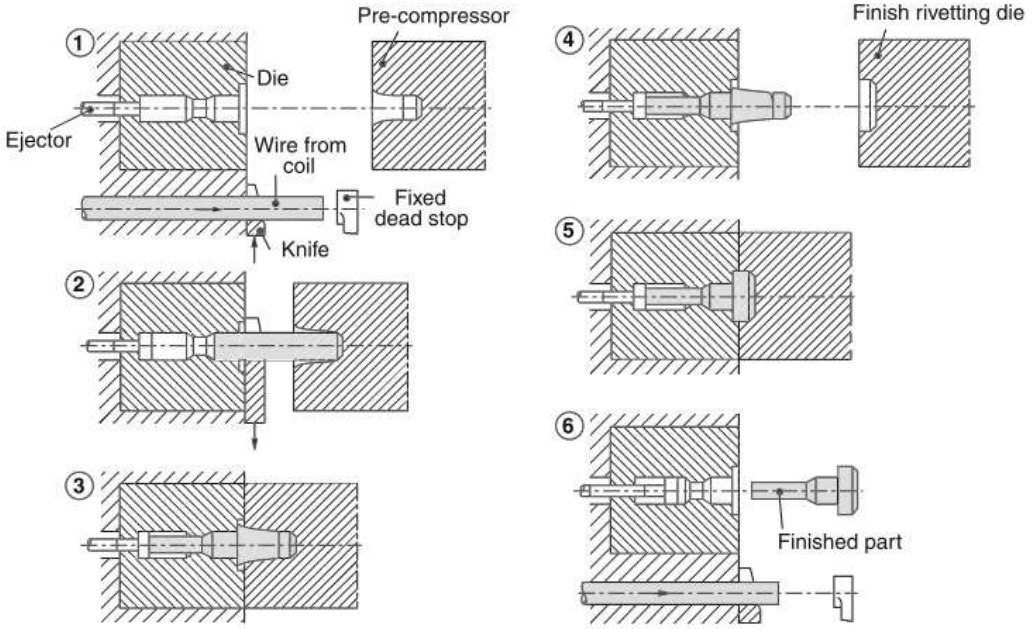

Figure 1: Example of a bolt manufacturing process using cold upsetting [11]

As can be seen in Figure 1, cold forming or heading operations are comprised of multiple forming steps, with each step increasing the dislocation density inside the material, leading to effects of strain hardening [11; 12]. The high degree of deformation at the head of the workpiece during finishing steps (4, 5) combined with work hardening effects may lead to internal and external crack formation and ultimately to ductile failure. Therefore, workability testing methods for materials intended for the use in cold forming have been developed. To investigate the formability of materials, standard methods are tensile or upsetting tests of cylindrical specimen with different length to diameter ratios [13; 14]. These standard methods enable an assessment of the deformation behaviour as well as the friction and stress states during forming operations. In recent decades, characterization of material behaviour during forming has been achieved through a combination of standard testing methods and finite element (FE) simulation. With these combined methods, depiction of workability at different stress states has been enabled [15–17].

However, the approach for investigation of formability behaviour of materials has been realized either through using standard testing methods combined with simulation of the material behaviour or by the usage of a specialized forming process [18–20]. Therefore, the main objective of this work is to determine the behaviour of cold heading steels during deformation on a microscopic scale and comparison of the results with a scaled up, application-oriented testing method. For this purpose, the selected materials are investigated using standard testing methods, in this case tensile testing, as well as a newly developed, application-oriented testing which depicts the final deformation step during the production of screw and fasteners, i.e., the cold heading test (CHT). This method enables evaluation of the influence of multi-axial stress

states on the deformation behaviour during radial extrusion and reproduces the final step of cold forming in industrial applications (comparable to step 5 in Figure 1). For evaluation of the microstructural workability, a novel approach using digital image correlation (DIC) methods during in-situ tensile tests to investigate the localisation of deformation, for example at grain boundaries, is used. These two methods enable a direct depiction of the formability of selected materials from microscopic to macroscopic level.

2. Literature study and state of the art

In the manufacturing of finished products, for example screws or fasteners, the process of cold heading plays an important role due to its wide range of applicable materials [8]. As it is possible to produce complex geometries, investigation of the forming behaviour of materials under multi-axial stress states is essential for the design of industrial forming processes. Therefore, formability of metallic materials during cold forming operations plays a key part in a wide range of scientific investigations. To determine the workability, the behaviour of metallic materials during deformation needs to be evaluated. Therefore, an overview over the structure as well as plastic deformation mechanisms of metals is given.

2.1. Behaviour of metals during deformation

The structure of metals and ceramics is defined by the arrangement of atoms in a so called unit cell, which can be classified according to the edge length and angles involved. Seven basic types can be distinguished, cubic, tetragonal, hexagonal, orthorhombic, rhombohedral, monoclinic and triclinic [21]. The structures most common in metals are body-centered cubic (bcc), face-centered cubic (fcc) and hexagonal close-packed (hcp). An overview is shown in Figure 2. Typical materials with bcc-structure are chromium (Cr) or α-iron (α-Fe), with fcc-stucture for example copper (Cu), nickel (Ni) or γ-iron (γ-Fe) [22; 23].

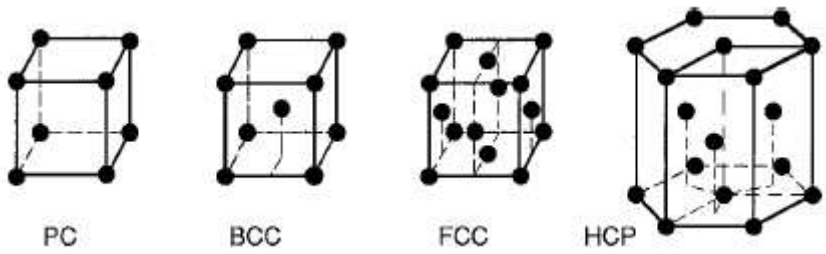

Figure 2: Types of crystal structures most common in metallic materials – primitive cubic (PC), body-centered cubic (bcc), face-centered cubic (fcc) and hexagonal close-packed (hcp) [21]

Polycrystalline engineering materials normally have defects in their crystal structure, which can be classified as point, line and planar defects [24]:

- Point defects: are also called zero-dimensional defects and are for example, substitutional impurities, vacancies or interstitial atoms. These are important for thermally activated processes such as diffusion.
- Line defects: are called dislocations and can be classified into edge dislocations (shown in Figure 3, (a)) and screw dislocations (Figure 3, (b)). These defects enable plastic deformation of materials and therefore are important for the formability.

- Planar defects: are grain and phase boundaries.

These defects play an important role in the plastic deformation behaviour of metallic materials if the external load exceeds the elastic limit.

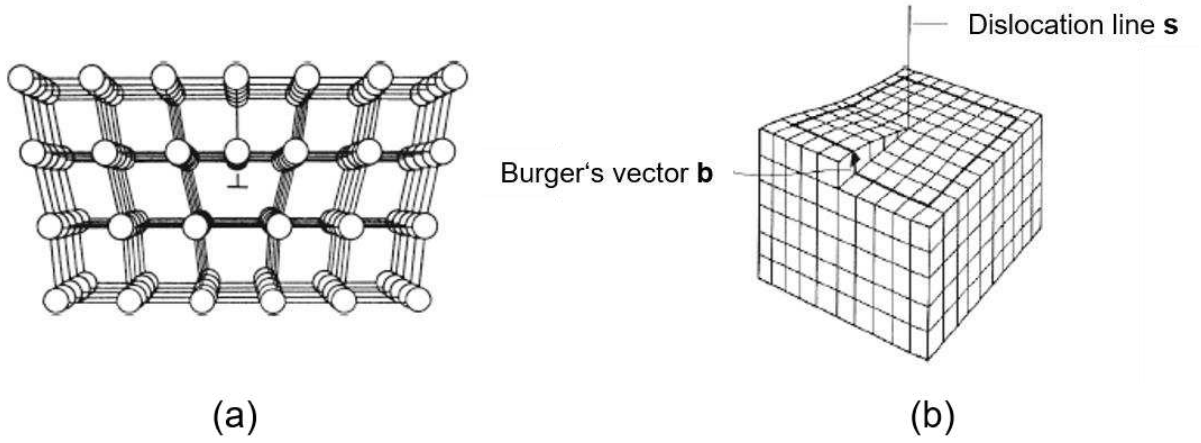

Figure 3: Types of dislocations – (a) edge dislocation, (b) screw dislocation [12]

One of the main plastic deformation mechanisms of metals occurs by dislocation slip due to shear stress. This effect is responsible for the large difference between the theoretical and the actual strength of a metallic material, as plastic deformation proceeds one atom at the time as opposed to simultaneously over the whole plane [21]. The dislocation moves slip planes or slip bands, which can sometimes be examined when these bands intersect the free surface of a material (for example in Figure 48). The preferred slip directions in a plane are called close-packed directions in which the atoms are more closely packed [12; 21]. If forming is conducted at temperatures below recrystallization temperature, as for example in cold heading operations, the material strength increases with increasing strain. This strain hardening is dependent on the crystal structure, as hcp materials are showing a more pronounced increase in strength as e.g. fcc materials [22]. This can lead to problems concerning the susceptibility of failure during forming. Different systematic approaches for characterization of the deformation behaviour have been developed in the past, for example the depiction of the plasticity behaviour on a microstructural level or the influence of different stress states [25; 26].

2.2. Crystal plasticity models

The first thorough description of the deformation of single crystals due to slip was proposed by Taylor & Elam in 1923 investigating the forming behaviour of an Al single crystal during tensile testing [27]. The model was enhanced by Taylor in 1938 to analyse the deformation of a polycrystal composed of a multitude of grains [28]. This considerations for polycrystalline and single crystal materials was adapted into the framework of continuum mechanics by Hill in 1966, which formed the base for different constitutive models describing the plastic deformation of single crystals on a microscopic level. [29]

Crystal plasticity (CP) models are based on the partition of the deformation gradient **F** into elastic $\mathbf{F}^{el}$ and plastic $\mathbf{F}^{pl}$ parts, shown in equation (1):

$$\mathbf{F} = \mathbf{F}^{el}\mathbf{F}^{pl} \tag{1}$$

It is generally accepted for CP that $\mathbf{F}^{pl}$ leaves the crystal lattice undistorted and that only $\mathbf{F}^{el}$ determines the rotation of the crystal lattice, as seen in Figure 4 [30].

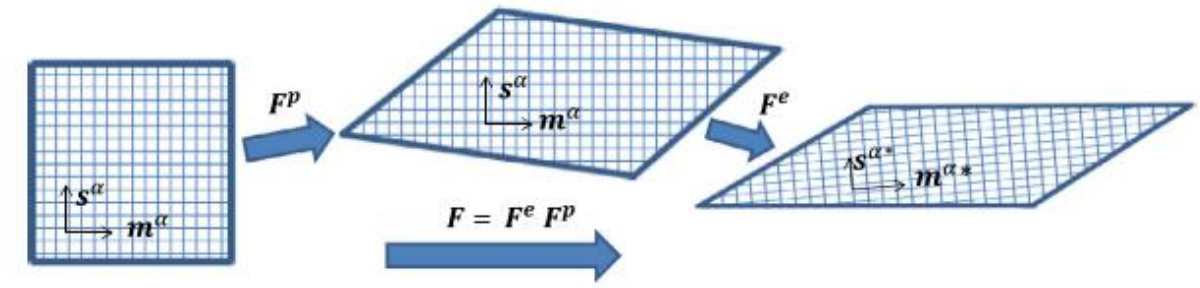

Figure 4: Influence of $\mathbf{F}^{el}$ and $\mathbf{F}^{pl}$ on the crystal lattice during deformation [30]

Considering the crystallographic nature of a single crystal, the plastic deformation is described by two orthogonal unit vectors, which define the slip system *k*, the slip direction $\mathbf{s}^k$ and the slip plane normal $\mathbf{m}^k$. The available slip systems are determined by the crystal lattice, for example *k* = 12 for *fcc* metals. In addition, CP models contain functions, which dictate the shear rate of each slip system $\dot{\gamma}^k$, which consists of the resolved shear stress τ^k and different internal variables ***q***. Examples for internal variables are dislocation density and velocity in the polycrystal. Due to the difference in approaching the modelling of crystal plasticity, four main groups can be differentiated for which an overview will be presented [30]:

- Phenomenological CP models
- Physically based CP models
- Strain gradient CP models
- Twinning CP models

2.2.1. Phenomenological CP-models

This approach is based on classical constitutive equation theory, and internal variables to determine the internal state of the crystal and the evolution laws which are not directly related to microscopical processes [31]. Earlier models were complex due to the fact that different combinations of shear increments lead to the same plastic strain, therefore in more recent formulations, viscoplastic approaches to material behaviour became a widely used alternative [32].

In detail, a set of internal variables **q** contains information about accumulated plastic slip γ^k and critical resolved shear stress (CRSS) g^k in each slip system *k.* If strain hardening is considered, these models were developed for monotonic load and therefore only isotropic

hardening is considered. Overall, in the approach of phenomenological crystal plasticity, three hardening models are the base for monotonic load models developed nowadays: Peirce, Voce hardening law and Bassani and Wu [32–34].

To extend the phenomenological frameworks to account for cyclic deformation, and to formulate kinematic hardening laws, the effect of backstress is introduced in the constitutive models [35]. Therefore, the plastic shear rate γ is a function of CRSS and backstress, which is dependent on slip system and crystallographic state of the material (e.g. fcc). Other expressions of kinematic hardening on the crystal level are based on macroscopic plasticity behaviour of materials, for example the Frederick-Armstrong law adapted by Mèric et al. which takes into account the Bauschinger effect [36].

2.2.2. Physically Based CP-models

These crystal plasticity models contain microscopical physical quantities, e.g. dislocation density, to formulate the mechanisms of plastic deformation on a microscopic scale and therefore initial material quantities have to be taken into account as well. Physically based models are based on the relationship between plastic slip rate γ and dislocation movement during deformation; first deduced by Orowan et al., with resolved shear stress as the driving force for dislocation movement, which is taken into account through the average dislocation velocity [37]. However, if the lattice friction is considered negligible (e.g. in fcc metals), a linear viscous relation between resolved stress and velocity of a single dislocation can be formulated [38].

At low dislocation densities a linear viscous relationship can be established between CRSS and plastic slip rate, but this formulation is valid only if a single dislocation is considered. The average dislocation velocity deviates due to the influence of temperature-dependent and independent barriers which hinder the dislocation movement. This influence of temperature on dislocation movement was studied by Kocks et al., which set the framework for most temperature dependent physically based CP-models [39]. However, these considerations are true only if the lattice friction is not taken into account.

In addition to the influence of temperature on the dislocation velocity during plastic deformation, micromechanical internal variables, such as dislocation densities are taken into account for calculation of the strain hardening behaviour on a microscopical level. This approach for modelling the evolution of dislocation density is based on the Kocks-Mecking model, which describes hardening as a combination of athermal storage at obstacles and temperature dependent annihilation of dislocations due to dynamic recovery [40].

2.2.3. Strain Gradient CP-models

The crystal plasticity models described above are size-independent as the material behaviour at any given point is dependent only on local state and internal variables as there are no length scales involved in the formulation of these models. However, the development of plastic strain heterogeneities in crystal deformation is also the reason behind the dependency of plastic strength of polycrystals on grain size, which was discovered by Hall and Petch [41; 42].

Influence of plastic heterogeneities in the mechanical response of a crystal was described by Nye and Ashby as the interaction between statistically stored dislocations (SSD) and geometrically necessary dislocations (GND) [43; 44]. SSDs evolve from random trapping processes during plastic deformation and GNDs are induced due to the existence of plastic strain gradients. Therefore, strain gradient plasticity models have been developed to account for the effect of plastic strain heterogeneities on deformation behaviour of materials.

Two approaches have been developed, low-order strain gradient plasticity models, which preserve the thermodynamic consistency and high order SGCP, where the internal variables are chosen as kinematic variables [45; 46]. Furthermore, lower-order formulations have the benefit of a simple structure, and therefore an easier implementation into FE codes and the description of size effects during deformation. However the main limitation is the impossibility of accounting for the gradient development due to the presence of grain boundaries in a polycrystal.

2.2.4. Deformation by Twinning

Metals with low symmetry in their crystal structure, e.g. Ti (hcp lattice) show plastic deformation by dislocation slip in combination with twinning, which occurs when not enough slip systems are present in the crystal [47]. Twinning is a two-step process, which consists of the formation of a twin band across a grain and the propagation of the twinned region perpendicular to the twin band plane. Due to the complexity of the twinning process and the large number of crystal planes which appear during the process, the CP framework is based on simplifications using statistical analysis.

In first modelling approaches, mean-field approximation for polycrystal plasticity was used which cannot be included in single crystal formulations. Recently, a model that was able to describe twinning in a single crystal was developed by Kalidindi and has been the base for further developed plasticity models [48].

2.3. Influence of stress state on deformation behaviour

An important influence on the forming behaviour of materials is the stress state during deformation. If an infinitesimal cubic element is viewed, each side is effected by three stresses, one normal stress and two shear stresses. Therefore, the stress state can be described as follows in equation (2) [12]:

$$\boldsymbol{\sigma} = \begin{bmatrix} \sigma_{xx} & \sigma_{xy} & \sigma_{xz} \\ \sigma_{yx} & \sigma_{yy} & \sigma_{yz} \\ \sigma_{zx} & \sigma_{zy} & \sigma_{zz} \end{bmatrix} \tag{2}$$

The shear stresses σ_{xy}, σ_{xz} and σ_{yz} always occur in pairs. If the stress state is characterized in cylindrical coordinates, possible due to the normally axial symmetric nature of cold heading, four of the six shear stresses result as zero, which leads to equation (3) [49]:

$$\boldsymbol{\sigma} = \begin{bmatrix} \sigma_r & 0 & \sigma_{rz} \\ 0 & \sigma_\theta & 0 \\ \sigma_{zr} & 0 & \sigma_z \end{bmatrix} = \begin{bmatrix} \sigma_1 & 0 & 0 \\ 0 & \sigma_2 & 0 \\ 0 & 0 & \sigma_3 \end{bmatrix} \tag{3}$$

The convention is chosen that $\sigma_1 \geq \sigma_2 \geq \sigma_3$. With these principal stresses, the hydrostatic stress state can be calculated as shown in equation (4):

$$\sigma_m = \frac{1}{3}(\sigma_1 + \sigma_2 + \sigma_3) \tag{4}$$

As the hydrostatic stress is invariant of the stress tensor **σ**, it is not affected by shear stresses and therefore does not influence the plastic deformation during forming. Therefore it can be subtracted from the stress tensor, which leads to the stress deviator **s** [24]:

$$\boldsymbol{s} = \begin{bmatrix} \sigma_{xx} & \sigma_{xy} & \sigma_{xz} \\ \sigma_{yx} & \sigma_{yy} & \sigma_{yz} \\ \sigma_{zx} & \sigma_{zy} & \sigma_{zz} \end{bmatrix} - \begin{bmatrix} \sigma_m & 0 & 0 \\ 0 & \sigma_m & 0 \\ 0 & 0 & \sigma_m \end{bmatrix} = \begin{bmatrix} s_{xx} & \sigma_{xy} & \sigma_{xz} \\ \sigma_{yx} & s_{yy} & \sigma_{yz} \\ \sigma_{zx} & \sigma_{zy} & s_{zz} \end{bmatrix} \tag{5}$$

However, the plastic deformation is still dependent on the maximum principal stress. For example, during uniaxial deformation, if $\sigma_1 = k_f$, the material deforms plastically. For multiaxial stress states, an equivalent stress has to be calculated to allow a comparison with uniaxial deformation. The equivalent stress can be calculated, for example, according to the hypothesis of von Mises [50]:

$$\sigma_{V,von\ Mises} = \sqrt{\frac{1}{2}[(\sigma_1 - \sigma_2)^2 + (\sigma_2 - \sigma_2)^2 + (\sigma_3 - \sigma_1)^2]} \tag{6}$$

Therefore it can be assessed that only elastic deformation occurs at $\sigma_V < k_f$, with localised plastic deformation starting at $\sigma_V = k_f$. Considering the influence of stress states on maximum formability of materials, an overview is given by the work of Stenger [51]. Different types of testing setups and sample geometries have been investigated concerning the effect of stress

states on the deformation behaviour of materials until the onset of failure. The result of this investigation is described in the Stenger-diagram shown in Figure 5. The description of the stress state during deformation can be evaluated as the influence of the hydrostatic stress state σ_m in relation to the flow stress k_f. This relationship is designated as the triaxiality η [24; 51]. The value of η is dependent on the sample geometry and the type of load applied to the specimen. For example, the triaxiality value for a smooth round bar during uniaxial tensile testing is calculated with $\eta = 0{,}33$. This value increases with the onset of necking or crack formation during testing [52]. At uniaxial compression stresses, the value is determined with $\eta = -0{,}33$. This concludes that, the maximum formability until the onset of failure increases with lower triaxiality values [24].

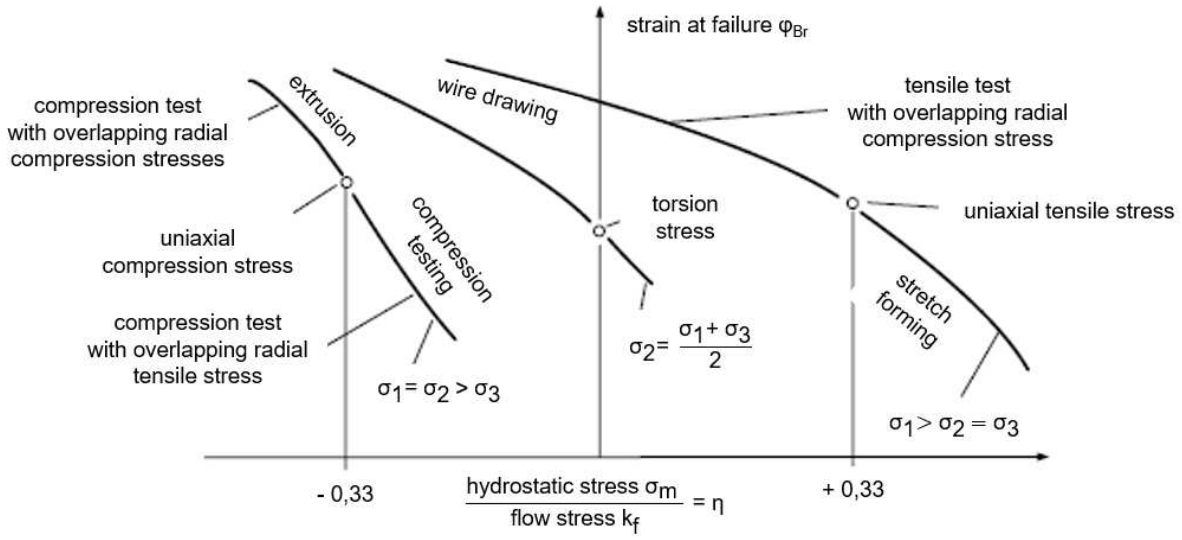

Figure 5: Stenger-diagram – influence of stress state on formability [51]

Many experimental procedures have been conducted, which confirm the findings of Stenger concerning the influence of stress state. For example, the influence of compressive stresses applied to the surface during compression testing was investigated by Pugh [53]. The experiments showed an increase in maximum formability until the onset of cracking of the sample. Furthermore, the influence of specimen geometry on the maximum strain at failure was also taken into account during compression testing [14; 54].

In recent years, the investigation of the forming behaviour of materials under more application-oriented experimental setups has been of interest. This is due to the complex stress states, which occur during the production of, for example, gear parts or fasteners [15; 55–59]. In these investigations, the material behaviour during lateral and radial extrusion and injection processes was examined with the help of experimental setups as well as finite element analysis. The influence of initial sample dimensions, gap height of the extruded parts and friction parameters between specimen and die at the maximum force required for forming, the

flow behaviour and plastic strain distribution were investigated [15]. The finite element analysis was used for a better description of the formability of the material during deformation. A different approach to the investigation of cold forming behaviour was considered by Guk et al [60]. In these experiments, a testing setup that imitates the production step of heading during the production of screws and fasteners has been developed. This setup was used to investigate reproducibility of the material properties after the final forming step. The investigations showed promising results concerning the description of the material behaviour during deformation but has not been pursued further [60].

2.4. Damaging behaviour of materials during deformation

An important part in the description of material behaviour is the occurrence of damage during deformation. If metals are concerned, two main types of failure are described in literature: brittle and ductile failure [61]. Brittle fracture mainly appears as cleavage or intergranular fracture and toughness against fracture is strongly dependent on the size of the investigated specimen [61]. However, many polycrystalline materials loaded with multi-axial stress states typically fail due to ductile fracture. This type of material failure has been investigated using different specimen geometries to influence the stress state during deformation [62].

Ductile damage in plastically deformed materials appears either due to void coalescence or due to mechanical instability of the specimen and shear localisation [61]. The underlying mechanism of ductile damage is, in both cases, the formation of voids and micro-cracks in the metal matrix initiated by local stress concentrations. Therefore, the process of ductile damage can be classified in the following three phases: nucleation, growth and coalescence of voids [63]. The process is shown in Figure 6.

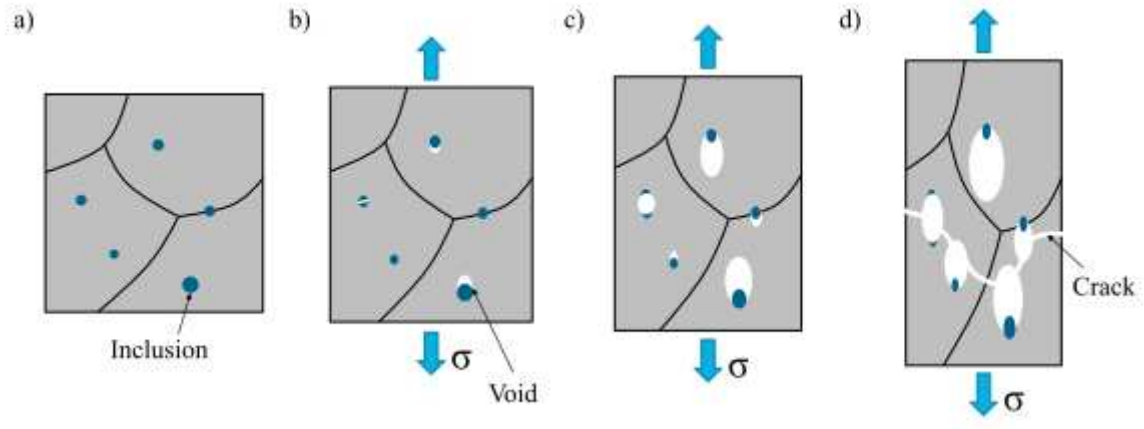

Figure 6: Phases of ductile fracture – (a) initial state, (b) void formation, (c) void growth, (d) void coalescence and cracking [63]

In the first step, the nucleation of voids at non-metallic inclusions (NMI) or phase boundaries play a role in the formation of these micro-cavities. This can be described by two initial processes. Firstly, decohesion of the boundary between matrix material and inclusion can occur, typically through multiaxial tensile loads. Secondly, the fracture of NMI can occur due to high compressive loads [10; 64]. The second step, the growth of nucleated voids, is dependent on the stress state inside the workpiece, namely the stress triaxiality *T*, calculated with equation (7):

$$\boldsymbol{T} = \frac{\boldsymbol{\sigma_m}}{\boldsymbol{\sigma_V}} = \frac{\frac{(\sigma_1+\sigma_2+\sigma_3)}{3}}{\frac{1}{\sqrt{2}}\sqrt{(\sigma_1-\sigma_2)^2+(\sigma_2-\sigma_3)^2+(\sigma_3-\sigma_1)^2}} \tag{7}$$

The triaxiality value *T* is comparable to the factor *η* calculated in the Stenger-diagram. The most prominent forms of void growth during different stress states is shown in Figure 7. Under combined tensile and compressive stresses with triaxiality T ≥ 1, uniform void growth is predominant. In the case of uniaxial loading, voids grow in the direction of the highest principal stress.

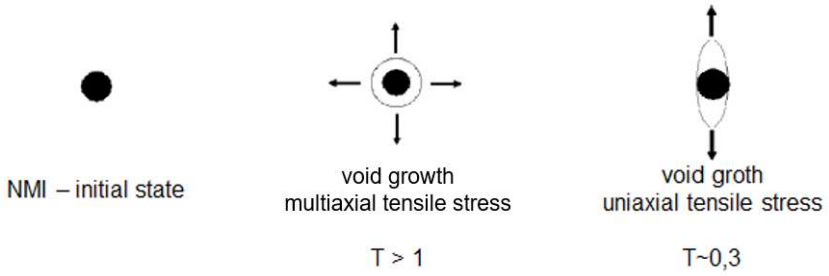

Figure 7: Void growth under different multi-axial stress states [10]

The third and final step of ductile damage is the coalescence of voids, as shown in Figure 6. Two main occurrences of coalescence are described in literature. Firstly, necking of the areas between the voids, which leads to the formation of sharp edges connecting the formed dimples at the fracture surface. Secondly, void sheet coalescence can occur, which connects the defects along shear bands over greater distances inside the metal matrix [62; 63]. As the formed micro-cavities grow during deformation, the section resisting the deformation reduces which finally leads to ductile failure of the material.

Due to the influences on the deformation the prediction of ductile damage behaviour is important for the design of new materials as well as production processes. Numerous criteria for the prediction of ductile failure have been presented, but it is of importance to select appropriate damage models dependent on the type of forming process and stress state. Overall, the mathematical approaches for the prediction of material failure can be divided into two main classes [65]:

- Macro-mechanical models: these models are used to describe the influence of global stresses and strains and include the main factors influencing the formation of damage, the equivalent stress σ_V and the principal stresses. Examples for this models are the Cockroft-Latham, Ayada and Freudenthal criteria [66–68].
- Micro-mechanical models: these models are developed to describe the crack initiation as well as propagation based on the methodology of ductile fracture, as described above. Examples for this criteria are the Oyane, Lemaitre, McClintock and Gurson-Tvergaard-Needleman (GTN) models [69–72].

2.4.1. Macro-mechanical damage criteria

The main focus of the macro-mechanical damage models is the consideration of the previous deformation, which happened to the material. This is achieved by the integration of process dependent local state variables, e.g. the principal stress at a given time, over the measured strain. With this methodology, the plastic strain which is present at the initiation of failure of a material can be calculated. One of the most prominent models for the macro-mechanical calculation of damage behaviour was proposed by Cockroft et al. in 1968 and is shown in equation (8) [66].

$$D_{C-L} = \int_0^{\varphi_{V,F}} \sigma_{1,max} d\varphi_{V,F} \tag{8}$$

with $\sigma_{1,max}$ being the maximum principal tensile stress and $\varphi_{V,F}$ the equivalent strain at fracture. Therefore, considering this approach, the maximum formability of a material is achieved, when the maximum principal stress reaches a critical, positive value. The second and third principal stresses, however, are not taken into account with this approach, which leads to a limitation of possible applications. To achieve a better account of the damaging behavior, the Cockroft-Latham criterion has been optimized numerous times, with the most used iteration presented by Chen et al. in 1979, which is shown in equation (9) [73]:

$$D_{C-L,modified} = \int_0^{\varphi_{V,F}} \frac{\sigma_1}{\sigma_V} d\varphi_{V,F} \tag{9}$$

with σ_V being the equivalent stress during deformation. This modification increases the accuracy of the calculations but the focus on the maximum principle stress still limits the applicability of this damage criterion.

Another important ductile damage model was proposed by Ayada et al in 1984 [67]. The main focus was to better describe the material behaviour during multiaxial stress states. Therefore, instead of the specification of the maximum principle stress σ_1 as the main influence on damage propagation, the hydrostatic stress state σ_m is taken into account. The formulation of the Ayada damage criterion is shown in equation (10):

$$D_{Ayada} = \int_0^{\varphi_{V,F}} \frac{\sigma_m}{\sigma_V} d\varphi_{V,F} \quad (10)$$

This hypothesis delivers more accurate depictions of the damage behaviour during deformation, especially with multi-axial stress states, e.g. cold heading operations. However, a major disadvantage of the macro-mechanical damage modelling is the lacking consideration of material behaviour during deformation, as only the simulated stresses and strains are taken into account [65]. The actual process of ductile fracture, the nucleation, growth and coalescence of voids is not considered in these criteria. These processes are observed with the use of micro-mechanical ductile damage criteria.

2.4.2. Micro-mechanical ductile damage criteria

The focus of the micro-mechanical fracture models mainly lies on the nucleation of pores in a material due to deformation. Therefore, these criteria are calculated using complex plasto mechanical methods. A prominent example for the calculation of damage due to nucleation of voids was proposed by Rice et al in 1969 [74]. In this publication Rice and Tracey show that the influence of nucleation of pores is the main influence in the ductility of a material as opposed to the void geometry. Furthermore it was demonstrated that the hydrostatic stress σ_m has a major influence on the growth of voids and therefore the formability of materials. The damage criterion proposed is shown in equation (11):

$$D_{R-T} = \int_0^{\varphi_{V,F}} exp\left(\frac{3}{2}\frac{\sigma_m}{\sigma_V}\right) d\varphi_{V,F} \quad (11)$$

Another important micro-mechanical damage model was proposed by Oyane et al in 1972 and further modified for different applications in 1980 [69; 75]. This criterion also takes into account the influence of the hydrostatic stress during deformation. To implement the influence of porosity on the formability and damage behaviour, an empirical factor *A*, dependent on the investigated material, is introduced. The formulation of the Oyane criterion is shown in equation (12):

$$D_{Oyane} = \int_0^{\varphi_{V,F}} \left(A + \frac{\sigma_m}{\sigma_V}\right) d\varphi_{V,F} \quad (12)$$

The equation of Ayada is quite similar to the Oyane model, as the former is a simplification of the Oyane criterion, which was proposed earlier. The final micro-mechanical damage model presented, is the Gurson-Tvergaard-Needleman (GTN) criterion, which takes into account the influences of void volume fraction, the yield strengths as well as the process of void nucleation [72]. The influence of the volume fraction of porosities was initially established by Gurson in 1976 [76]. This basic model has been developed and modified by Tvergaard with consideration of the influence of yield condition and damage evolution [77–79]. The influence of void

nucleation on the formability was implemented by Needleman in 1990 [80]. Therefore, the proposed damage criterion is named GTN and is shown in equation (13) [81; 82]:

$$D_{GTN} = \left(\frac{\sigma_V}{R_{p0,2}}\right)^2 + 2q_1 f^* \cdot cosh\left(\frac{3q_2\sigma_m}{2R_{p0,2}}\right) - 1 - q_3 f^{*2} \quad (13)$$

with $R_{p0,2}$ being the yield strength of the matrix material, f^* the modified damage parameter, which takes into account the reduced stress carrying capacity with increasing void volume fractions, and q_1 = 1,5; q_2 = 1 and q_3 = 2,25. These parameters are used as initial parameters and have been calculated in [81]. With this model, the influence of void nucleation can be estimated, however the implementation into finite element (FE) simulation model is difficult and slight variations of parameters can lead to a pronounced difference in calculated damage values.

The macro-mechanical damage models present a simple method of calculating the behaviour of materials at fracture, compared to the micro-mechanical methods. However, the influence of stress states and fracture mechanisms during deformation has to be taken into account. This has been shown by Stögner et al in 2019 [83].

Due to the multiaxial stress state during extrusion of the flange, the Cockroft-Latham criterion shows a wide range of high damage values. This results as only the maximum principal stress σ_1 is taken into account in the calculations. If the micro-mechanical Oyane model is implemented, the results show a more defined area of damage with good alignment with the experimental examinations. This results show the importance of the selection of damage criteria conforming to the deformation process investigated.

2.5. Deformation behaviour of metals on a microstructural level

The forming behaviour of materials on a macroscopic scale is usually conducted using destructive testing methods such as tensile or compression testing [84]. The important material parameters are usually measured using load cells and the strains by measuring the elongation of the specimen during forming. In recent years however, the application of optical measurement systems using digital image correlation (DIC) methods has increased due to the enhancement of measuring equipment and calculation methodology [85–88]. The approach of DIC is the measurement of the shift of a pre-defined grid due to the deformation of the investigated surface. This is shown schematically in Figure 8.

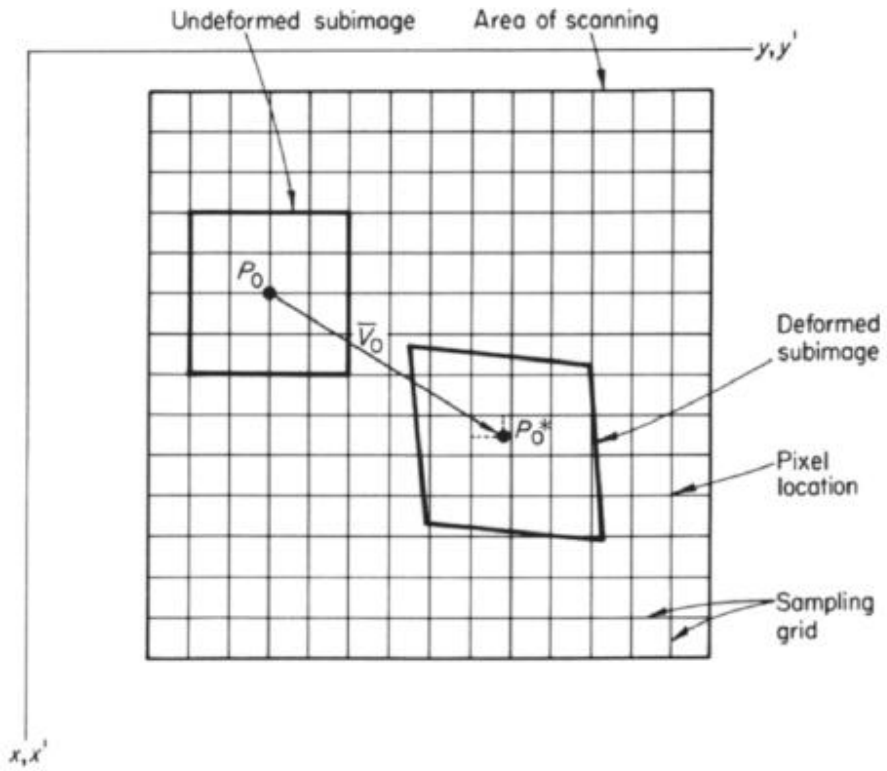

Figure 8: Deformation of a defined geometry (subimage or subset) using DIC [85]

The deformation of the subset can be generally written according to equation (14) [85]:

$$(\boldsymbol{x}')_i = (\boldsymbol{x})_i + (\boldsymbol{u})_i + \frac{\partial[u_i(x)]}{\partial x_j} dx_j \quad i,j = 1,2 \tag{14}$$

with $\boldsymbol{x}'$ being the deformed position of a random point in the subset, $\boldsymbol{u}$ the vector displacement field and $\frac{\partial u_i}{\partial x_j}$ the components of the deformation gradient. With this established correlation method, the deformation of samples during macroscopic tests have been conducted. In recent years, the DIC has been applied for investigations at a microstructural level using, e.g. in-situ tensile tests in a SEM [89–91]. In comparison to standard optical recording devices, for example CMOS cameras, analysis using SEM shows differences in main areas of DIC. For image correlation methods to work properly, a high contrast pattern needs to be applied to the surface. At low magnifications and visible light conditions, typical methods for surface decorations are speckle patterns, applied using paint with high contrast, etching of grids or moiré speckles [86]. At higher magnifications and under conditions using SEM imaging, these established methods cannot be used, as the grain structure and its behaviour during deformation is of interest. Speckle patterns using thick coating are not serviceable for this setup.

Therefore, a wide range of patterning methods has been investigated for plastic strain mapping at a sub-micron resolution [92]. The most widely used methods for application of a pattern, feasible for digital image correlation are [93; 94]:

- Microgrid patterns by photolithography [95]
- Remodelling of thin metallic films [96]
- Nanoparticle deposition techniques [97; 98]

A thorough description of patterning methods for DIC measurements will be presented in chapter 5.

3. Cold forming materials

Materials intended for cold forming are characterized by a low yield stress at the onset of and a low inclination of strain hardening during deformation. This behaviour is obtained by a maximum carbon content of 0,5 wt.% and maximum content of other alloying elements of 3 wt.%. Typical alloying elements are manganese (Mn), chrome (Cr), nickel (Ni) and molybdenum (Mo). Concentrations of sulphur (S) and phosphorus (P) are kept below 35 ppm due to embrittlement of the material [1; 23]. Overall, cold forming steels are categorized into three main groups, with increasing content of C and other alloying elements [1; 99; 100]:

- Carbon steels, for example C8C (C ~ 0,06-0,10 %)
- Case-hardening steels, for example C15 (C ~ 0,12-0,18 %) or 16MnCr5
- Quenched and tempered (Q & T) steels, for example C45 (C ~ 0,42-0,50 %) or 42CrMo4

Carbon steels are used for components with low requirements concerning material strength or corrosion resistance, but higher demands for complex component geometry [1]. Case-hardening steels are deployed for applications needing higher material and fatigue strength. For high demand on material strength, quenched and tempered (Q & T) steels are used, but limitations in material forming behaviour have to be considered due to the increased carbon and alloying element content. Therefore, different types of heat treatment are applied to enable cold forming operations with a quenching and tempering process applied after deformation to increase material strength. Ultimate tensile stress (R_m) and reduction of area (Z) values for typical cold heading steels are shown in Table 1. [1; 23]

Table 1: UTS and reduction of area of typical cold forming steel types [1]

Category	Steel grade	annealed		strain-hardened	
		R_m [MPa]	Z [%]	R_m [MPa]	Z [%]
Carbon steel	C8C	360	75	470	66
Case-hardening steel	C15	430	65	570	56
	16MnCr5	550	62	660	59
Q & T – steel	C45	600	60	720	-
	42CrMo4	630	58	650	58

As shown in chapter 1, the cold forming process is widely used in the production of screws and fasteners. For applications with lower requirements concerning material strength, unalloyed carbon steels are widely used. If high material strength is required, Q & T-steels present a feasible option, due to the possibility of adjusting the strength and ductility of the product through heat treatment. Overall, screws and fasteners are categorized into strength classes

by the technical standard DIN EN ISO 898-1 [101]. An exemplary display of the classification is shown in Table 2.

Table 2: Categorization of screws and fasteners (DIN EN ISO 898-1) [101]

Material property	**Strength class**				
	4.8	**5.8**	**8.8**	**10.9**	**12.9**
R_m [MPa]	400	500	800	1000	1200
R_{eH} [MPa]	240	300	640	900	1080
A [%]	22	20	12	9	8

The standard strength for applications under higher loads, for example in mechanical engineering or the automotive industry, is the 8.8 material class. To reach higher strength classes with the aforementioned cold forming steels, an increasing number of time and energy consuming production steps, like heat treatments before and after deformation are required [23]. Therefore, optimizations concerning the chemical composition are necessary. A promising approach to reach strength classes of 10.9 and higher is the precipitation hardening of ferritic-pearlitic steels by alloying with Nb, Ti or V [23]. Examples for precipitation hardened ferritic-pearlitic (PH-FP) steels are 46MnSV3 or, if higher ductility is needed, 27MnSiVS6 with a reduced carbon content [23; 102]. In this work, two steel types intended for cold heading operations, the Q & T-steel 42CrMo4, in annealed condition and the PH-FP steel 27MnSiVS6 in as-rolled condition are investigated using standard testing methods such as tensile testing and newly developed approach, such as the cold heading test (CHT). The two materials are specified in detail in the following chapter.

3.1. Overview of the investigated materials

The steel grades chosen for this project are the quenched and tempered (Q & T) steel 42CrMo4, in annealed condition and the precipitation hardening ferritic-pearlitc (PH-FP) steel 27MnSiVS6 in as-rolled condition. These two types represent the main material group used for the manufacturing of high strength screws and fasteners with strength classes of 8.8 and above. The steel batches used for this project were delivered as wire rods with diameters of *d = 17,5 mm* for 27MnSiVS6 and *d = 22 mm* for 42CrMo4 and cut into segments with *l = 1000 mm*. From these rods, all specimen for the following experiments were machined at the Chair of metal forming at the MUL.

In the following Table 3, the composition of the two steels as well as the main material properties, determined using tensile testing with circular specimen according to standard DIN 50125 (ISO 6892-1), method B, are shown [103].

Table 3: Overview of the composition and tensile properties of the investigated materials

Material	C wt%	Si wt%	Mn wt%	P wt%	S wt%	Cr wt%	Ni wt%	Mo wt%	V wt%	B wt%	Fe wt%
27MnSiVS6	0,30	0,68	1,25	0,01	0,02	0,15	0,04	0,00	0,12	0,000	97,35
42CrMo4	0,40	0,07	0,80	0,01	0,01	1,04	0,03	0,18	0,00	0,000	97,46

Material	$R_{p0,2}$ [MPa]	UTS [MPa]	A_g [%]	A [%]	GS_{LIMI} [µm]	GS_{EBSD} [µm]
27MnSiVS6	546	780	11,5	23,3	5,9	3,7
42CrMo4	360	561	13,2	28,2	annealed	1,5

Figure 9 shows a comparison of the mean values of the tensile tests two investigated materials. The influence of the annealing of the Q&T steel, reduced strength and higher ductility, can clearly be seen. Compression testing, conducted using a Servotest Thermo-mechanichal testing system (TMTS), as seen in Figure 10, shows the difference between the alloy systems and heat treatment conditions as well [104]. The PH-FP-steel shows a higher flow stress k_f, which increases at higher strain rate. In comparison 42CrMo4 shows a lower flow stress, due to the annealing treatment, with a further decrease with increasing strain rate. This reduction at higher strains can occur either due to deformation of the flanges of the used Rastegaev specimen or because of softening effects of the material due to increased temperatures at higher strain rates during forming [104–106].

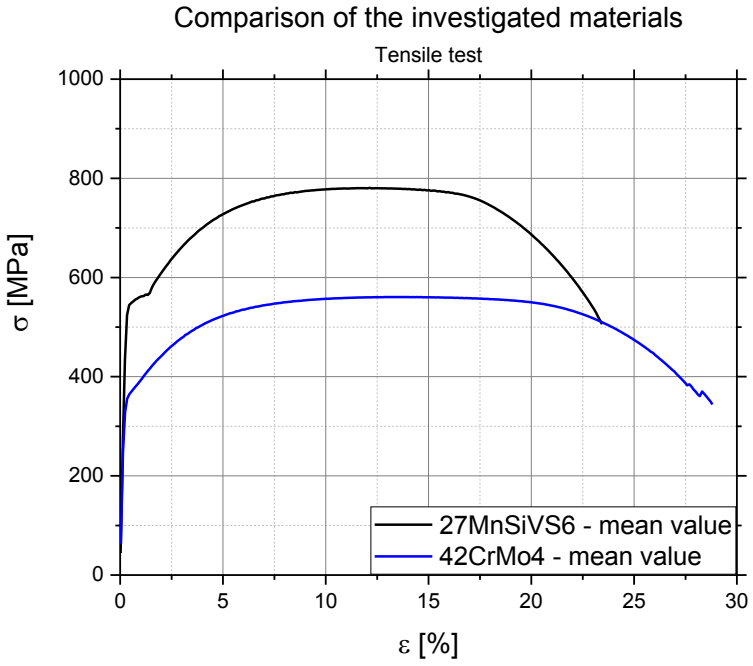

Figure 9: Comparison of the investigated materials – tensile test

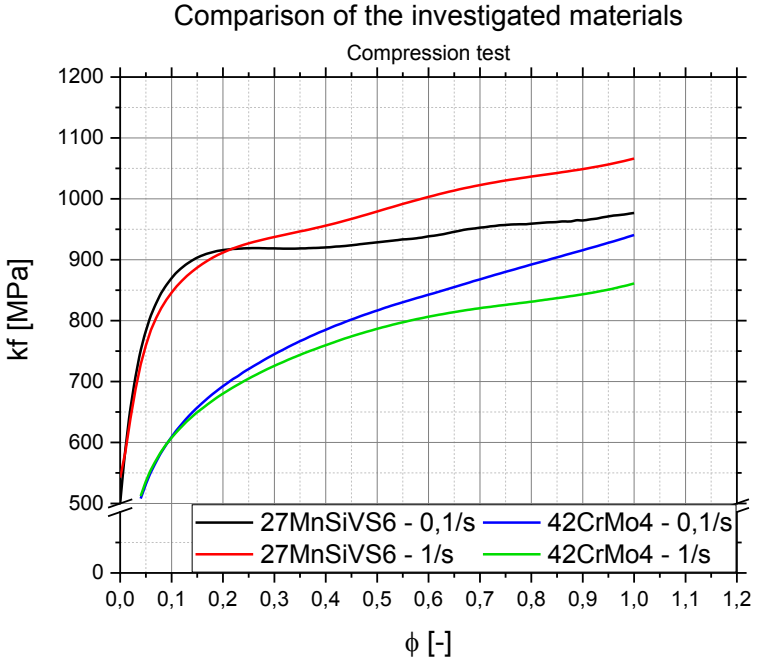

Figure 10: Comparison of the investigated materials – compression tests at strain rates of $\dot{\varphi} = \frac{0,1}{s}$ and $\dot{\varphi} = \frac{1}{s}$

3.2. Microstructural analysis of 27MnSiVS6 in as-rolled condition

Alloyed vanadium (V) leads to the precipitation of vanadium carbo-nitrides during the controlled cooling after the hot rolling of the material. Due to this precipitation, a smaller grain size and a higher strength can be achieved [107]. The ferritic-pearlitic structure of the PH-FP-steel is shown in Figure 11 and Figure 12 in transverse direction and in Figure 13 and Figure 14 in longitudinal direction. The direction of rolling can be clearly seen in the longitudinal sections. The batch of material used in the experiments shows an average grain size (GS) of 5,9 µm with a ferrite-to-pearlite (F/P) ratio of 46 %:52 % (± 5 %). The fine grain structure seen in the micrographs is due to alloying with ~0,12 % V. The microsections used for the measurements were created by grinding and polishing with a 1 µm polishing agent followed by etching with 3 % Nital solution for 10 seconds.

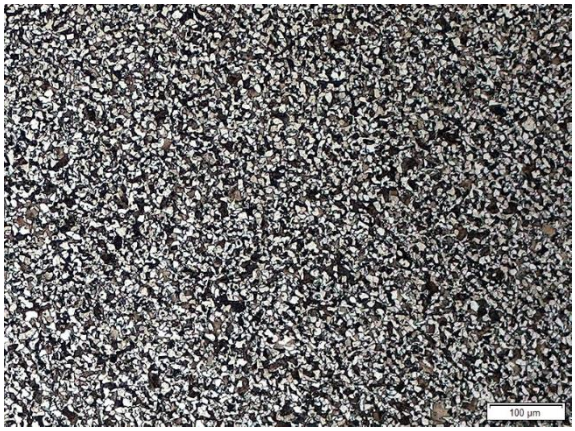

Figure 11: 27MnSiVS6 (as-rolled), transverse section 100x magnification

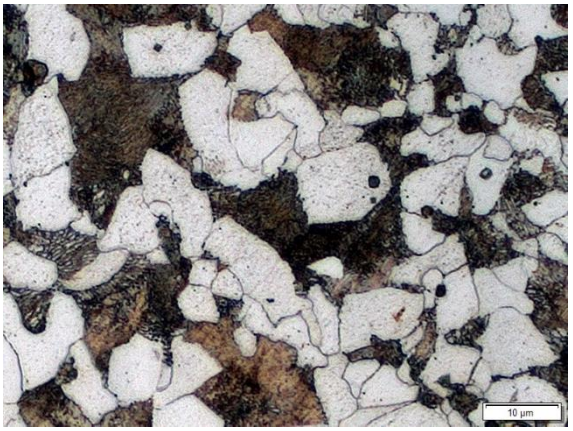

Figure 12: 27MnSiVS6 (as-rolled), transverse section 1000x magnification

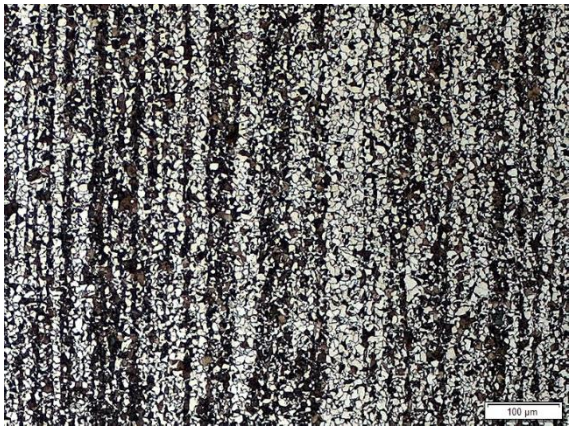

Figure 13: 27MnSiVS6 (as-rolled), longitudinal section 100x magnification

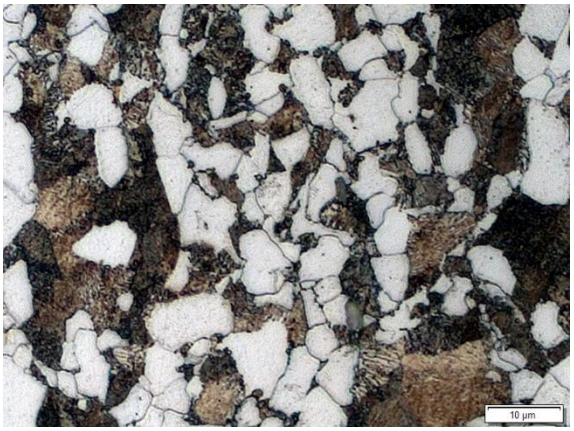

Figure 14: 27MnSiVS6 (as-rolled), transverse section 1000x magnification

Steel cleanness of the material was investigated using the standardized testing method "*K*" of DIN 50 602 and DIN EN 10247 [108]. For this examination, non-metallic inclusions (NMI) are separated into the following groups: (i) oxide inclusions with lamellar shape (OS), (ii) oxide inclusions with globular shape (OG), (iii) dissolved oxide inclusions (OA) and (iv) sulfide inclusions with lamellar shape (SS). From these types of NMI, a factor *K 2* is calculated. The

investigated PH-FP steel shows a high degree of cleanness with a K 2-value of 3,38 with a small amount of OS-type inclusions and sporadic lamellar MnS inclusions in the ferritic-pearlitic steel matrix.

3.3. Microstructural analysis of 42CrMo4 in annealed condition

Due to the (soft-) annealing of the material, the cementite has formed into a globular shape with the grain boundaries still visible on the optical micrographs (Figure 15 – Figure 18). This leads to a higher ductility in combination with a reduced strength of the material which is beneficial for the manufacturing of complex shapes, for example gears or fasteners [109]. The final material strength for applications is adjusted by quenching and tempering after the final forming step [1; 99; 110].

The micrographs taken in transverse direction (Figure 15 and Figure 16) show a ferrite matrix with globular cementite but no preferred orientation of the microstructure. In the longitudinal microsections, on the other hand, banding of the microstructure in the rolling direction is still visible after the soft-annealing process (Figure 17 and Figure 18).

Figure 15: 42CrMo4 (annealed), transverse section 200x magnification

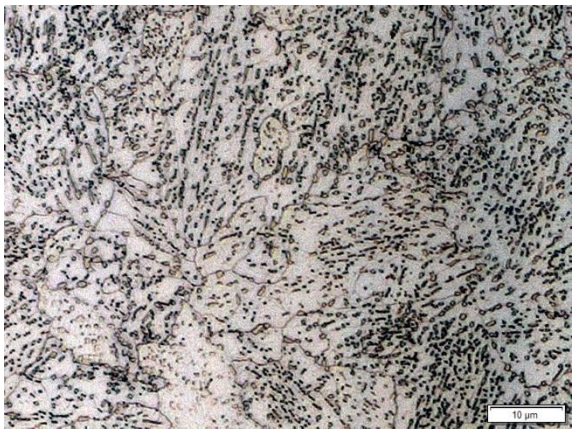

Figure 16: 42CrMo4 (annealed), transverse section 1000x magnification

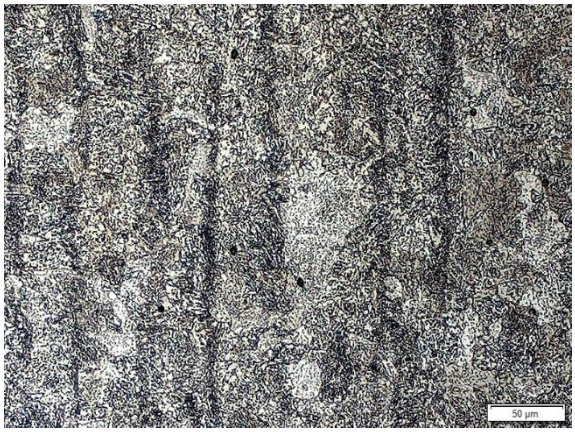

Figure 17: 42CrMo4 (annealed), longitudinal section 200x magnification

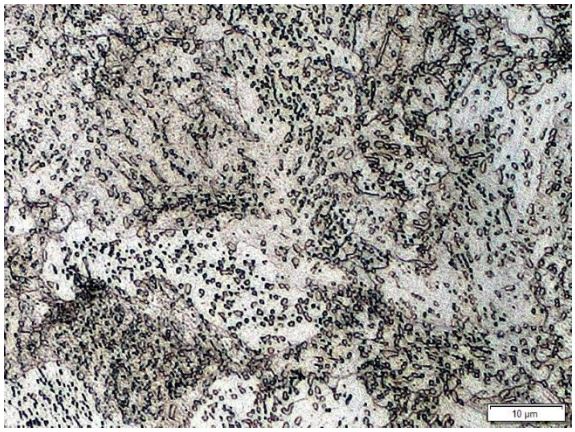

Figure 18: 42CrMo4 (annealed), longitudinal section 1000x magnification

Steel cleanness measurements on the basis of method *K* of standards DIN 50 602 and DIN EN 10247 is not possible for soft-annealed materials, due to the finely dispersed, globular cementite (Fe_3C) in the ferrite matrix. However, based on the micrographs, the investigated steel batch shows a high degree of cleanness with only sporadic NMI visible.

4. Overview over experimental procedures

In this chapter, the experimental procedures used for the investigations are described in detail. The approach for defining the influences on forming behaviour of the materials specified in chapter 3 can be separated into two independent parts. Firstly, the material behaviour is investigated on a microscopic scale, using an in-situ tensile testing method built into a scanning electron microscope (SEM) combined with digital image correlation (DIC). Secondly, an application-oriented testing method simulating the final deformation step during cold heading of screws and fasteners, developed and optimized during this project, is applied to analyse the deformation and damaging behaviour of the materials. In addition to the experimental investigations with the cold heading test (CHT), finite element simulation is used to quantify the formability of the investigated steel grades.

4.1. In-situ tensile testing using a SEM

To investigate the forming behaviour of metals on a microscopic scale, the two selected materials, 27MnSiVS6, as-rolled, and 42CrMo4, annealed, are examined by the means of in-situ tensile testing. Therefore, a 15 kN tensile/compression module (Figure 19) manufactured by Kammrath & Weiss, specifically designed for microscopic tensile testing, is used for the experiments. The samples, in this case flat tensile samples (Figure 20), are manufactured using wire-cut EDM (electrical discharge machining) followed by surface grinding with polishing agents of 1 µm grain size.

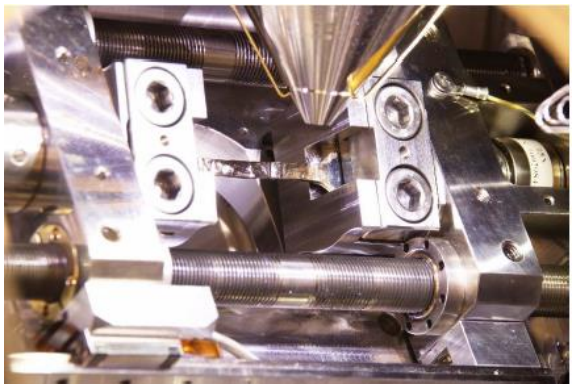

Figure 19: Tensile stage inside SEM

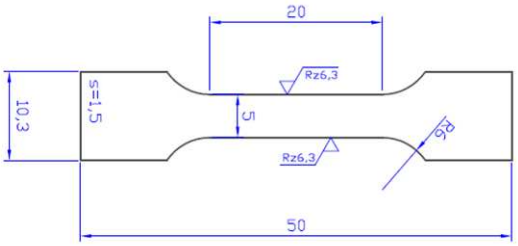

Figure 20: Specimen geometry for in-situ tensile tests

The experiments are conducted using a Zeiss Crossbeam 340 SEM at the Materials Center Leoben (MCL) and consist of two main procedures. Firstly, the digital image correlation (DIC) method used for measuring the strain during deformation are calibrated using methods described in chapter 5.1. Secondly, the tensile tests are performed. Finally, the deformation measured using DIC methods and the globally measured strain are compared. The results of the calibrations as well as the in-situ tensile tests are shown in chapter 5.

4.2. Cold heading test (CHT)

The experimental setup for the cold heading testing (CHT), based on an optimized testing apparatus for radial extrusion presented by Guk, et al in 2017 is shown in Figure 21 [60]. The main goal of the experiments is the application-oriented investigation of the forming and damaging behaviour of materials during cold forming, especially cold heading.

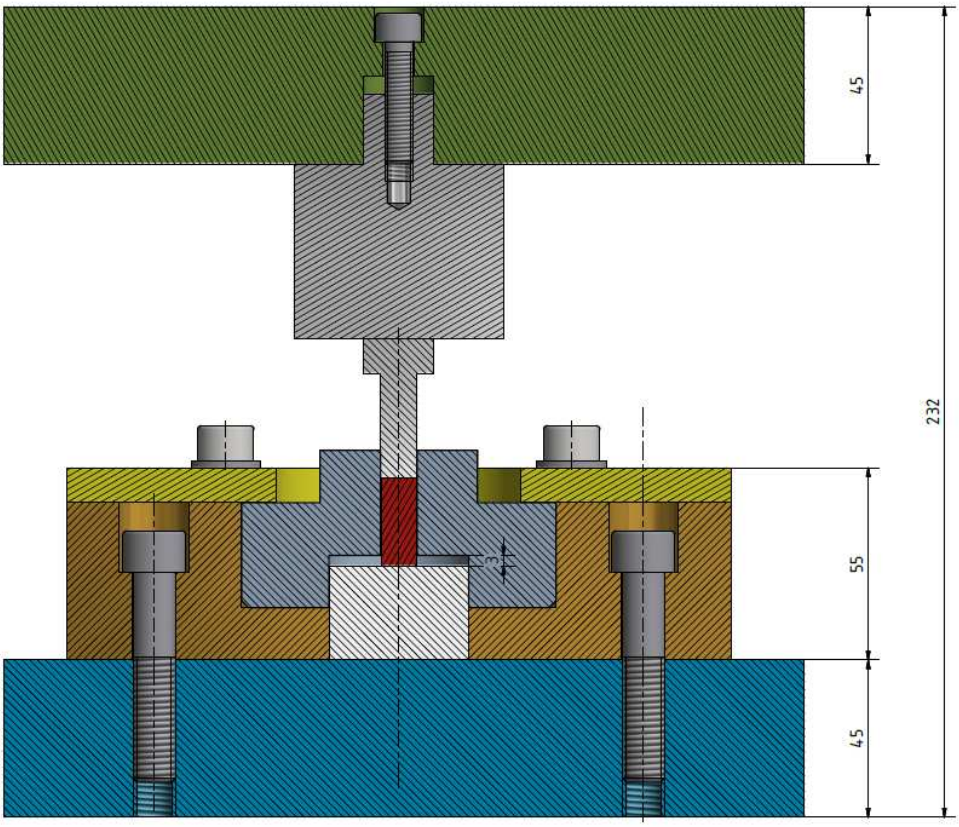

Figure 21: Experimental setup for the cold heading test (CHT)

The experiments are conducted at two different machine types to investigate a range of different strain rates which use the same experimental setup pictured in Figure 21 :

1. A walter+bai LFV-T (w+b LFV-T), a servohydraulic testing system with a maximum compression force of F_{max} = 200 kN and a maximum strain rate of $\dot{\varphi} = \frac{0{,}1}{s}$.
2. A Servotest servohydraulic testing system with a maximum compression force of F_{max} = 330 kN and a maximum strain rate of $\dot{\varphi} = \frac{10}{s}$.

The w+b LFV-T system is used for the optimization of the cold heading test setup as well as the determination and comparison of the deformation behaviour of the investigated materials at lower strain rates. For investigations at higher strain rates and the influence of heat treatment

on the materials, the Servotest system is used. The general setup, as shown in Figure 21, is the same for both testing machines with the general parameters shown in Table 4.

Table 4: Testing parameters for the two experimental setups

Testing system	F_{max} [kN]	s_{max} [mm]	$\dot{\varphi}_{max}$ [1/s]	stop criterion [% F]
w+b LFV-T	200	15	0,1	0,5
Servotest	330	15	10	0,5

To guarantee a high durability of the CHT-setup, tools contacting the specimen during deformation are manufactured using the high speed tool steel S390 hardened to a value of ~65 HRC (the chemical composition is shown in Table 5). For other parts of the system, structural steel is used.

Table 5: Chemical composition of S390 high-speed steel [111]

C [wt.%]	Si [wt.%]	Mn [wt.%]	Cr [wt.%]	Mo [wt.%]	V [wt.%]	W [wt.%]	Co [wt.%]
1,64	0,60	0,30	4,80	2,00	4,80	10,40	8,00

The geometry of the specimen used for cold heading testing is shown in Figure 22. The samples are machined from coiled wire rod, with a bevelled edge at both faces. After machining, the specimens are coated with Zn-phosphate and lubricant to achieve a friction coefficient of μ ~ 0,05 to lower wear and increase tool life [99; 112; 113].

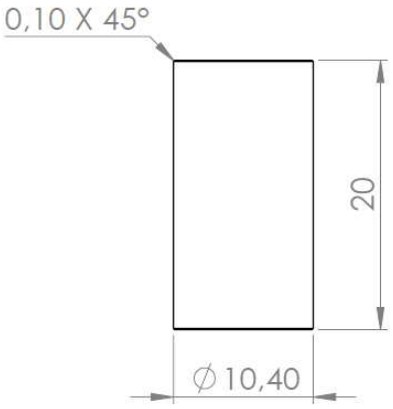

Figure 22: Geometry of specimen used for the cold heading test

4.3. Finite element simulation

To complement the experimental investigations of the cold forming behaviour, the cold heading test (CHT) is modelled using the finite element simulation software simufact.forming™, Version 15. The setup of the simulation is shown in Figure 23, with the numbered parts as follows:

1. Moveable tool
2. Punch, defined as an elastic die (no plastic deformation)
3. Specimen, rectangular mesh with element size (edge length) = 0,15 mm
4. Counterpunch, only elastic deformation possible
5. Die, only elastic deformation possible
6. Base frame combined with counter die, frame rigidity realized with a generic spring setup

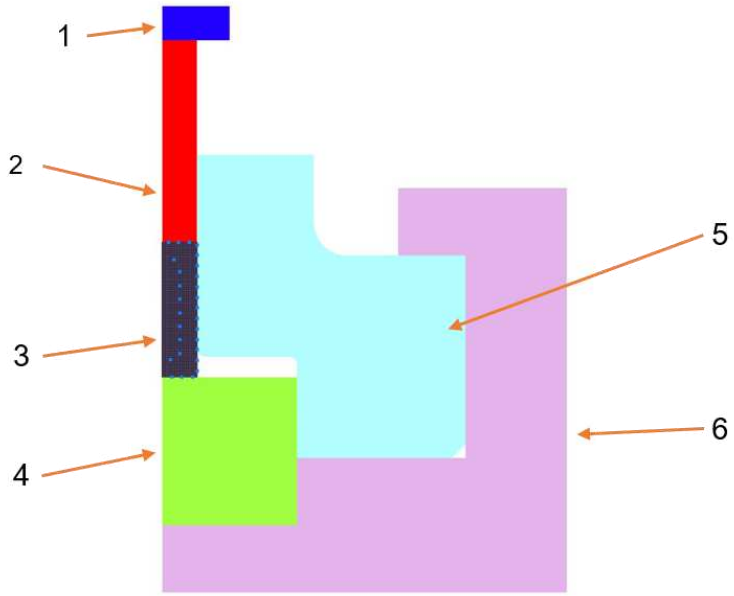

Figure 23: Simulation setup in simufact.forming™ V15

The key characteristics implemented for the investigated materials are taken from compression tests of 27MnSiVS6, as-rolled, and 42CrMo4, annealed, as well as the Dr. Sommer materials database [114]. To simulate the damage behaviour, the ductile damage model of Oyane is implemented, equation (15), because the hydrostatic stress state, tensile and compressive, is taken into account in this model [69; 75].

$$C_{Oyane} = \int \left(A + \frac{\sigma_m}{\sigma_V}\right) d\bar{\varepsilon} = \int \left(A + \frac{\left(\frac{\sigma_1+\sigma_2+\sigma_3}{3}\right)}{\frac{1}{\sqrt{2}}\sqrt{(\sigma_1-\sigma_2)^2+(\sigma_2-\sigma_3)^2+(\sigma_3-\sigma_1)^2}}\right) d\bar{\varepsilon} \qquad (15)$$

The key simulation parameters are as follows:

- Built up as a 2D-simulation
- Punch velocity v_{Punch} = 4 mm/s, this equals a strain rate of $\dot{\varphi} = \frac{0,1}{s}$ in the upper part of the die, not the flange area
- Maximum punch stroke s_{max} = 17 mm
- A combined friction model is used with friction coefficient μ = 0,05 and friction parameter m = 0,1, taken from [99]
- Specimen geometry: h_0 = 20 mm, d_0 = 10,4 mm
- Meshing parameters: Advancing Front Quad Meshing (quadratic elements) with element size (edge length) l_0 = 0,15 mm
- Element amount: 4522 elements
- 1360 calculation steps (one calculation per 0,0125 mm punch stroke)
- The damage parameters for the materials were calculated empirically from compressive experiments using cylindrical specimen
    - $D_{Oyane,27MnSiVS6}$ = 0,0689
    - $D_{Oyane,42CrMo4}$ = 0,13334

4.4. Adjustment of microstructure using heat treatment

To investigate the influence of different microstructures on the forming behaviour, two steel types, 27MnSiVS6 (PH-FP-steel), in as-rolled condition, and 42CrMo4 (Q&T-steel), annealed, are chosen for different heat treatment procedures. The goal for the PH-FP-steel is to produce a ferritic-pearlitic microstructure with variations in pearlite lamellar distance. To achieve this, a isothermal time temperature transformation (TTT)-diagram (Figure 24), which was calculated by JMatPro by Pfleger et al. in a preceding project, is used as a basis for the applied heat treatment processes shown in Figure 25 [115].

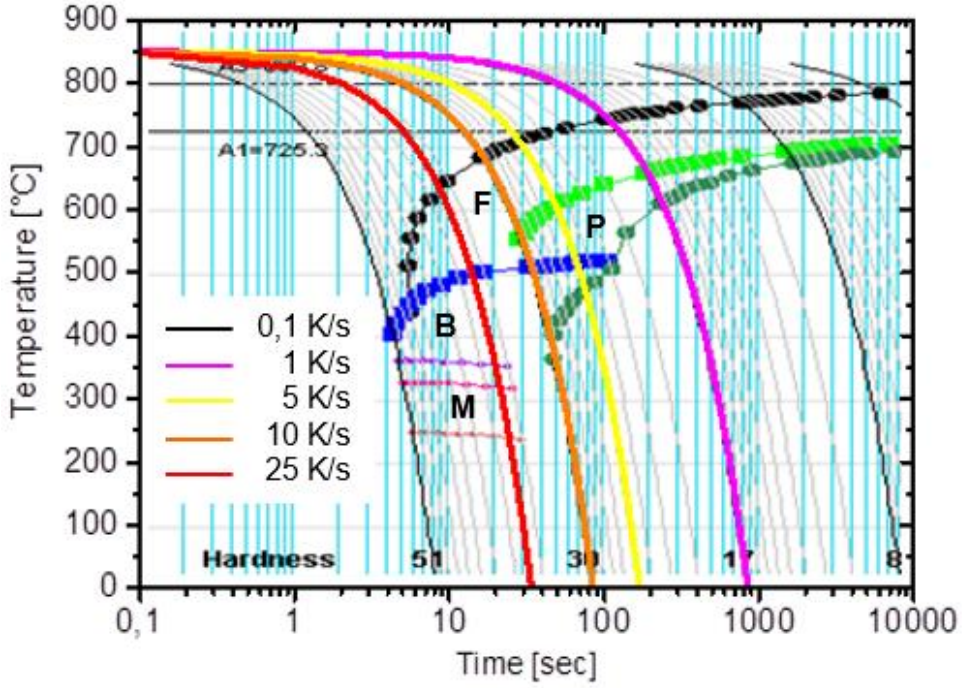

Figure 24: Calculated CTT-diagram of 27MnSiVS6 for an austenitizing temperature of 850 °C [115]

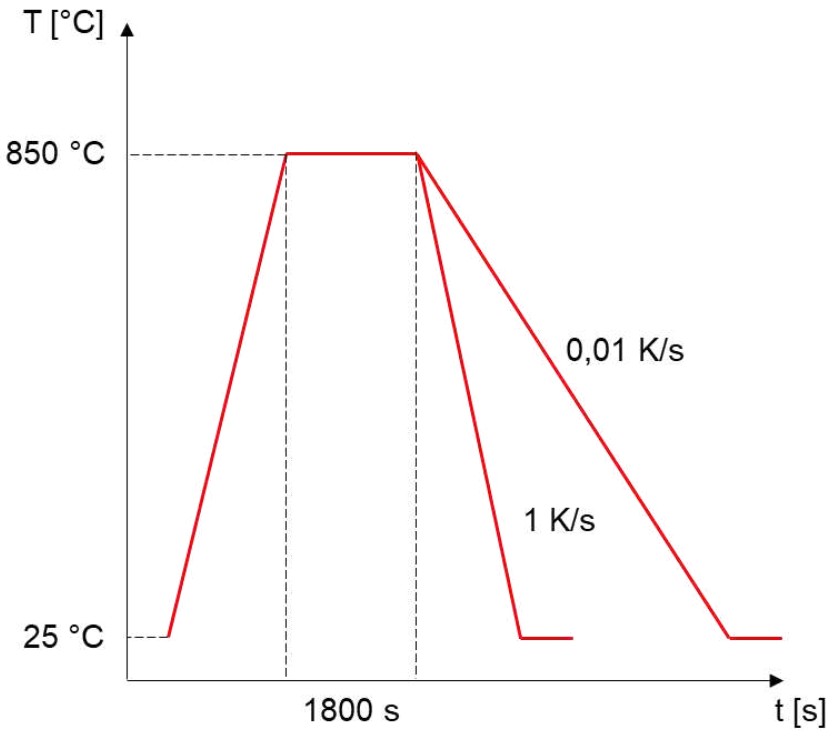

Figure 25: Heat treatment of 27MnSiVS6 to achieve different pearlite lamellar structures; HT 1 – 0,01 K/s, HT 2 – 1 K/s

For the heat treatment of the Q&T-steel, a comparable approach to the PH-FP-steel was taken. The goal was to investigate the influence of different microstructures on the deformation behaviour during cold forming. Therefore, three different heat treatments, in consideration of the TTT-diagram of 42CrMo4 (Figure 26), were conducted. Firstly, to investigate the typical microstructure of the material, a quenching and tempering treatment is executed. Secondly, the material is fully austenitized at 850 °C followed by a slow controlled cooling step to achieve a coarse ferritic-pearlitic (FP) structure. Lastly, in a third heat treatment experiment, a different FP structure was adjusted as suggested by Eggbauer, Lukas et al [116]. The schematic overview over the different heat treatments is shown in Figure 27.

To investigate the forming behaviour of treated materials, tensile testing with round specimen as well as CHT-testing, as shown in chapter 4.2, is conducted. The results of the investigations using the cold heading test (CHT) are shown in chapter 6.

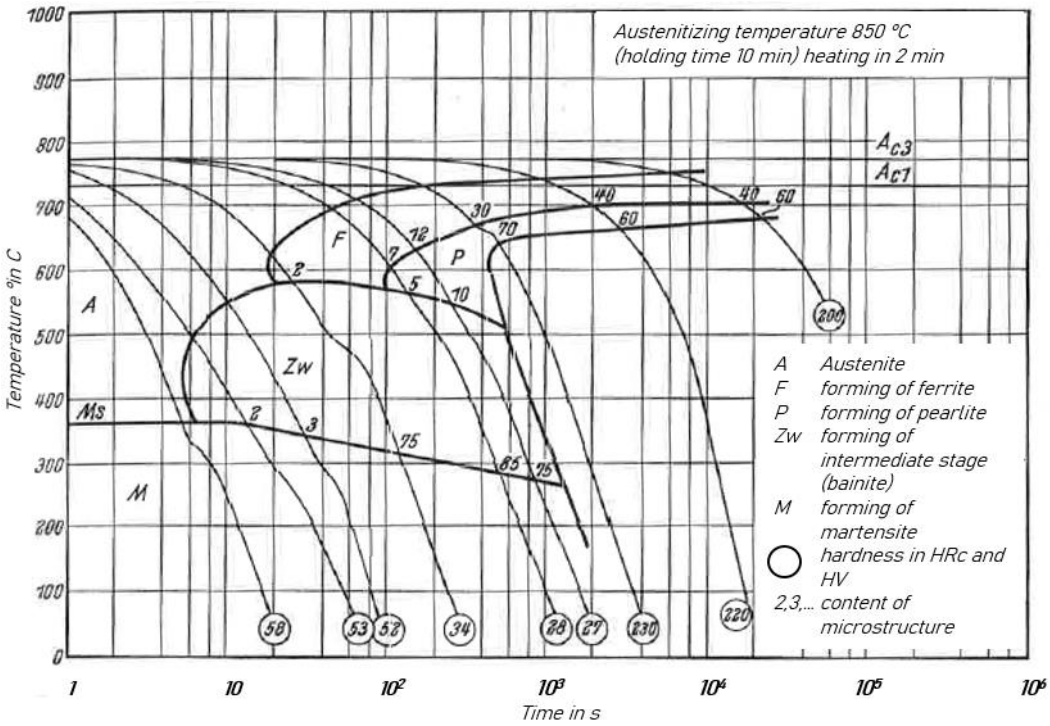

Figure 26: Calculated continuous TTT-diagram (CCT) for 42CrMo4 for an austenitizing temperature of 850 °C [117]

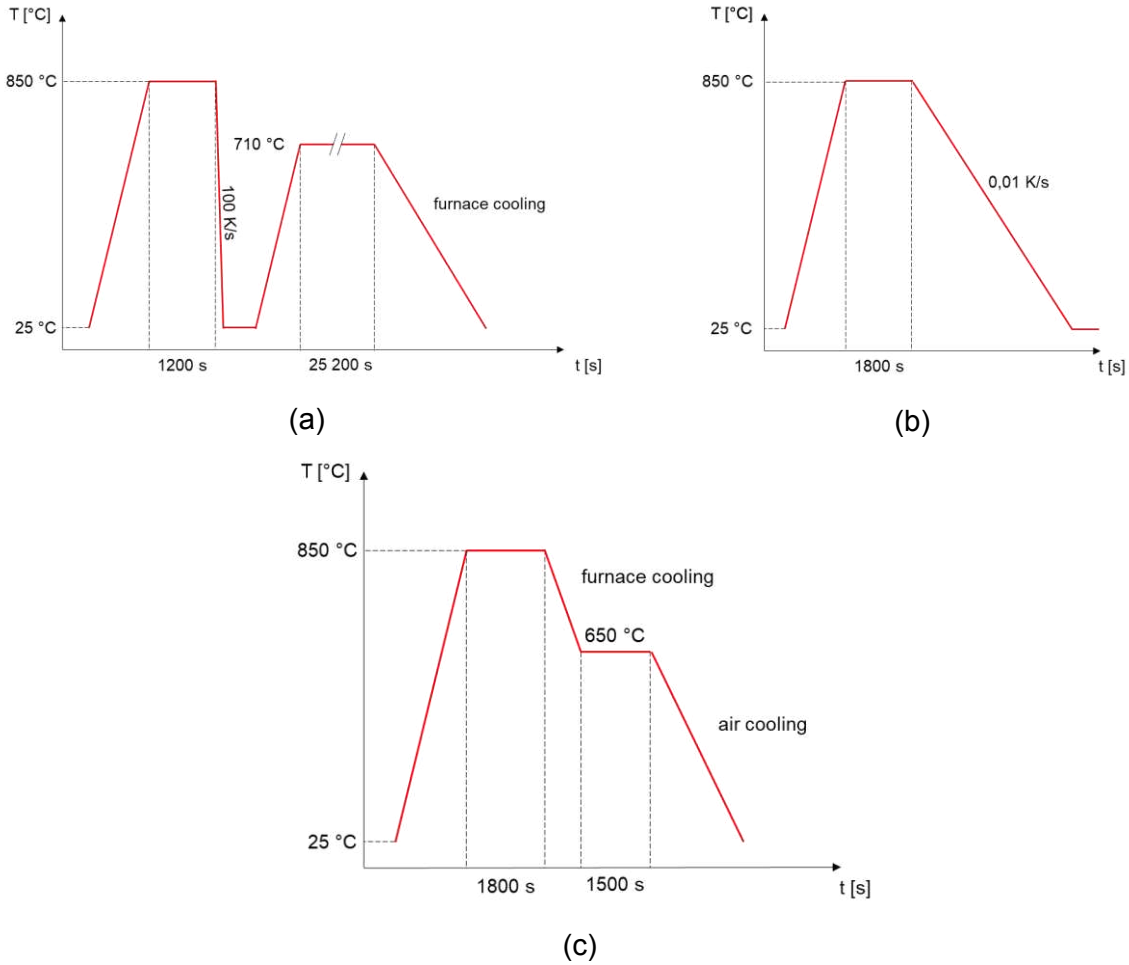

Figure 27: Conducted heat treatments of 42CrMo4 – (a) HT 1-Quenching and Tempering, (b) HT 2-slow cooling for a lamellar ferritic-pearlitic (FP) structure, (c) HT 3-FP structure as proposed by Eggbauer, Lukas et al [116].

5. Microstructural characterization of the material behaviour during deformation

In this section, the results of the investigation of the forming behaviour of materials on a microscopic level is discussed in detail. To characterize the homogeneity of the deformation, in a first step, the digital image correlation (DIC) method has to be calibrated to obtain robust information. After the setup of the measurement methods, tensile tests are conducted and the deformation measured with optical DIC is compared with the global stress-strain measurements. By combining these measurement techniques, the forming behaviour of the investigated materials, 27MnSiVS6, in as-rolled condition, and 42CrMo4, in annealed condition, can be described on a microstructural level.

5.1. Calibration and optimization of DIC measurements

To identify the most reliable conditions for measuring the deformation behaviour of the materials on a microstructural level, the influences on the DIC measurements using a SEM have to be evaluated. These factors can be divided into two groups:

- SEM imaging parameters, the type of signal detection and noise reduction methods, and
- sample surface conditions.

The most common signals used for SEM imaging are secondary electrons (SE) and backscattered electrons (BSE). Concerning DIC, SE images have the advantage of capturing images at high scanning speeds, with acceptable signal to noise ratios, which is known to reduce imaging instabilities. But due to the low energy of secondary electrons (<50 eV), SE imaging is sensitive to contaminations on the surface of the specimen. On the other hand, back scattered electrons have higher energy (>50 eV) and BSE images are less sensitive to surface contaminations but require lower scan speeds which leads to increasing imaging instabilities [90].

5.1.1. Patterning methods for sample surface preparation

As has been discussed in chapter 2.5, the application of digital image correlation (DIC) methods require high-quality surface modifications of the investigated specimen. Typically, a pattern is applied to the surface of a sample by different patterning methods. The most widely used procedures can be divided into the following groups, which will be discussed in further detail:

- Microgrid patterns by photolithography [95]
- Remodelling of thin metallic films [96]

- Nanoparticle deposition techniques [97; 98]

The photolithography methods consist of several cumulative steps to achieve a serviceable pattern. First, a combination of a photoresistant compound and a mask, which contains the desired pattern, are applied to the substrate material and exposed using UV light or the electron beam of a SEM. The photoresist decomposes at the exposed areas before development. The structured surface of the substrate is coated with a gold (Au) film. In a final step, the remaining photoresist is dissolved using chemical treatment. After this procedure, the sample is coated with a fine speckle pattern usable for DIC. The process is shown schematically in Figure 28 [93; 95]. This method produces a pattern of high quality, with a wide range of applicable testing, as typically a gold film is deposited. The downsides of this procedure are the high cost of material, as special exposure units are necessary and the time-consuming nature of the process. Therefore, different approaches to surface patterning have been developed, for example the remodelling of thin metal films or the disposition of nanoparticles.

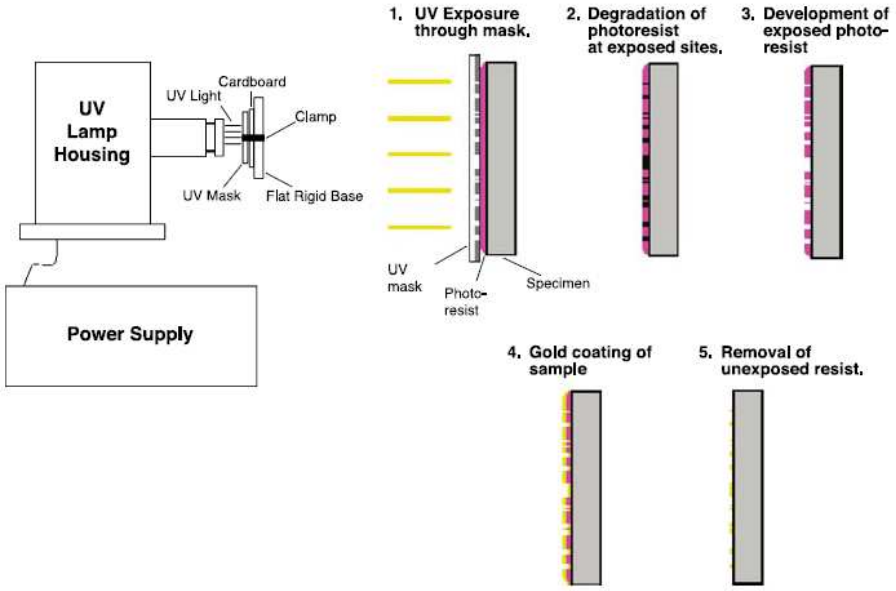

Figure 28: Schematic presentation of the photolithographic patterning method using UV-light [95]

Another widely used procedure, the remodelling of thin films is normally a two-step process. At first, a thin film of Au, Pt, Ag or Pb with thickness > 10 nm is deposited on the surface of the specimen [118]. A metal with high density is used to achieve a high contrast between the substrate material of the sample and the pattern. The coated specimen is placed in a vapour chamber and heated up to a maximum temperature of 300 °C [119]. Under the constant flow of vapour, H_2O if the substrate material is corrosion resistant, otherwise N_2 in combination with other solutions, e.g. iodobenzene, the deposited thin metal film forms metal islands [118]. The size of the speckles depends on the dwelling time in the vapour, as the islands start to consolidate and grow. Exposure times reported in literature range from one to five hours [119].

A schematic representation of a vapour chamber used for the remodelling of thin films is shown in Figure 29.

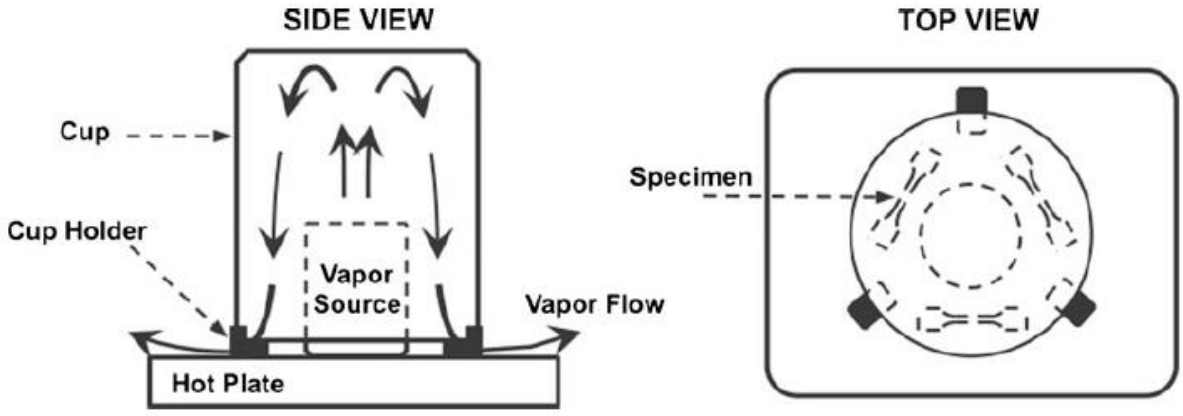

Figure 29: Schematic representation of a vapour chamber used for remodelling of thin films [119]

With the procedures of photolithography and remodelling of thin films it is possible to create a finely dispersed, high contrast pattern for the application of digital image correlation in a SEM. The downside of these methods is the high expenditure of time to create the desired surface pattern as well as the high temperatures used for patterning. To decrease preparation time of samples investigations concerning nanoparticle deposition techniques have been conducted. One approach uses the deposition of Pt or yttria stabilised zirconium (YSZ) with different methodologies for the creation of the pattern [120]. In a first investigation, the YSZ particles are dissolved in an ethanol suspension, dropped on the sample surface, dried and sputter coated with carbon. This process gives high DIC precision, but the spatial distribution of particles is difficult to control. Therefore, the deposition of Pt dots using FIB and FEB imaging and patterning, normally used as a protection layer for TEM sample preparation, is examined. These methods provide a controlled spatial density of the surface pattern well suited for the use in DIC. However, the influence of FIB and FEB, e.g. heat generation at the surface or damaging effects, need to be taken into account [120; 121]. Another method investigated concerning the deposition of nanoparticles is the physical vapour disposition (PVD) of metals [122]. Normally, the sample has to be heated during the coating procedure. This would influence the deformation behaviour of the examined material. However, in this investigation an indium-tin (InSn) soldering alloy with a low melting point is used as the sputtering agent. With this setup, it is possible to create a dense, high-quality DIC pattern which enables the examination of material behaviour on a sub-micron level [122].

With the realisation of fine patterning of a sample surface, the field of application for digital image correlation (DIC) can be expanded to the investigation of material behaviour on a sub-grain level. With the use of in-situ tensile setups, which can be examined using a SEM, the development of local strains during deformation can be investigated. Early investigations show

that in-situ SEM measurements are a tool which enables the local mechanical strain analysis in combination with macroscopic strain [123]. Different types of materials, for example Ti-alloys or DP-steels, can be investigated with the help of in-situ testing and DIC. The strain measurements provide a depiction of the localisation of the deformation at a sub-grain scale, concerning shear bands and strain inhomogeneity [124–126]. The combination of the results of DIC with EBSD (electron back scattered diffraction) measurements provides further insight into the influence of grain structure on the forming behaviour of materials [127–129].

5.1.2. Adjustment of the sample surface of cold heading steels

Considering the patterning methods presented in chapter 5.1.1., a refined and easy-to use surface coating process for digital image correlation (DIC) applications has been developed in collaboration with the Materials Center Leoben (MCL) especially with Dr. Walter Costin. The process, as well as an evaluation of the quality of the pattern concerning (i) signal detection effects, (ii) noise reduction effects and (iii) surface condition effects is presented.

To evaluate the quality of SEM imaging as well as the surface condition, two types of specimen are used. For investigation of the image instability, gold-coated carbon samples (Au on C) are selected. For evaluation the influence of the surface condition, two types of AFP-steel samples are used. One specimen is polished with colloidal silica (OP-U) as the final preparation step (Figure 30) and the other is prepared using OP-U polishing followed by a gold (Au) sputter coating (Figure 31). The sputtering time is chosen as 10 s with a following thermal treatment at a constant temperature of 100 °C for 3 h. This leads to a random distribution of fine Au particles which can be recognized and processed by the DIC software.

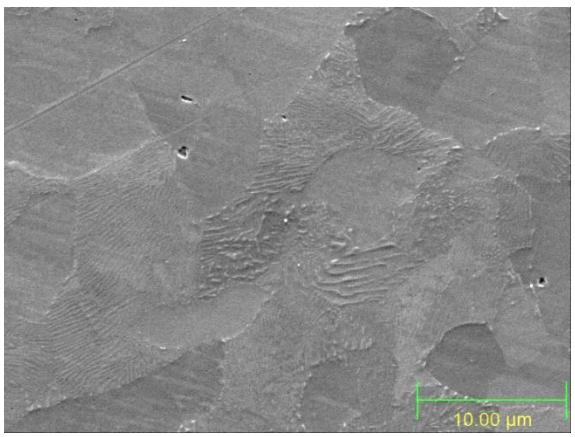

Figure 30: AFP-steel, OP-U polishing
3000x magnification

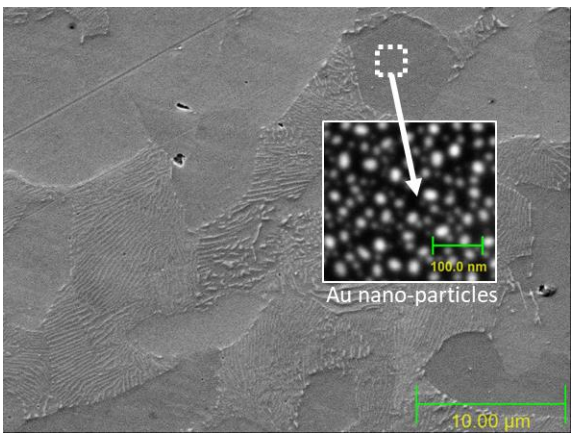

Figure 31: AFP-steel, OP-U polishing + Au sputtering
3000x magnification

To assess the quality of SEM imaging instabilities the displacements between subsequently taken images of the same region without external load and under the same surface conditions is measured. In an ideal case, no displacements should occur between these images. In reality,

however, SEM imaging always involves instabilities due to the type of image generation (rastering) [90]. To evaluate these errors, two criteria have been chosen [130]:

- the standard deviation of displacements (SD^{DIC}) and
- the ratio *R* between the average of the standard deviation ($\overline{SD}$) of the displacements in an image in columns and rows

The first criterion, the standard deviation of displacements for all facets between the taken images, is calculated for both x (horizontal, equation 16) and y (vertical, equation 17) directions and can be used as an indicator for the measurement accuracy. It also shows the imaging instability of the SEM images, with low values of SD^{DIC} meaning a high accuracy of measurements, but no information of displacement distribution can be obtained [130]. The standard deviation is calculated with the following equations:

$$SD_x^{DIC} = \sqrt{\frac{1}{N}\sum_i \left(\Delta_x^i\right)^2} \tag{16}$$

$$SD_y^{DIC} = \sqrt{\frac{1}{N}\sum_i \left(\Delta_y^i\right)^2} \tag{17}$$

with N as the number of all facets analysed by DIC.

To identify the presence of order in the displacements, the ratio *R* can be used to find patterns in rows and columns, as is expected by the way a SEM image is created [130]. It consists of the ratio between the average of the standard deviation ($\overline{SD}$) of the displacements in an image in columns ($\overline{SD}^{cols}$) and rows ($\overline{SD}^{rows}$) and is calculated for both the x and y directions [130]:

$$\overline{SD}^{cols} = \frac{1}{m}\sum_{j=1}^{m} SD_j = \frac{1}{m}\sum_{j=1}^{m}\sqrt{\frac{1}{n}\sum_{i=1}^{n}\left(\Delta_i(j) - \overline{\Delta_i(j)}\right)^2} \tag{18}$$

$$\overline{SD}^{rows} = \frac{1}{n}\sum_{i=1}^{n} SD_i = \frac{1}{n}\sum_{i=1}^{n}\sqrt{\frac{1}{m}\sum_{j=1}^{m}\left(\Delta_i(j) - \overline{\Delta_i(j)}\right)^2} \tag{19}$$

with *n* and *m* being the number of columns and rows. Following from equations 18 and 19, the ratio *R* can be calculated as follows (equation 20):

$$Ratio\ (R) = \frac{\overline{SD}^{cols}}{\overline{SD}^{rows}} \tag{20}$$

R can be interpreted in the following way [130]:

- If $R < 1$, a higher correlation in columns than in rows exists.
- If $R > 1$, a smaller correlation in columns than in rows exists.

If R ~ 1, no evidence for a specific order of displacements can be found.

5.1.3. Investigation of signal detection effects

To determine the influence of the type of signal detection, secondary electrons (SE) or backscattered electrons (BSE), a carbon specimen sputtered with gold (Au on C) is measured under constant and force-free conditions using the DIC software VEDDAC (Version 6.4.0.3). The results for the measurements using SE detection are shown in Figure 32 and Figure 33, those for BSE detection are shown in Figure 34 and Figure 35.

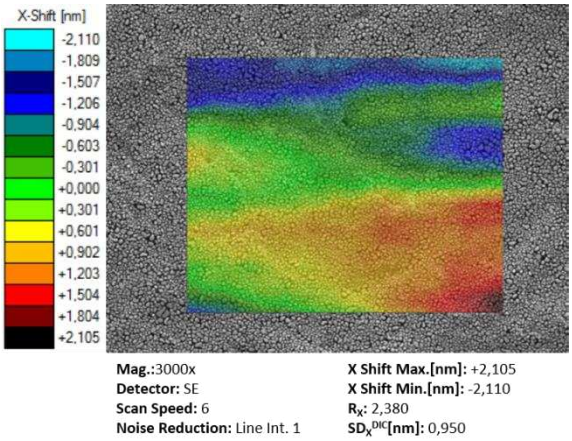

Figure 32: SEM image of Au on C specimen
SE – detector, horizontal direction
3000x magnification

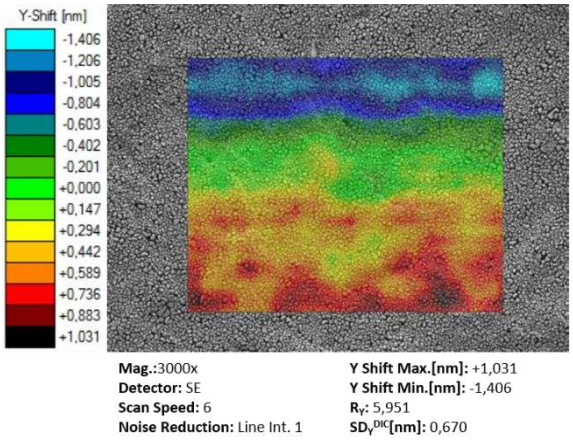

Figure 33: SEM image of Au on C specimen
SE – detector, vertical direction
3000x magnification

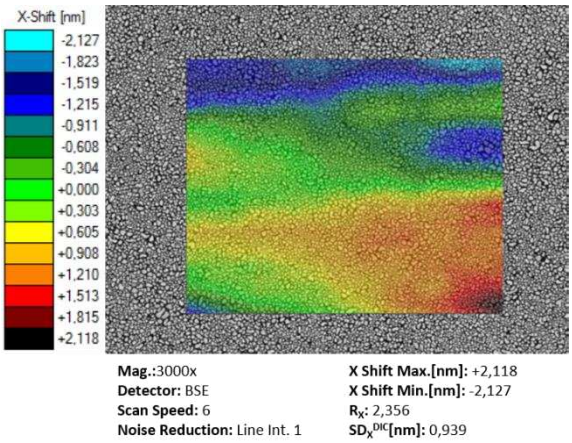

Figure 34: SEM image of Au on C specimen
BSE – detector, horizontal direction

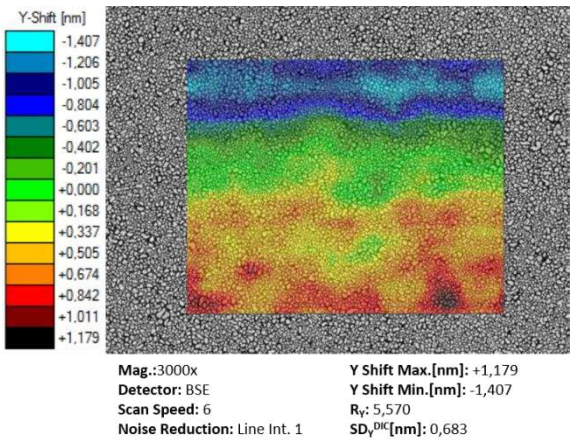

Figure 35: SEM image of Au on C specimen
BSE – detector, vertical direction

The results indicate a minor impact of the chosen detection signal on the quality of the DIC measurement. However, the calculated ratios R show a high correlation of displacements in rows, particularly in vertical (y) direction, which can also be seen by the formation of bands in the DIC images. This banding and other imaging artefacts are often associated with slow scan speeds, which can reduce the noise during imaging but have a high probability of small scanning distortions between subsequently captured images [90; 130]. These will lead to misleading strain data when the images are processed. Therefore, SE signal detection is

chosen for the next steps of the calibration as this method has the advantage of a higher scanning speed.

5.1.4. Investigation of noise reduction effects

The procedure to evaluate the effectiveness of the noise reduction method for DIC measurements is as follows. Two noise reduction methods are tested on two subsequent SE images at a magnification of 3000x:

- A slow scan speed (value 6) is combined with a line interpolation method for a single frame per image (Line Int. 1) (Figure 36 and Figure 37)
- Secondly, a high scanning speed (value 1) is used in combination with a frame interpolation combining 10 frames per image (Frame Int. 10) (Figure 38 and Figure 39)

For these chosen parameters the SD^{DIC} value and the ratio *R* are calculated and compared. The aim is to reach a low standard deviation and a ratio of *R*~1. The results of the line interpolation method are shown in Figure 36 and Figure 37, those for frame interpolation in Figure 38 and Figure 39.

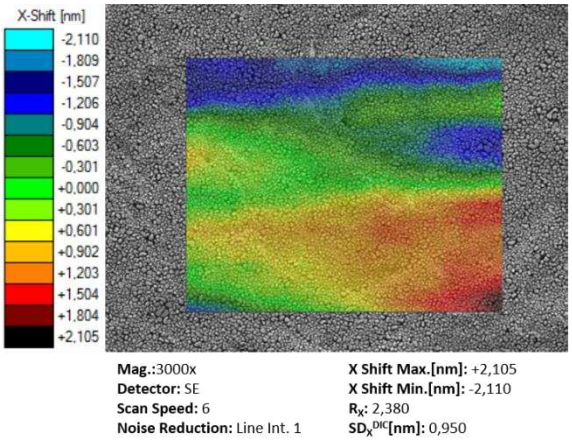

Figure 36: SEM image of Au on C specimen, horizontal direction

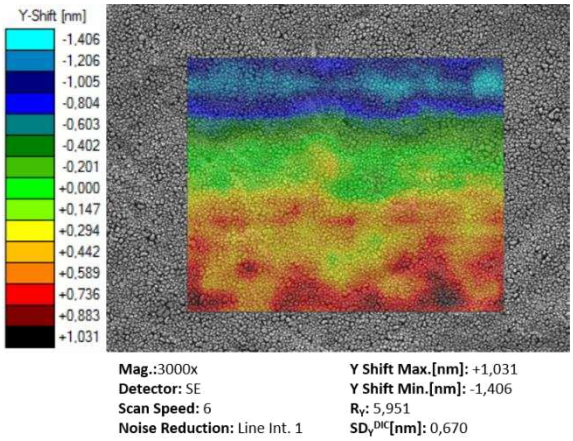

Figure 37: SEM image of Au on C specimen, vertical direction

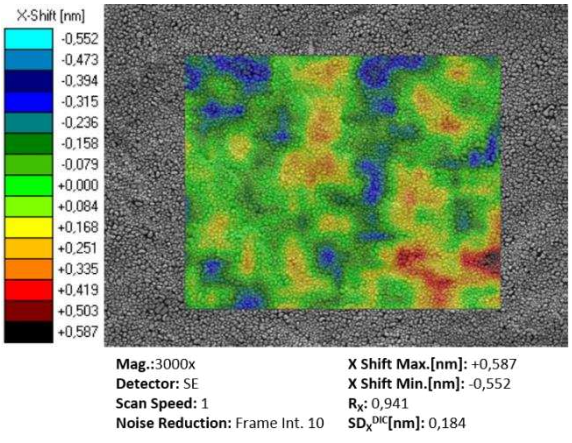

Figure 38: SEM image of Au on C specimen, horizontal direction

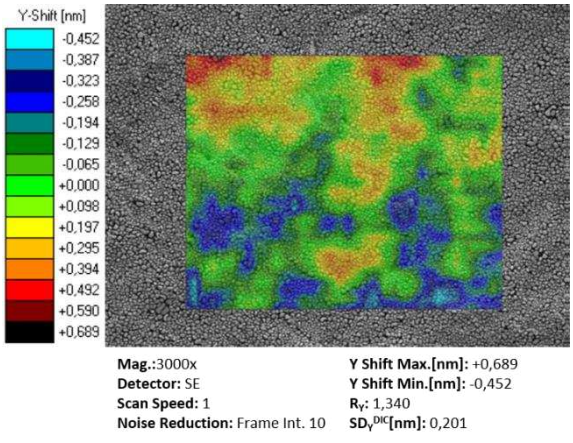

Figure 39: SEM image of Au on C specimen, vertical direction

The images taken for the line interpolation method at slow scanning speeds clearly show an order of displacements in the form of banding as well as a ratio of $R >> 1$ (Figure 36 and Figure 37). This can lead to errors in the strain measurement using DIC due to distortions during the image recording. In contrast, the results of the frame interpolation (Frame Int. 10) show a more random displacement pattern with lower SD^{DIC} values as well as R ratios close to 1. This indicates a higher imaging accuracy and shows that there is no preferred direction of measured strains. Concluding from this results, a frame interpolation method combined with a high scanning speed is used for the following investigations as these parameters show the most promising approach for DIC measurements.

5.1.5. Investigation of sample surface conditions

In the first calibration steps, a carbon sample sputter coated with gold (Au on C specimen) was used for the investigations of the influences of signal detection and noise reduction methods on the quality of DIC measurements. After optimization of the imaging procedures of the SEM, the surface condition of the specimen is evaluated. In literature, many methods for preparation of the sample surface were tested, for example speckle patterns, FIB patterning or template patterning [94; 122; 118; 131].

For this investigation, the polished PH-FP-steel sample is sputter coated with Au for 10 seconds followed by a heat treatment at 100 °C for 3 h. This leads to the formation of randomly distributed Au-islands on the surface. To compare the effect of this patterning method, the prepared sample is compared with a specimen polished with colloidal silica (OP-U). For the investigation, two SEM images are taken at 3000x magnification under stress-free conditions. The DIC measurements with the calculated values of SD^{DIC} and R are shown in Figure 40 and Figure 41 for the polished surface and in Figure 42 and Figure 43 for the patterned surface.

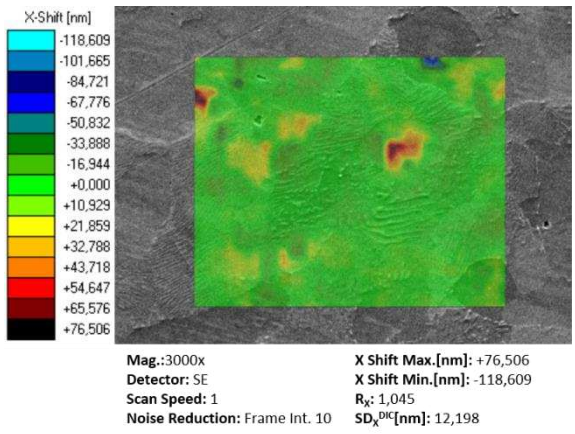

Figure 40: SEM image of PH-FP-steel, final polishing with OP-U horizontal direction

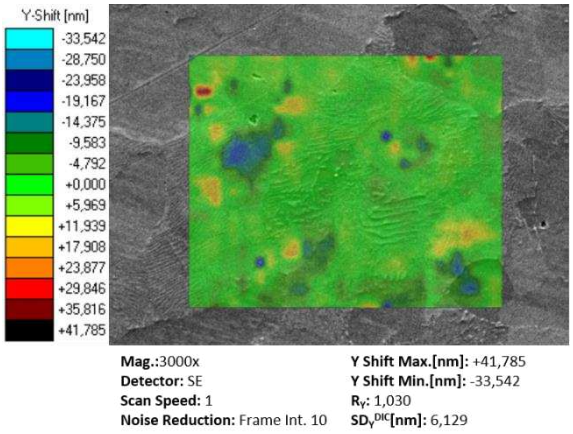

Figure 41: SEM image of PH-FP-steel, final polishing with OP-U vertical direction

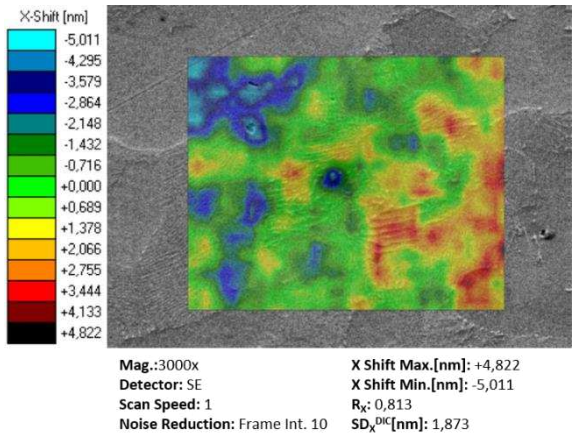

Figure 42: SEM image of PH-FP-steel, final polishing with OP-U + Au – sputtering horizontal direction

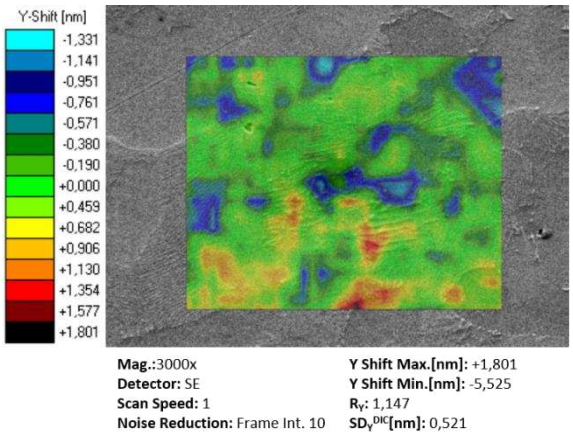

Figure 43: SEM image of PH-FP-steel, final polishing with OP-U + Au – sputtering vertical direction

In both cases the displacement maps of the DIC measurement show relatively random patterns with ratios *R* close to 1 for both surface conditions. However, the sputtering with Au leads to a significant decrease of the standard deviation values, indicating an improvement of the imaging conditions. The accuracy of the measurement also increases significantly for the sputtered sample. Therefore, the optimized parameters for the in-situ measurements are chosen as follows:

- SE signal detection
- High scanning speed
- Frame interpolation method with (>10 frames per image)
- Sample surface polished with OP-U and sputtered with Au for 10 s followed by a thermal treatment at 100 °C for 3 h

These parameters minimize the influences of the imaging method as well as the sample surface on the strain measurement using DIC and enable a comparison between the strain measured at a microscopic level and the global stress-strain curve.

5.2. In-situ tensile testing

The in-situ tensile test is conducted on a Kammrath & Weiß 15 kN tensile/compression module (Figure 19) built into a Zeiss CrossBeam 340 SEM calibrated with the optimized parameters determined in the previous chapter. The specimen is prepared following the specifications established in the calibration experiments, polishing with OP-U followed by sputtering with Au and thermal treatment to form randomly distributed Au islands. The specimen geometry is shown in Figure 20 in chapter 4.1. The software used for the DIC measurement is VEDDAC in the upgraded version 7, which uses optimized sub-pixel algorithms compared to version 6.4.0.3. The exact parameters for imaging as well as the DIC software are shown in the following Table 6.

Table 6: Imaging and software parameters – in-situ tensile testing

Imaging parameters	**Software parameters**
• Acceleration voltage (EHT): 10 kV • Aperture: 60 µm • Working distance (WD): 15 mm • Detector: secondary electrons (SE) • Scan speed: 1 (238 µs per line) • Noise reduction: frame interpolation (25 frames per image) • 6 images taken per measurement • Magnification: 1000x • Resolution: 2048 x 1536 • Pixel size: 55,82 nm = 0,05582 µm	• Software version: VEDDAC v7 • Measurement field size: 300 x 300 pixel • Reference field size: 100 x 100 pixel • Number of measuring points: 34 x 24 • Spacing of measuring points: 50 pixel • Correlation algorithm: full correlation • Subpixel algorithm: parabolic

The tensile tests have been conducted with $v = 5*10^{-6}$ m/s (5 µm/s), the maximum speed of the tensile module to replicate a tensile test according to standard DIN 50125 (ISO 6892-1) as close as possible [103]. The sample is tested to a maximum engineering strain of 10 % with images for DIC measurement taken every $\Delta\varepsilon = 2$ %. The maximum strain of $\varepsilon_{max} = 10$ % is selected as only a uniaxial stress state is investigated to be able to focus on the deformation of the grains without vertical movement of the observed sample area due to necking of the specimen. To enable the imaging process and avoid errors in the strain measurement due to creep and motor vibrations, the specimen is unloaded before the images are recorded. Therefore, holding points with a load of $\sigma = 0$ MPa are visible in the curve progression of the stress-strain curve shown in Figure 44.

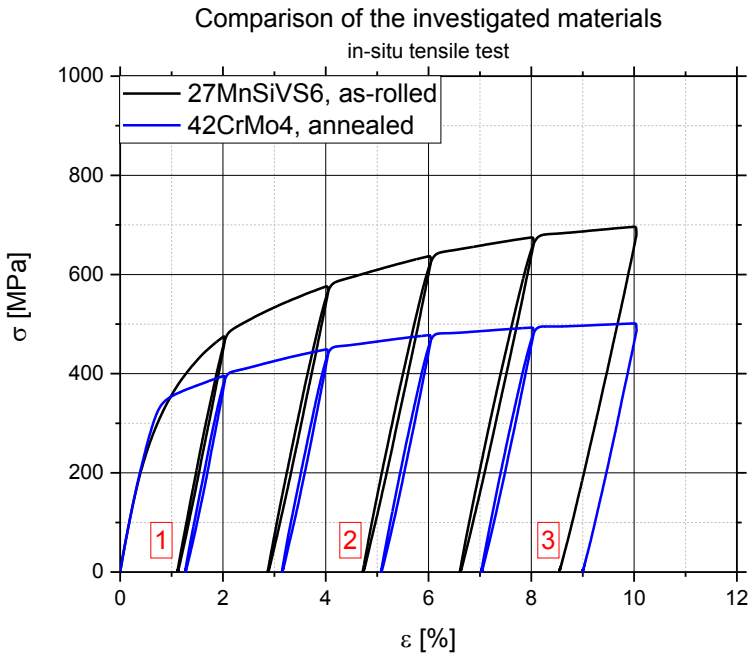

Figure 44: Comparison of the investigated materials – in-situ tensile testing

The DIC measurement is taken at three holding points during the in-situ tensile test, at $\varepsilon_1 = 2$ %, $\varepsilon_2 = 6$ % and $\varepsilon_3 = 10$ %. Due to the elastic contraction of the specimen after unloading, the true elongation is lowered by $\Delta\varepsilon \sim 1{,}0\text{-}1{,}7$ % at the point of investigation and is shown clearly in the measurement data in Table 7 and Table 8. At the holding points the forming behaviour of the two investigated materials, 27MnSiVS6, as-rolled, and 42CrMo4, annealed, on a microstructural level can be evaluated.

In Figure 45, the deformation of the ferritic-pearlitic structure of the PH-FP-steel is shown in SEM images. The ferrite grains can be distinguished from pearlite by the darker shading and the difference in surface contours. During forming, the topography of the surface changes, due to slip at grain boundaries in perpendicular direction to the measured sample area. This is evident at the image taken at $\varepsilon = 10$ % strain. Most of the deformation of the sample occurs by rotation and stretching of ferrite grains while the pearlite mostly retains its shape during the tensile test. But it is difficult to clearly depict the areas where the plastic deformation takes place. To this end, DIC measurement of the specimen is conducted. The square shaped area in the middle of the image results from electron beam induced contamination during imaging, but does not influence the quality of the DIC, as seen in Figure 46.

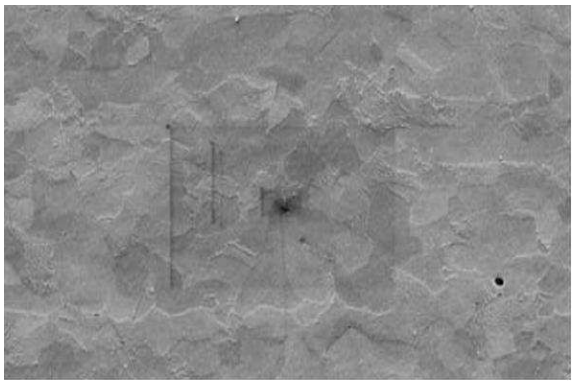

Measurement step 1 – 2 % strain
27MnSiVS6, as-rolled

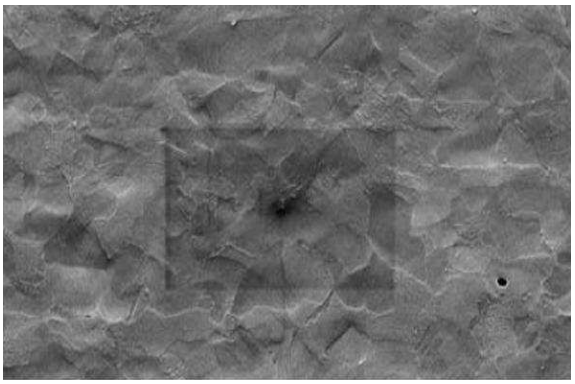

Measurement step 2 – 6 % strain
27MnSiVS6, as-rolled

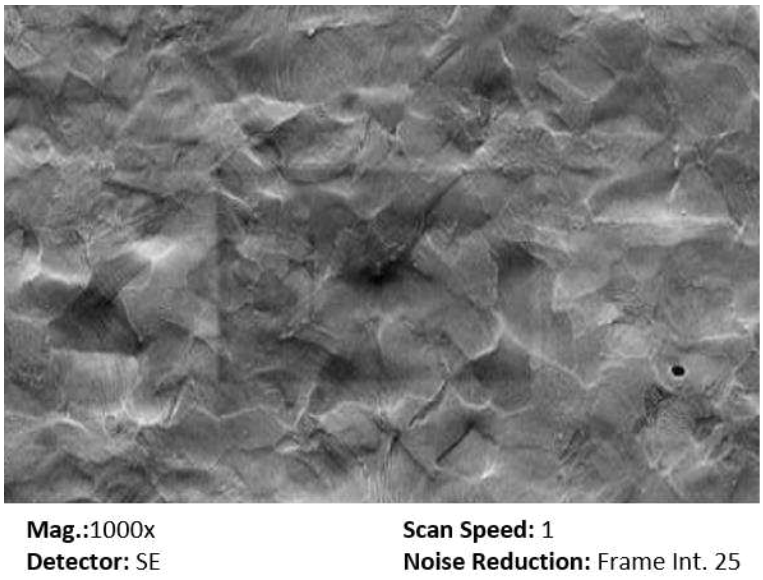

Measurement step 3 – 10 % strain
27MnSiVS6, as-rolled

Figure 45: SEM measurements of in-situ tensile tests – 27MnSiVS6, as-rolled (PH-FP-steel)

The DIC measurement of the sample surface (Figure 46) shows a pronounced localisation of the deformation of the ferritic-pearlitic structure. With increasing strain, the irregular shape of measured deformations increases, with the areas of high strain showing an alignment with the ferritic grains. The high strength pearlitic grains display a many times lower displacement during forming as can be seen in the blue areas in the DIC images. It can be concluded that the PH-FP-steel shows a strong localisation of the deformation, mainly in ferritic areas. This observation is supported when the local and maximum strains, measured by DIC, are compared with the global strains measured at the tensile stage. The measurement values are shown in Table 7.

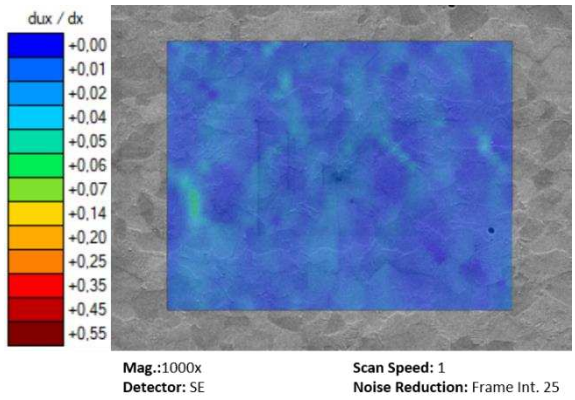

Measurement step 1 – 2 % strain

27MnSiVS6, as-rolled

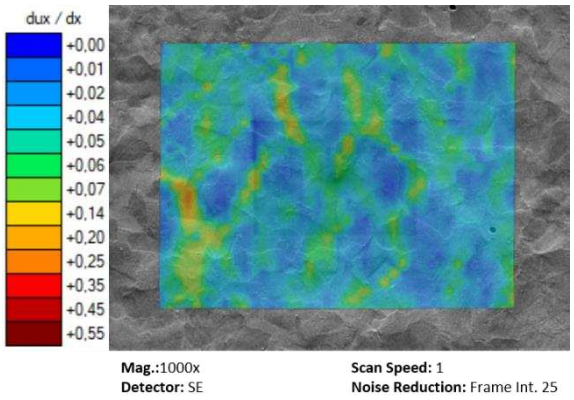

Measurement step 2 – 6 % strain

27MnSiVS6, as-rolled

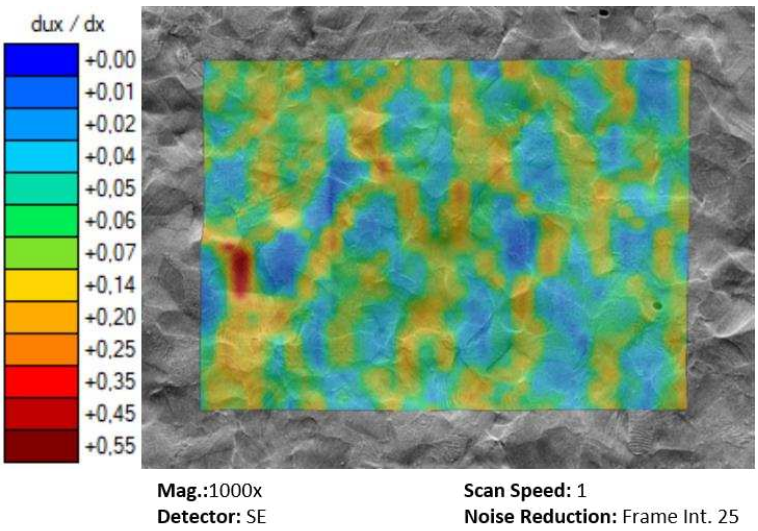

Measurement step 3 – 10 % strain

27MnSiVS6, as-rolled

Figure 46: In-situ DIC measurement of 27MnSiVS6, as-rolled (PH-FP-steel)

Table 7: Comparison of global and local strains – 27MnSiVS6, as-rolled

Measurement step	**Elongation [µm]**	**ε_{global} [%]**	**$\varepsilon_{local,\ average}$ [%]**	**$\varepsilon_{local,\ max}$ [%]**
1	225	1,13	0,94	5,51
2	947	4,73	3,8	23,6
3	1709	8,54	6,96	50,48

The global strain (ε_{global}), measured at the tensile stage, and the average local strain ($\varepsilon_{local,\ average}$), measured by DIC methods, show a decent alignment during the experiment, with the local maximum strain ($\varepsilon_{local,\ max}$) being 5-7 times higher than the average (Figure 47). This can be explained through the localisation of the deformation in the ferrite grains (yellow and red areas), as seen in the DIC measurements in Figure 46. From these results it can be

concluded that the DIC method provides detailed data concerning the localized microstructural behaviour of materials during deformation.

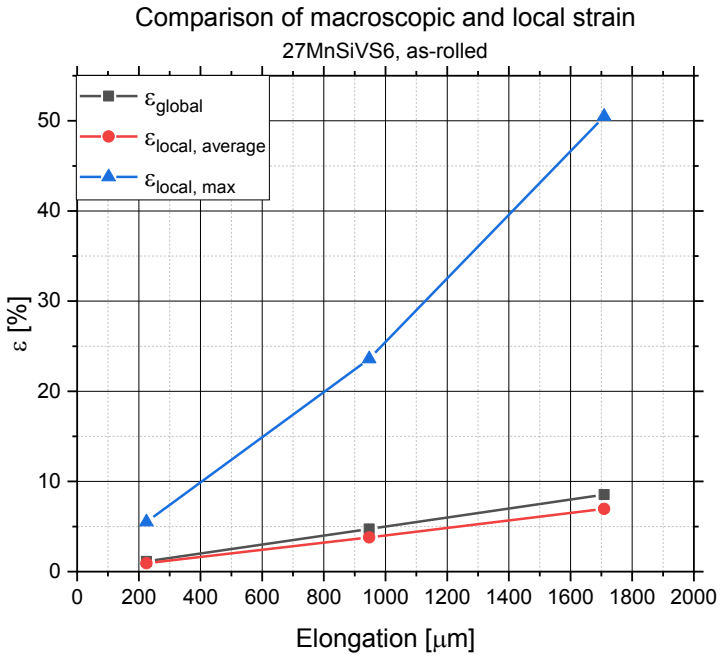

Figure 47: Comparison of macroscopic (global) and local strain – PH-FP-steel

The SEM images taken during the in-situ tensile test of the Q & T steel are shown in Figure 48. At low strain the annealed microstructure with globular formed carbides (Fe_3C) in a ferrite matrix can still clearly be seen. With increasing strain (below 6 % strain) the formation of shear bands due to shear stress in a roughly 45 degree angle to the direction of loading becomes more pronounced. At the end of the experiment (10 % strain), a rough topography of the surface with deformation perpendicular to the observed area and more pronounced shear bands is formed. The underlying grain structure from before the annealing treatment can be seen in the lower half of the SEM image. In comparison to the ferritic-pearlitic microstructure of the PH-FP-steel, the deformation is more uniform due to the homogenized structure of the annealed material. A localisation of deformations near grain boundaries or NMIs cannot be determined from the SEM images, therefore a DIC measurement with the parameters shown in Table 6 is conducted and presented in Figure 49.

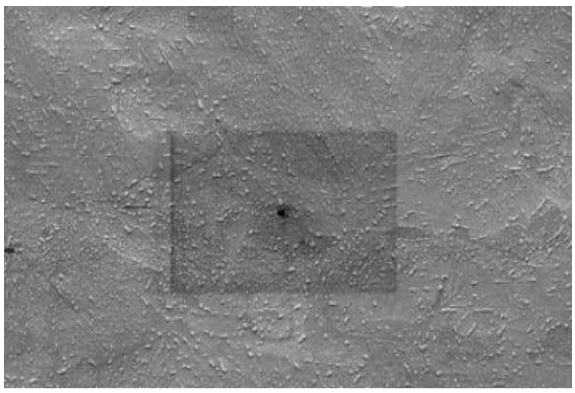

Measurement step 1 – 2 % strain
42CrMo4, annealed

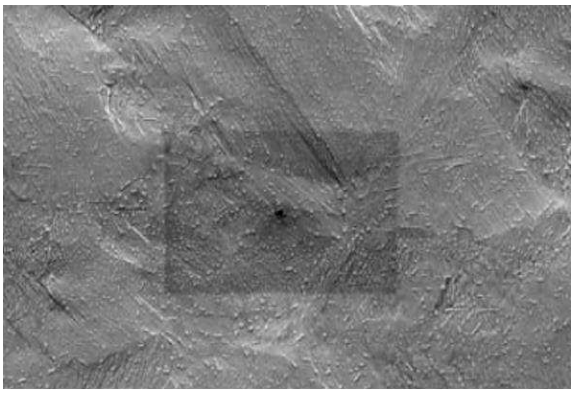

Measurement step 2 – 6 % strain
42CrMo4, annealed

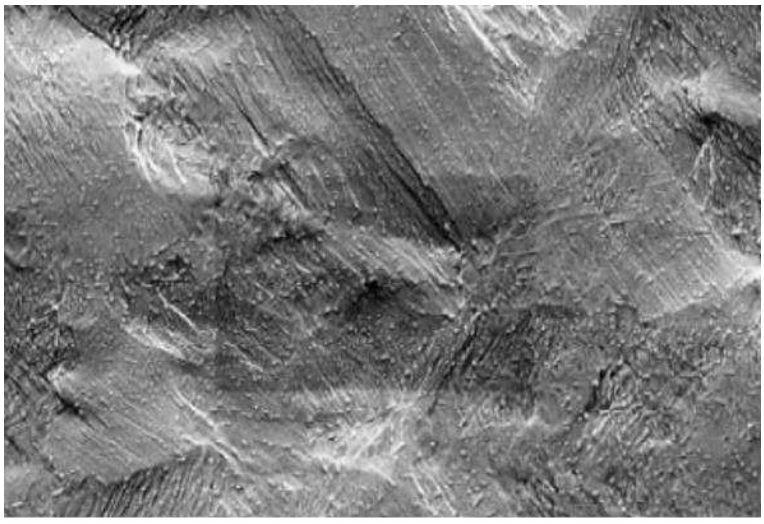

Measurement step 3 – 10 % strain
42CrMo4, annealed

Figure 48: SEM measurements of in-situ tensile tests – 42CrMo4, annealed (Q & T steel)

The DIC measurement of the Q & T steel shows a less pronounced localization and more uniform deformation compared to the PH-FP-steel. With increasing global strain, some areas with a higher measured deformation are detected due to the forming of shear bands, as well as the more rugged topography of the surface. The highest localized strains are measured at areas where the underlying grain structure from before the annealing step becomes visible. In conclusion, 42CrMo4, in annealed condition, shows a more uniform deformation behaviour compared to 27MnSiVS6, as-rolled. To support this observation, the global strains measured at the tensile stage are compared with the local strains measured by DIC. The results are shown in Table 8.

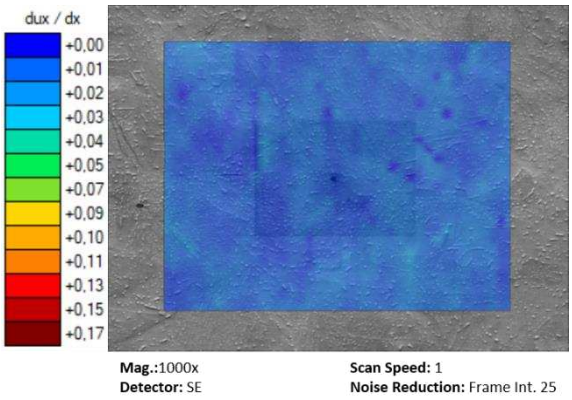

Measurement step 1 – 2 % strain

42CrMo4, annealed

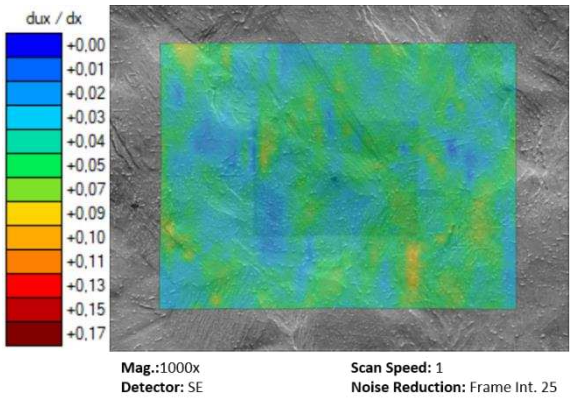

Measurement step 2 – 6 % strain

42CrMo4, annealed

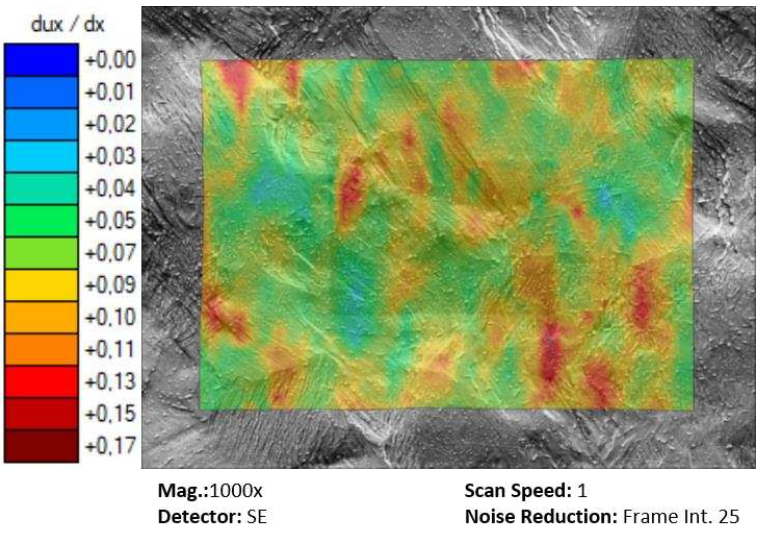

Measurement step 3 – 10 % strain

42CrMo4, annealed

Figure 49: In-situ DIC measurement of 42CrMo4, annealed (Q&T steel)

Table 8: Comparison of global and local strains – 42CrMo4, annealed

Measurement step	**Elongation [µm]**	**ε_{global} [%]**	**$\varepsilon_{local,\ average}$ [%]**	**$\varepsilon_{local,\ max}$ [%]**
1	255	1,28	1,15	3,03
2	1017	5,09	4,33	10,53
3	1800	8,99	7,82	17,15

The global strain (ε_{global}), measured at the tensile stage, and the average local strain ($\varepsilon_{local,\ average}$) show a good alignment over the course of the experiment with the maximum local strain ($\varepsilon_{local,\ max}$) being 2-2,5 times higher (compared to 5-7 times higher with ferritic-pearlitic microstructure) (Figure 50). These results show the more uniform deformation behaviour of an annealed compared to a ferritic-pearlitic microstructure.

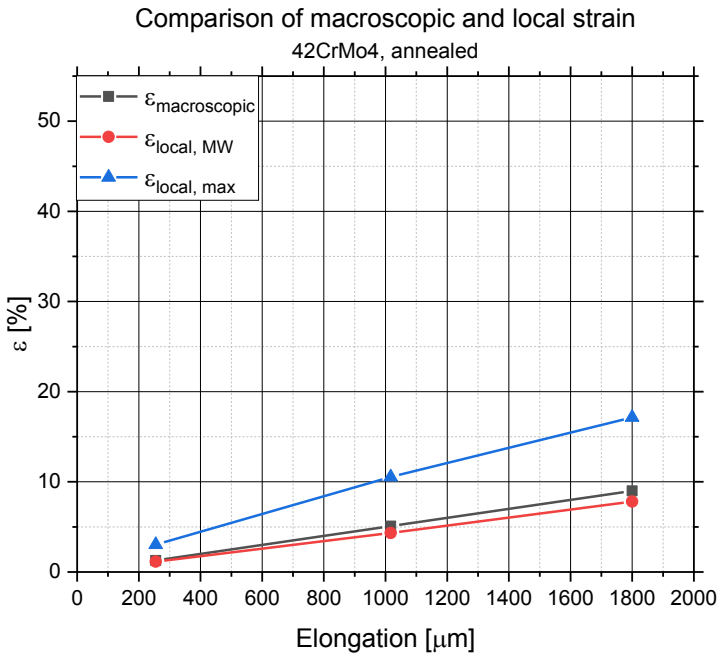

Figure 50: Comparison of macroscopic (global) and local strain – Q&T steel

The fine grained ferritic-pearlitic microstructure of 27MnSiVS6 leads to a reasonable ductility of the material (shown in chapter 3.1) combined with a higher strength due to the high amount of pearlitic grains [1]. The influence of the grain size is presented by high localized strain compared to the measured global strain. In comparison, the annealed microstructure of the Q & T-steel 42CrMo4 with globular Fe_3C precipitations enables better dislocation movement and leads to a uniform deformation and lower localization of strains [12; 22; 23]. The influence of shear strains, in a 45°-angle to the loading direction is clearly visible during forming (seen in Figure 48 and Figure 49).

Therefore, it can be concluded that using DIC with a robust underlying calibration of the imaging and surface preparation methods, the deformation behaviour on a microstructural level can be investigated. In combination with global measurement using tensile testing, digital image correlation methods lead to a better understanding of the material behaviour during forming, concerning, for example, localisation effects.

6. Application-oriented investigation of forming behaviour

Even though the characterisation of material behaviour during forming can be determined using proven experimental methods such as tensile, compression or torsion testing, it is still difficult to predict the deformation behaviour in the production at industrial facilities. This difficulty arises from the difference in stress states of the experimental procedures, for example a uniaxial stress state during uniform deformation in a tensile test, does not represent the stress state in industrial forming operations. Therefore, the need for specialized, application-orientated forming experiments arises. An example for the difficulty is the cold heading process, used in the production of screws and fasteners [8; 99]. This process is a combination of compression and extrusion of the specimen to form the final geometry of fasteners. The exact production process is described in detail in chapters 1 and 2.

Originating from the problem to experimentally depict the forming behaviour of materials during the cold heading step in the production of screws, an application-orientated testing method, the cold heading test (CHT), has been developed. The initial idea of using a lateral extrusion method to depict the material behaviour in the final step of production was presented by Guk et al [60]. This approach of testing is further optimized to deliver replicable results concerning the deformation of low-alloyed steels. The final experimental setup is shown in Figure 21, with the specimen geometry pictured in Figure 22. During the experiments, a servo-hydraulic testing machine of the type walter + bai LFV-T was used. The testing parameters are shown in Table 9.

Table 9: Testing parameters of the utilized machine setup (w + b LFV-T)

Machine type	**Initial force F_{init} [N]**	**Max. force F_{max} [N]**	**Strain rate $\dot{\varphi}$ [1/s]**	**Max. punch stroke s_{max} [mm]**
w+b LFV-T	200	275000	0,1	15

The termination criterion for the experiments was defined by a reduction of the punch force of ΔF = 0,5 % of the current measured force. Through this, the point of failure of the specimen during deformation, due to cracking at the outer diameter of the sample, can be defined accurately. An example of a CHT-specimen after deformation with the crack initiation (green circle) is shown in the following Figure 51.

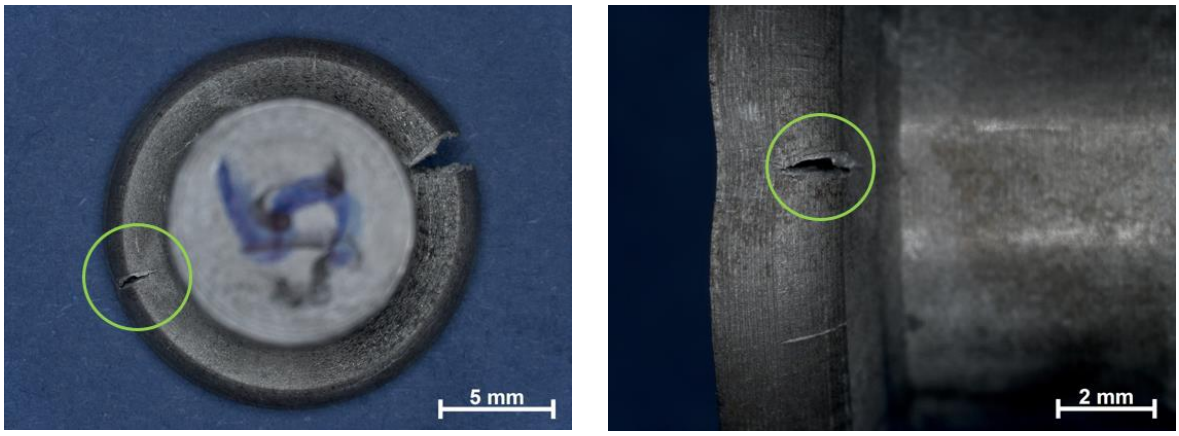

(a) (b)

Figure 51: Example for a CHT-specimen after deformation – 27MnSViVS6, as-rolled
(a) top-down view, (b) side view

The goal of this investigation is to characterize the forming behaviour of the materials investigated using DIC in chapter 5, 27MnSiVS6, as-rolled condition (PH-FP-steel) and 42CrMo4, annealed (Q&T steel), on a macroscopic, application-orientated scale. Therefore, the developed and optimized cold heading test as well as tensile tests are used. Finally, the CHT is implemented in a finite element simulation program, simufact.forming™ V15, to generally evaluate and compare the deformation behaviour quantitatively.

6.1. Forming behaviour of the investigated materials

The optimized cold heading test is used to investigate the forming behaviour of the materials chosen, 27MnSiVS6, as-rolled condition, and 42CrMo4, annealed. Therefore, the results of the experiments are discussed in detail. Furthermore, the damage behaviour of both materials is examined using SEM imaging of tested samples.

6.1.1. Evaluation of the cold heading test (CHT)

The recorded punch force F – strain φ_z in loading direction for selected experiments as well as the average values of 27MnSiVS6, as-rolled, and 42CrMo4, annealed, are pictured in Figure 52 and Figure 53. The force is measured directly at the punch using a calibrated load cell, whereas the strain is calculated from the recorded punch stroke *s* using the following equation 21:

$$\varphi_z = \ln\left(\frac{h_0 - s}{h_0}\right) * (-1) \tag{21}$$

with h_0 being the initial sample height, and *s* the recorded punch stroke. For the PH-FP-steel, the maximum strain due to punch stroke is measured as φ_z = 0,29 with a maximum punch force of F_{max} = 148 kN. In comparison, the maximum strain for the investigated Q&T steel is φ_{max} = 0,85 with a force of F_{max} = 143 kN. The measured values are also shown in Table 10.

Table 10: Measured maximum values for the investigated materials

Material	Strain rate $\dot{\varphi}$ [1/s]	Maximum punch force *F* [N]	Maximum strain φ_z [-]
27MnSiVS6	0,1	148 000	0,29
42CrMo4	0,1	143 000	0,85

It can clearly be seen, that higher strength steel displays a lower maximum strain, with a comparable maximum punch force at crack initiation. These results allow a comparison of the forming behaviour and show a good correlation to the results of the tensile tests (Figure 9), with a higher UTS leading to a lower maximum deformation. Furthermore, the cold heading test demonstrates a high reproducibility of results, when the single experiments are compared to the average measurement values.

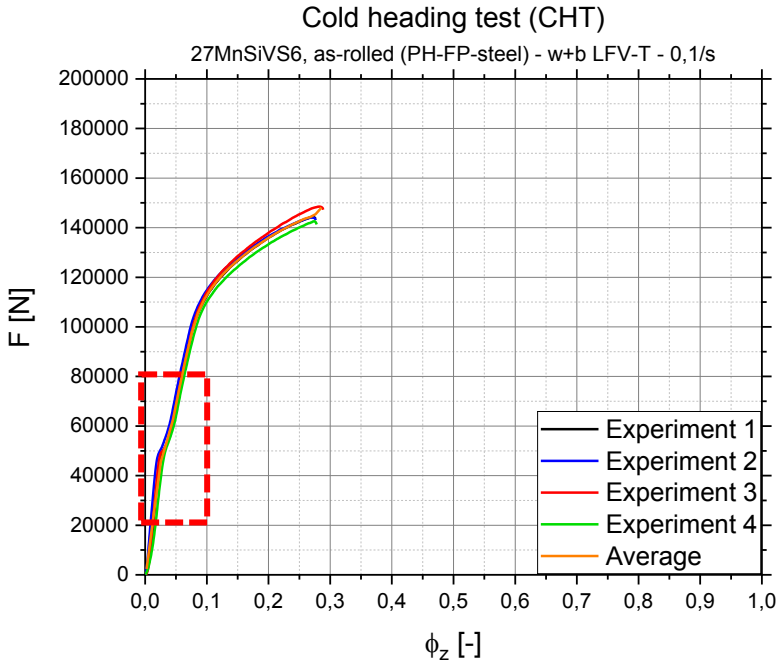

Figure 52: Cold heading test (CHT) – 27MnSivS6, as-rolled (PH-FP-steel), punch force F plotted against strain in punch direction φ_z

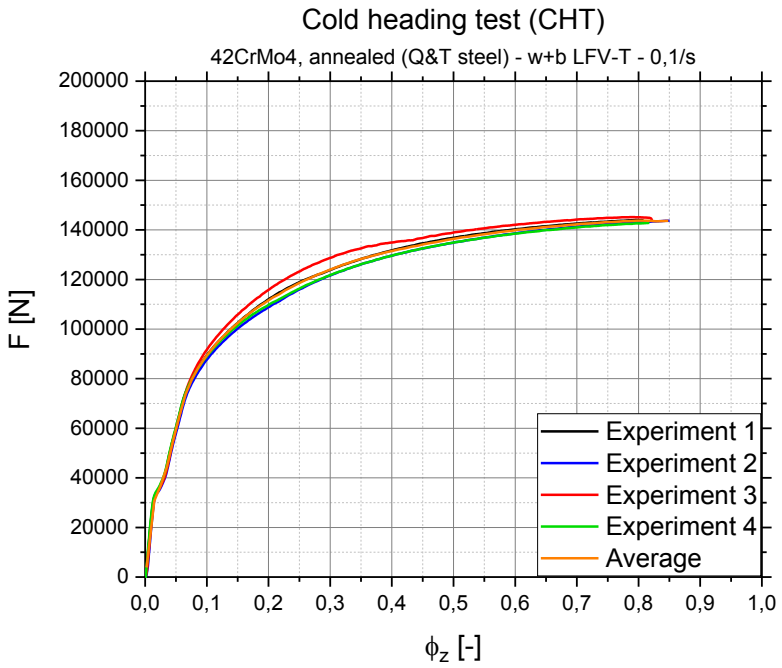

Figure 53: Cold heading test (CHT) – 42CrMo4, annealed (Q&T steel), punch force F plotted against strain in punch direction φ_z

A magnification of the area of the slope change in Figure 52 (red rectangle) is shown in the following Figure 54. The constant force measured after the first bend at $\varphi_z \sim 0{,}025$ occurs due to the elastic deformation and barrelling of the cylindric specimen inside the die in the first step of forming. The punch force *F* increases when the maximum diameter of the sample contacts the inside of the upper part of the die (as seen in Figure 21), and defines the transition from elastic to plastic deformation. The process can be described in three steps; (i) elastic deformation of the sample (barrelling of the cylinder), (ii) filling of the upper part of the die (transition from elastic to plastic deformation) and (iii) plastic deformation and lateral flow of the material into the flange area (Figure 54). The width of the transitioning area is set by the gap between the specimen and the inner diameter of the die and can therefore be set before the experiment.

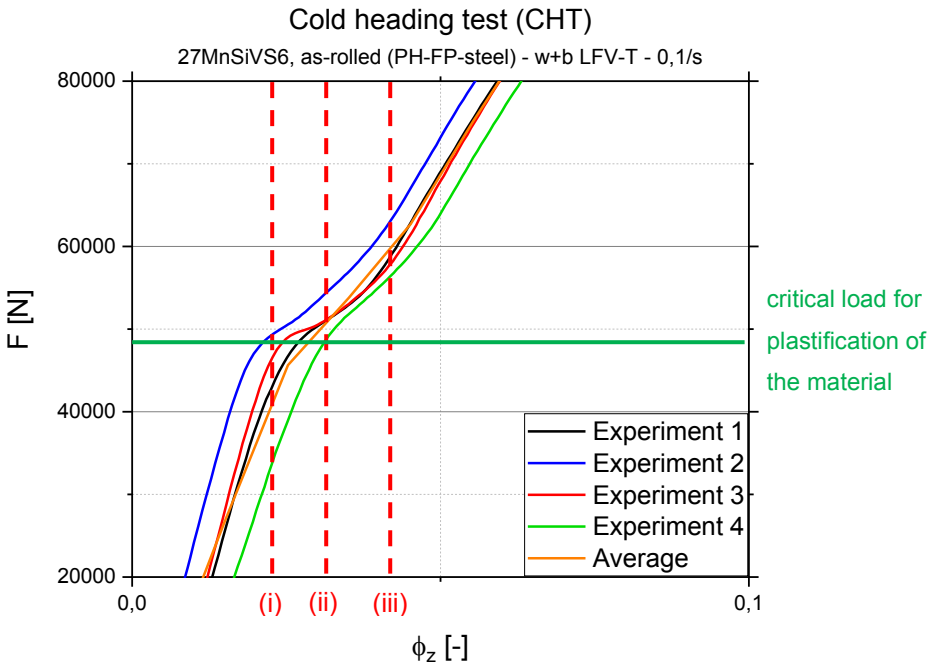

Figure 54: Magnification of the slope change during CHT experiments (red rectangle in Figure 54)

This approach to analyse the forming behaviour yields precise data useful for the design of technical components used for the cold heading of materials. However, to enable a more refined comparison with, for example tensile testing, the maximum punch force F_{max} as well as the strain in punching direction φ_z do not deliver satisfactory results. Therefore, the maximum flow stress as well as the strain in the area of crack initiation (as seen in Figure 51) need to be determined to better describe the influences on deformation behaviour. The two main values calculated are the tangential flow stress kf_t at the largest sample diameter when cracks occur for the first time, and the strain in radial direction φ_r, perpendicular to the punching direction. To evaluate these parameters, the maximum diameter as well as the lateral surface of the sample in the extruded area (as shown, for example, in Figure 64) need to be calculated. Consequentially, the flow stress and the strain during forming can be determined. The maximum diameter D^* is calculated using following equation using volume conservation

$$D^* = 2 * \sqrt{\frac{V_{extruded}}{h_{extruded}*\pi} + r_i^2} \tag{22}$$

with $V_{extruded}$ being the extruded volume of the specimen, $h_{extruded}$ the height of the extruded cylinder ($h_{extruded} = 3\ mm$, as seen in Figure 21) and r_i the inner radius of the die. The maximum lateral area of the extruded sample M^* is calculated as follows

$$M^* = D^* * \pi * h_{extruded} \tag{23}$$

With these parameters the tangential stress at crack onset $k_{f,t}$ and strain in radial direction φ_r can be determined

$$k_{f,t} = \frac{F_{punch}}{M^*} \tag{24}$$

$$\varphi_r = \ln\left(\frac{d_0+(D^*-d_0)}{d_0}\right) \tag{25}$$

with d_0 being the initial specimen diameter (d_0 = 10,40 ± 0,05 mm, as seen in Figure 22). These calculations represent an estimation of the maximum strain dependent on the extruded volume in the flange. Firstly, due to consistency of the volume of the specimen, the height of the flange reduces with increasing diameter of the deformed sample. Therefore, a slight difference between calculated maximum diameter D^* and the real diameter of the pressed specimen as well as the calculated radial strain φ_r occurs. Secondly, $k_{f,t}$ is influenced by friction at the die during deformation as well as the deformation speed. For this reasons, the tangential stress at crack onset is dependent on the experimental setup of the CHT.

For PH-FP-steel, the maximum strain in radial direction is φ_r = 0,49, with a tangential stress at crack initiation of $k_{f,t}$ = 918 MPa, and maximum average stress of $k_{f,tmax}$ = 944 MPa. In comparison, 42CrMo4, in annealed condition, shows a maximum strain of φ_r = 0,81, with flow stress at cracking $k_{f,t}$ = 653 MPa and a maximum stress of $k_{f,tmax}$ = 805 MPa (Table 11).

Table 11: Calculated values of the investigated materials

Material	**$k_{f,t}$ [MPa]**	**$k_{f,tmax}$ [MPa]**	**Maximum strain φ_r [-]**
27MnSiVS6	914	944	0,49
42CrMo4	653	805	0,81

The measured flow curves are presented in Figure 55 and Figure 56. The flow stress at the beginning of deformation is zero, as plastic deformation and therefore increase in flow stress starts with the filling of the upper part of the die (Figure 21). After reaching a maximum ($k_{f,tmax}$), the $k_{f,t}$ values decrease due to the onset of cracking inside the specimen and a subsequent decrease in material strength.

The measured stress values show a decent alignment with the UTS measured in tensile testing, with the results shown in Table 12. However, the influence of friction between the surface of the specimen and the die as well as compressive stresses during deformation using CHT have to be taken into account. A thorough investigation of the stress state during cold heading using FE-simulation is shown in chapter 6.2.

Table 12: Comparison of tensile tests with CHT

Material	$UTS_{tensile}$ [MPa]	$k_{f,t}$ [MPa]	$k_{f,tmax}$ [MPa]
27MnSiVS6, as-rolled	780	914	944
42CrMo4, annealed	561	653	805

The results indicate, with a maximum of flow stress during the deformation, that damaging occurs inside the specimen before the failure due to crack opening at the surface. To further investigate the damaging behaviour during the cold heading testing, samples of both materials are prepared and examined using a SEM (Zeiss CrossBeam 340).

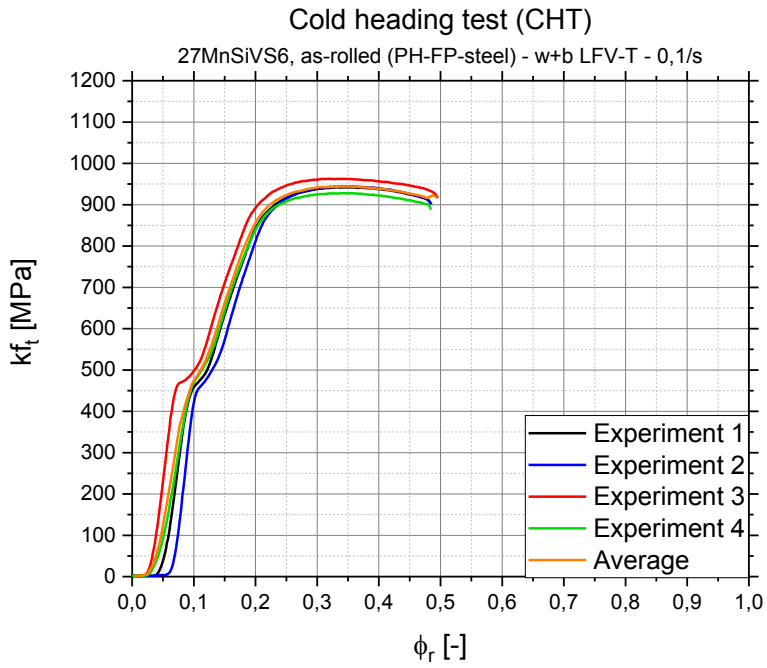

Figure 55: Cold heading test –27MnSiVS6, as-rolled (PH-FP-steel), tangential flow stress $k_{f,t}$ plotted against radial strain φ_r

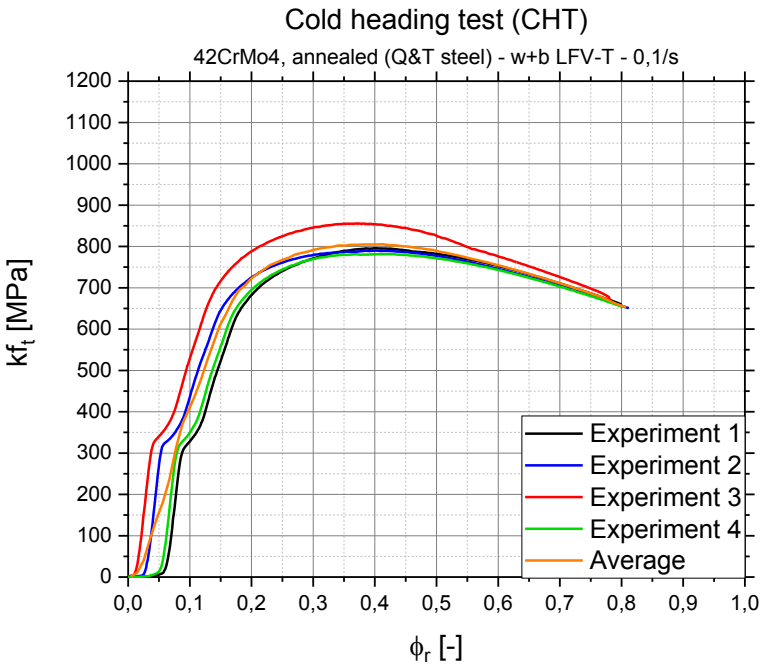

Figure 56: Cold heading test – 42CrMo4, annealed (Q&T steel), tangential flow stress $k_{f,t}$ plotted against radial strain φ_r

6.1.2. Damaging behaviour of the investigated materials

The damage behaviour of the chosen materials, 27MnSiVS6, as-rolled condition, and 42CrMo4, annealed is examined using SEM imaging on a Zeiss CrossBeam 340 at the Materials Center Leoben (MCL). The goal is to investigate the influence of non-metallic inclusions (NMI) and porosity on the formability. Therefore, samples are prepared using cross-section ion cutting in tangential direction at the outer diameter of tested samples, as well as parallel to the surface of the extruded flange. The specimens and the cutting and polishing directions, with the processed planes are shown in Figure 57. The sections are placed in areas of the samples where no cracks are visible at the surface, as only the damage behaviour inside the materials is investigated.

Figure 57: Cutting directions for cross section ion cutting – tangential (red arrows) and parallel (green arrows), (a) 27MnSiVS6, as-rolled, (b) 42CrMo4, annealed

The images of 27MnSiVS6, as-rolled, at magnifications of 1000x and 3000x for the cross sections parallel to the extruded flange (red arrows in Figure 57) are shown in Figure 58, for sections tangential to the surface (green arrows) in Figure 59. Parallel to the flange, voids forming uniformly around non-metallic inclusions (NMI) are visible. At higher magnifications, delaminations of the matrix material at the NMI are visible as potential starting points for cracks in the material. The inclusions examined are manganese-sulfides (MnS) as well as titanium-nitrides (TiN). The formation of these inclusions leads to an overall reduction in fracture toughness as well as tensile properties of the material [132–134]. No voids can be measured in the matrix material around the impurities, but in the case of TiN and MnS, cracking of the NMI is clearly visible.

In the section tangential to the lateral surface of the sample, stretching of the inclusion in the direction of the highest tensile stress can be examined. This stretching leads to comparable delamination and cracking effects at MnS and TiN as in the parallel sections. Again, no voids can be measured in the vicinity of the NMI. Therefore, it can be assumed, that the initial damaging of the PH-FP-steel starts at inclusions due to the delamination of the matrix and the

cracking phenomenon of inclusions and propagates to the lateral surface of the flange. There, the crack opens at the outer surface due to high tensile stresses in tangential direction, as can be seen in Figure 51 and Figure 55.

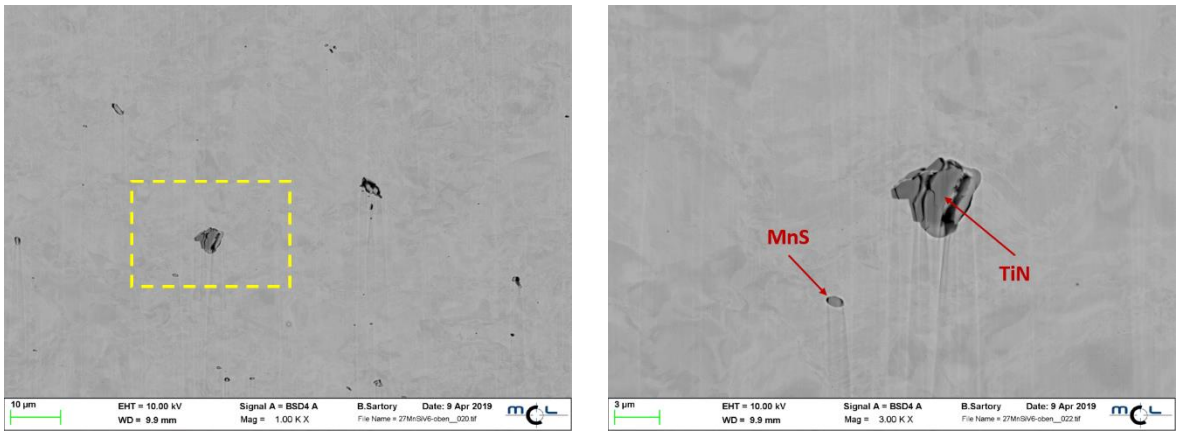

(a) (b)

Figure 58: Inclusions in a cutting surface parallel the flange – 27MnSiVS6, as-rolled
(a) 1000x magnification, (b) 3000x magnification

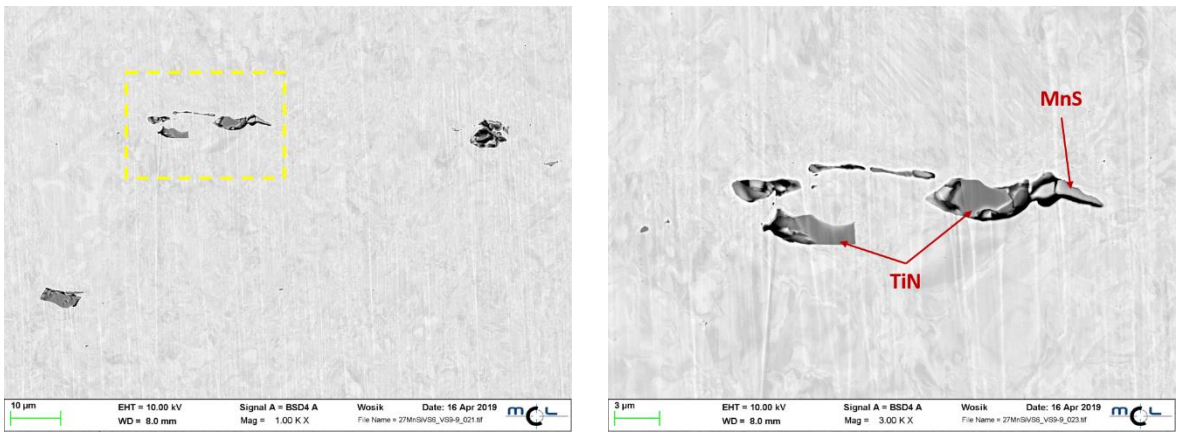

(a) (b)

Figure 59: Inclusions in a section tangential to the surface – 27MnSiVS6, as-rolled
(a) 1000x magnification, (b) 3000x magnification

The cross section images of 42CrMo4, annealed, parallel to the flange are shown in Figure 60 and tangential to the lateral surface in Figure 61. In comparison to the PH-FP-steel sample, high porosity can be measured across the section parallel to the extruded flange. Additionally, delamination of the matrix material in the direction of the highest tensile stress can be seen at a non-metallic inclusion (Al_2O_3 and CaS). In the porosity at the NMI, crack growth is clearly visible (red circle).

The cut tangential to the lateral surface of the flange shows lower porosity than the parallel section, with the highest pore density in the area around the impurity (Figure 61). Again, delamination of the matrix material from the inclusion (Al_2O_3 and CaS) as well as stretching of pores in the direction of the highest tensile stress can be detected. The high porosity is a sign

of a high percentage of ductile damage, which can be deduced from the high radial strain at the end of the heading experiment of φ_r = 0,81. [10; 52; 135; 136]

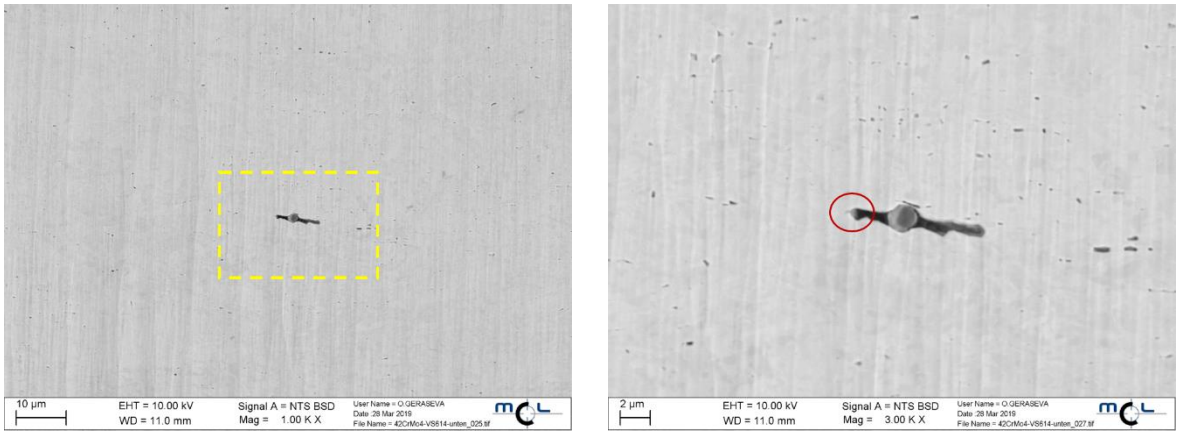

(a) (b)

Figure 60: Inclusions in a cutting surface parallel the flange – 42CrMo4, annealed
(a) 1000x magnification, (b) 3000x magnification

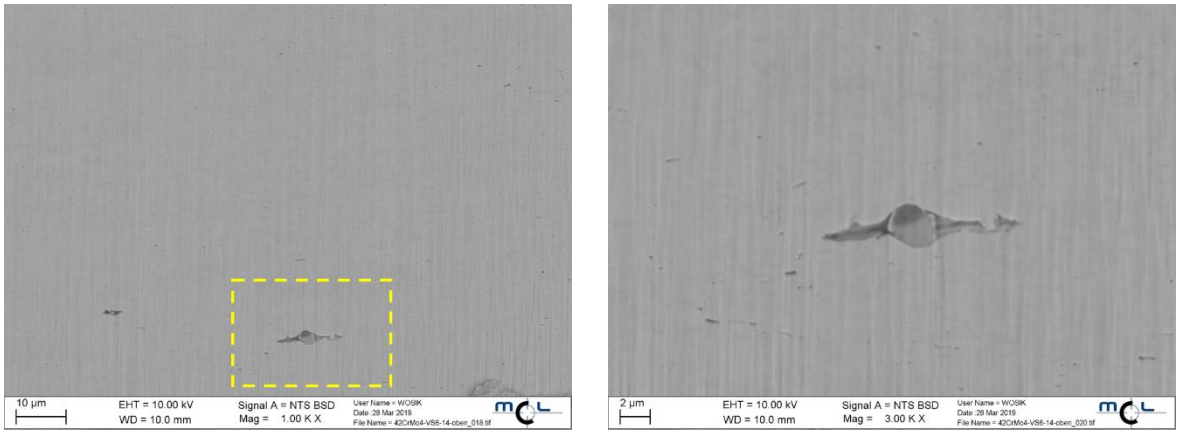

(a) (b)

Figure 61: Inclusions in a section tangential to the surface – 42CrMo4, annealed
(a) 1000x magnification, (b) 3000x magnification

In conclusion, the main microstructural influences on the damaging behaviour of the investigated materials are the delamination of the matrix at non-metallic inclusions, the cracking of nitride-based NMI and, at high radial strains, the formation of high porosity during the experiment. The delamination can be accounted to the high tensile stresses during the cold heading test, while the cracking of inclusions typically appears due to high compression stresses during deformation [10].

In accordance with the investigations using in-situ tensile testing and DIC measurements, the formability of the materials can be described in detail. At low strains during the in-situ experiments, the influence of shear stress on the deformation is shown. Due to the low amount of deformation, no onset of voids at NMI or grain boundaries is determined. Therefore, the CHT enables the investigation of the damaging behaviour at higher strains, where the principal causes for material failure are the delamination of the matrix at NMI as well as the cracking of

inclusions. At higher strains, in ductile materials, the onset of voids further weakens the microstructure which ultimately leads to material failure.

However, to enable a better comparability of the CHT and in-situ tensile tests, the multiaxial stress state during cold heading is investigated by using finite element simulation. The results of the FE-simulation are discussed in the following chapter.

6.2. Finite element simulation of the cold heading test

The experimental cold heading test enables an application-orientated evaluation of materials, as presented in chapter 6.1. However, for example the damage behaviour, can only be evaluated after the end of the experiment. Therefore, to better describe the stress state and damaging behaviour during deformation and to enable comparison with tensile experiments, the CHT is implemented into the finite element (FE) simulation program simufact.forming™ version 15.

In this software, the testing setup is built as shown in Figure 23. To optimize the calculation time, the cold heading test is defined as a two-dimensional (2D) model. This approach is justifiable due to the rotationally symmetric experimental setup and leads to a significant reduction in computation time as well as a reduced error rate due to the lower amount of elements of which the sample is constructed. The materials investigated with the FE-simulation are 27MnSiVS6, as-rolled condition, and 42CrMo4, annealed. The flow stress data are determined using standard compression testing with Rastegaev specimens to reduce the influence of friction at the end faces of the specimen [25]. The geometry of the samples used in the experiments is shown in Figure 62 (a), with the specifications as follows (Table 13):

Table 13: Specifications for rastegeav specimen

d_0 [mm]	h_0 [mm]	t_0/h_0 [-]	u_0/d_0 [-]
12	18	1/100	1/20

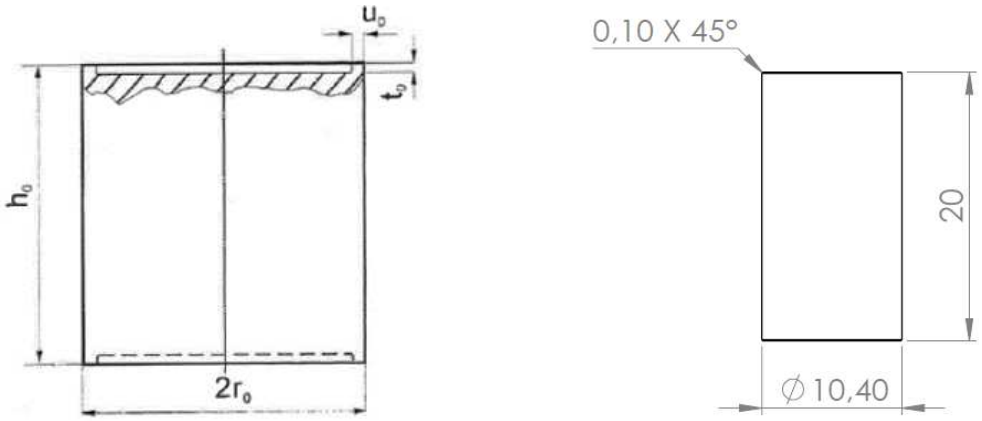

(a) (b)

Figure 62: Sample geometries used (a) for compression testing – Rastegaev specimen, (b) cold heading testing

The stress-strain data is recorded for strain rates of $\dot{\varphi} = 0{,}1/s$, $\dot{\varphi} = 0{,}5/s$, $\dot{\varphi} = 1/s$ and $\dot{\varphi} = 50/s$ and is implemented into a material model for both materials. The thermal characteristics, e.g. c_p, α and ρ depending on temperature, are taken from online databases (Dr. Sommer Prüflabor) [114]. An overview of the testing parameters as well as sample specifications is given in Table 14. The damage parameters D_{Oyane} for determining the damaging behaviour are calculated with equation 26 using compression testing and represent empirical values with validity only for the selected material [69; 75; 137].

$$D_{Oyane} = \int \left(A + \frac{\sigma_m}{\sigma_V}\right) d\bar{\varepsilon} = \int \left(A + \frac{\left(\frac{\sigma_1+\sigma_2+\sigma_3}{3}\right)}{\frac{1}{\sqrt{2}}\sqrt{(\sigma_1-\sigma_2)^2+(\sigma_2-\sigma_3)^2+(\sigma_3-\sigma_1)^2}}\right) d\bar{\varepsilon} \tag{26}$$

Table 14: Testing and sample specifications for the FE-simulation

Testing parameters	**Sample specifications**
• Punch velocity v_{punch} = 4 mm/s (equals $\dot{\varphi} = 0{,}1/s$) • Max. punch stroke s_{punch} = 17 mm • Frame rigidity realised with a generic spring in punch direction with k = 150 kN/mm • Calculation steps CS = 1360 (equals 1 step per 0,0125 mm punch stroke)	• Geometry: h_0 = 20 mm, d_0 = 10,4 mm • Friction parameters: μ = 0,05, m = 0,1 • Meshing parameters: Advancing Front Quad Meshing with element edge length l_0 = 0,15 mm • Element number E = 4522 elements • Damage parameters: $D_{Oyane,AFP}$ = 0,0689 and $D_{Oyane,Q\&T}$ = 0,13334

The results of the simulation with the parameters in Table 14 implemented, in comparison to the experimental data, are presented in Figure 63, with the data points at higher strains ($\varphi_{27MnSiVS6,Sim} > 0,3$ and $\varphi_{42CrMo4,Sim} > 0,8$) deleted for a clearer comparison. The FE-calculations show a good correlation with the experiments, especially for 27MnSiVS6, in as-rolled condition. For 42CrMo4, annealed, a deviation of simulation results above strain values of $\varphi > 0,3$ is visible, with a maximum difference in punch force *F* of $\Delta F \sim 10$ kN. This can be explained by the large strain at the point of failure and the complicated friction condition between sample surface and die. The pronounced up and down movement of the simulation results occur due to two separate influences. Firstly, the rounded die edge where lateral extrusion starts cannot be rendered in full detail, therefore the simulation skips around the edge every few calculation steps leading to increase in punch force *F* with a subsequent decline. Secondly, remeshing steps are conducted periodically to reduce the error rate of the calculations, which leads to a slight distortion of calculated results. These calculation inaccuracies lead to the serrated form of the force-strain curve. If this is taken into account, the simulation results show a good correlation with the experimental data of the cold heading testing.

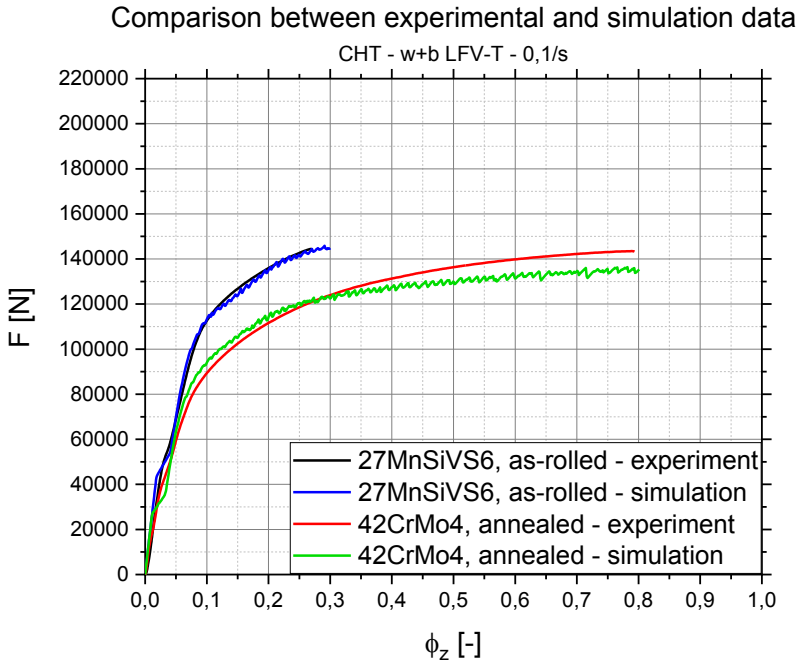

Figure 63: Comparison between experimental and simulation data – CHT at w+b LFV-T

With the simulation setup implemented, the stress-strain and damage behaviour of the investigated materials during cold heading can be calculated. To enable measurement inside the sample during testing, a point tracking method at areas of highest stress and strain, the outer diameter of the extruded flange (particles 1-5), is used. With this approach, the effective plastic strain φ_V, the effective stress σ_V, the hydrostatic stress state σ_m, the triaxiality σ_m/σ_V, the tangential stress σ_t and the damage factor C can be calculated in detail. The point tracking

setup is shown in Figure 64 (a), with the deformation of the specimen at the end of the simulation shown in Figure 64 (b), (c).

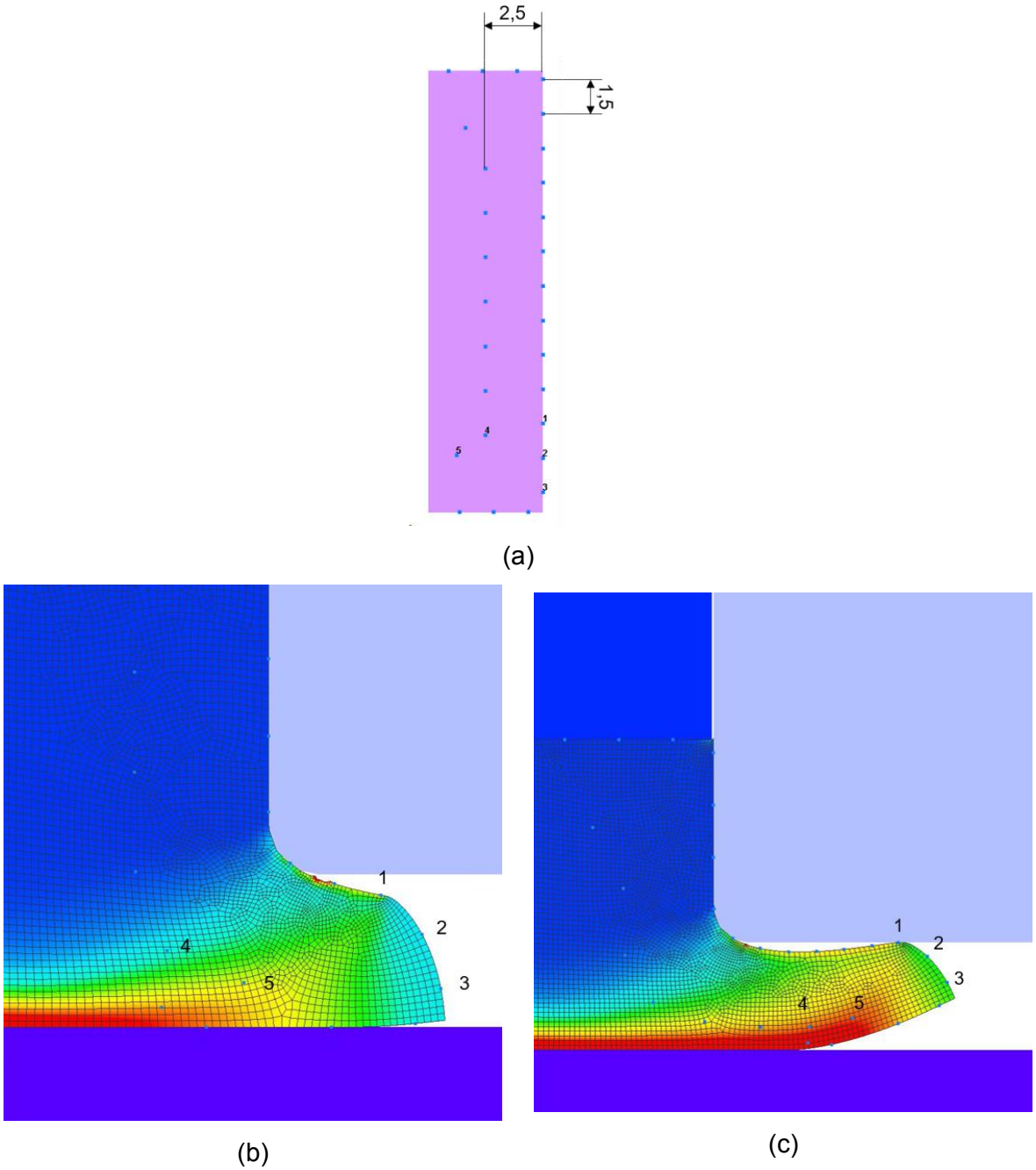

Figure 64: Particle tracking – (a) initial setup of unloaded specimen,
(b) 27MnSiVS6, as-rolled a thet end of simulation, (c) 42CrMo4, annealed at the end of simulation [83]

6.2.1. Particle tracking – 27MnSiVS6, as-rolled condition

The results of the particle tracking for 27MnSiVS6, as-rolled are presented in the following chapter. Particles 1-3 are placed at the outer diameter of the extruded flange, whereas particles 4 and 5 are placed at a distance 2,5 mm from the lateral surface (Figure 64). The calculated stress and damage values are plotted in relationship to the strain in punch direction to enable a comparison with the results of the cold heading test, for example in Figure 52 or Figure 63.

The maximum strain in punch direction is calculated at $\varphi_{z,max} = 0{,}3$. The deformation of the sample was calculated up to a maximum strain of $\varphi_z = 1{,}0$ as similar simulation setups were used for both investigated materials. For the PH-FP-steel this leads to inconsistencies of the calculations at higher strains ($\varphi \sim 0{,}8$) which are not taken into account in the discussion due to the failure of the material at lower strains during the experiments.

The effective stress σ_V (Figure 65, (a)) is calculated with a value of $\sigma_V \sim 850$-900 MPa on the outer surface of the sample, which is reached at a strain of $\varphi_V = 0{,}1$ and stays in this range until the end of the experiment. Inside the specimen (particle 4 and 5) the effective stress increases during the whole test, with the maximum of $\sigma_V = 1050$ MPa reached at the end of deformation. To get a better understanding of the stress state during forming, Figure 65, (b) displays the calculated hydrostatic stress σ_m. At the lateral surface, throughout the entire experiment, a tensile stress state is depicted, with a maximum value of $\sigma_m = 450$ MPa reached at the failure of the specimen during experiments. Inside the sample, a compressive stress state is measured. Hence, the tangential stresses measured in the CHT in the experimental procedures (Figure 55), which are higher than the ultimate tensile (UTS) stress of the material, can be explained by the supporting effect of compressive stresses during forming.

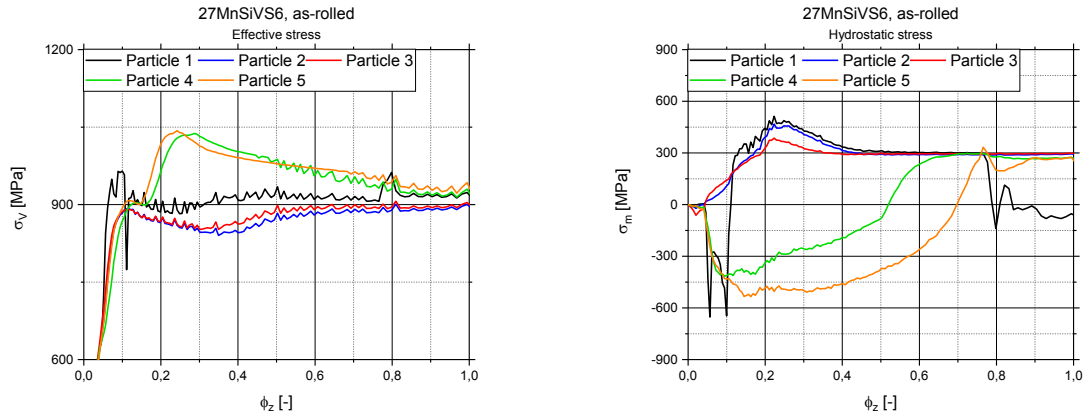

(a) (b)

Figure 65: Simulation results for effective stress σ_V and hydrostatic stress σ_m – 27MnSiVS6, as-rolled
(a) effective stress σ_V, (b) hydrostatic stress σ_m

If the triaxiality $T_T = \sigma_m/\sigma_V$ Figure 66 is examined, the measurements at the lateral surface show a transition from a compressive stress state of $T_T < 0$ at the beginning of deformation to a tensile stress state at the end of deformation wit $T_T \sim 0{,}3$. At this value, the stress state can be considered uniaxial in tensile direction [10; 52]. With this result, the stretching of voids, as examined in the microscopic investigation in chapter 6.1.2 (Figure 59), can be explained. The occurrence of compressive and tensile stresses during forming is also clearly visible by analysing the tangential stresses, which are shown in Figure 67. The calculated values of

σ_t ~ 900 MPa demonstrate a good correlation with the results of the experiments. Therefore, this again shows the validity of the simulation setup for the evaluation of the cold heading test.

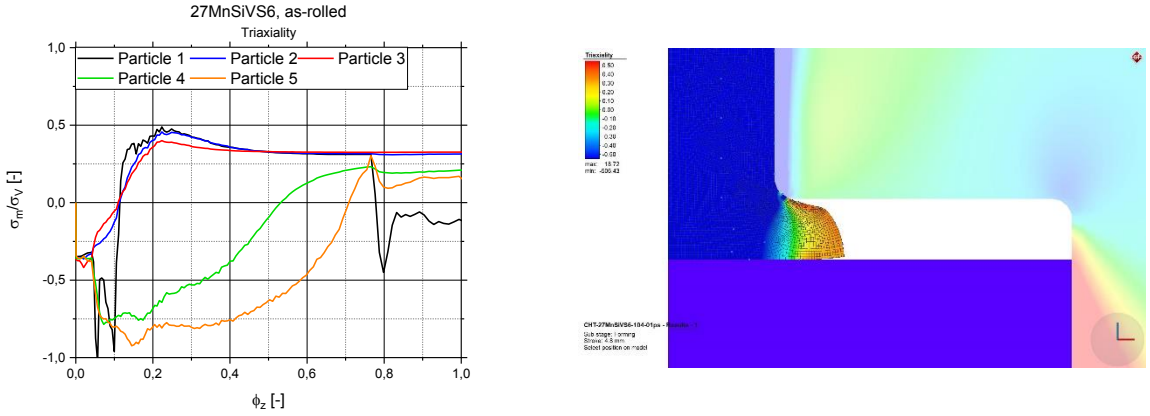

(a) (b)

Figure 66: Simulation results for triaxiality σ_m/σ_V – 27MnSiVS6, as-rolled
(a) simulation results, (b) image of the simulation

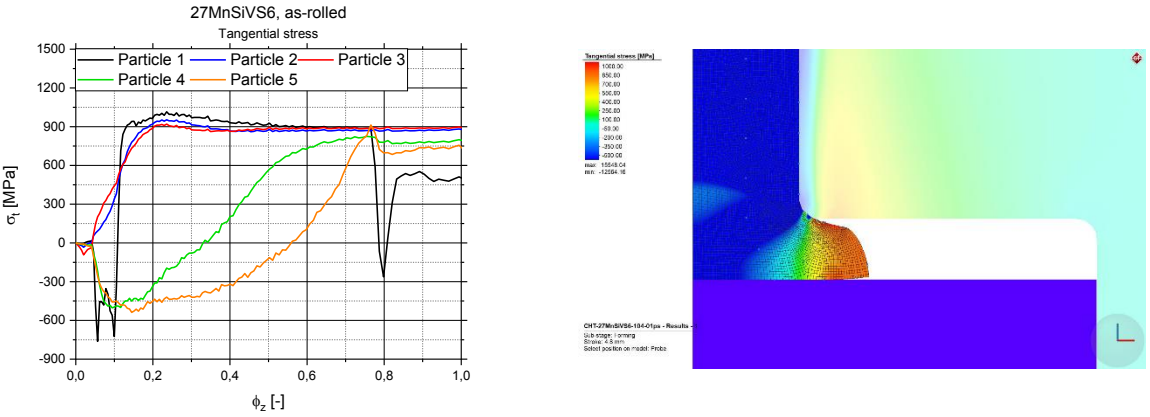

(a) (b)

Figure 67: Simulation results for tangential stress σ_t – 27MnSiVS6, as-rolled
(a) simulation results, (b) image of the simulation

By calculation of the damage behaviour using the Oyane/Ayada ductile damage model (as seen in equation (26)) the beginning of material failure can be determined, as seen in Figure 68 (a). At the end of the experiment at φ_z = 0,3, a damage factor of C = 0,09 is measured. If compared to the experimental results (Figure 68, (b)) the results show a good correlation with the location of crack initiation during cold heading experiments. Therefore, the damaging behaviour of the material in the CHT can be assessed with the optimised simulation setup, but it has to be taken into account, that this damage model is only valid for the current material.

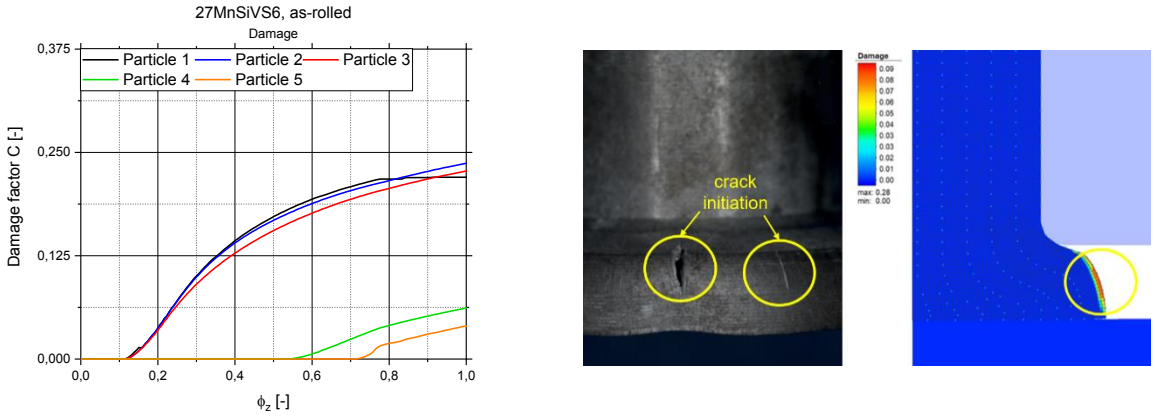

(a) (b)

Figure 68: Simulation results for Damage factor C – 27MnSiVS6, as-rolled
(a) simulation results, (b) comparison of simulation with experiments

An overview of the simulated results for material 27MnSiVS6, as-rolled condition is shown in Table 15. If the results are compared with the material properties measured using tensile tests, the tangential stress σ_t at the surface (particles 1-3) exceeds the UTS during tensile testing. Due to compressive stresses inside the specimen, this behaviour is possible at very low strains. At higher strains, the maximum workability of the material is reached and damage occurs. By calculating the hydrostatic stress σ_m the multi-axial stress state during deformation is shown, with tensile stresses at the lateral surface, which ultimately lead to crack initiation, and compressive stresses inside the sample. The triaxiality factor *T* also describes a tensile stress state at the surface and a compressive stress-state inside the specimen (as shown in chapter 2.3., Figure 5).

Table 15: Overview of simulation results for 27MnSiVS6, as-rolled

Strain φ_z [-]	**σ_v [MPa]**	**σ_m [-]**	**$T_T = \sigma_m/\sigma_v$ [-]**	**σ_t [MPa]**	**C [-]**
Lateral surface (particles 1-3, average)					
0,1	912	32	-0,17	167	0
0,2	885	392	0,40	941	0,04
0,3	864	386	0,40	919	0,09
Inside of specimen (particles 4 & 5, average)					
0,1	889	-416	-0,77	-468	0
0,2	999	-399	-0,73	-373	0
0,3	1022	-378	-0,67	-249	0

These results allow the description of the formability behaviour of the material during heading processes, which enable an application-oriented examination. However, the calculations using

finite element simulation depend on the experimental data collected by a combination of the developed cold heading test and tensile testing.

6.2.2. Particle tracking – 42CrMo4, annealed condition

Comparable to the calculations using FE simulation for the PF-PH steel, the results of the particle tracking for 42CrMo4, annealed, are presented in this chapter. Particles 1-3 are placed at the outer diameter of the extruded flange, whereas particles 4 and 5 are placed at a distance 2,5 mm from the lateral surface (Figure 64, (a)). The calculated stress and damage values are plotted in relationship to the strain in punch direction to enable a relation with the results of the cold heading test, for example in Figure 53 or Figure 63. The maximum strain in punch direction is measured at $\varphi_{z,max}$ = 0,8 during experiments.

The effective stress σ_V is calculated with a maximum value of $\sigma_{V,max}$ = 825 MPa at the inside of the sample (Figure 69,(a)). On the lateral surface, the measured stress increases over the course of the simulation up to a value of σ_V = 750 MPa. The hydrostatic stress values show tensile stresses at the extruded flange surface (Figure 69, (b)). The initial compressive stress state of particle 1 can be explained by the beginning of extrusion, where the specimen is pressed into the die. With increasing deformation during the experiment, the mean hydrostatic stress state shifts to a fully tensile stress state at the end at φ_z = 0,8. Similarly to the PH-FP-steel, the exaggeration of the measured tangential stresses during the experiment, as shown in Figure 56, can be explained by the supporting effect of the compressive stresses inside the material.

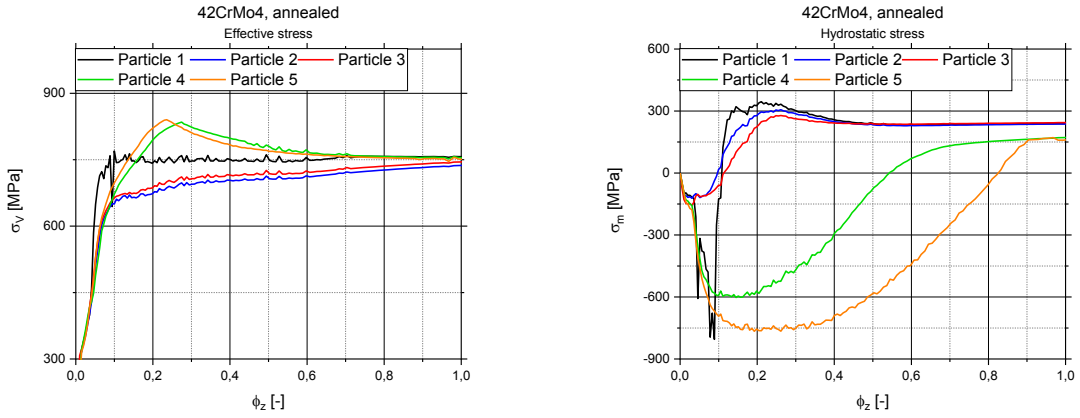

(a) (b)

Figure 69: Simulation results for effective stress σ_V and hydrostatic stress σ_m – 42CrMo4, annealed (a) effective stress σ_V, (b) hydrostatic stress σ_m

The triaxiality $T_T = \sigma_m/\sigma_V$ calculated (Figure 70) shows a uniaxial tensile stress state in the lateral surface of the flange at the end of the deformation. Due to the high strain at failure, particles 4 and 5 on the inside of the sample show comparable triaxiality values as the particles 1-3 at the surface. When the tangential stresses, shown in Figure 71, are viewed, the calculated results show a good correlation to the experiments (Figure 56). At the end of the

simulation, at all investigated particles tensile stresses are calculated. Due to the high stresses compared to the UTS measured in tensile tests and the high deformation at failure, the pronounced form of the cracking in comparison with 27MnSiVS6, as-rolled can be explained (as seen in Figure 72, (b)).

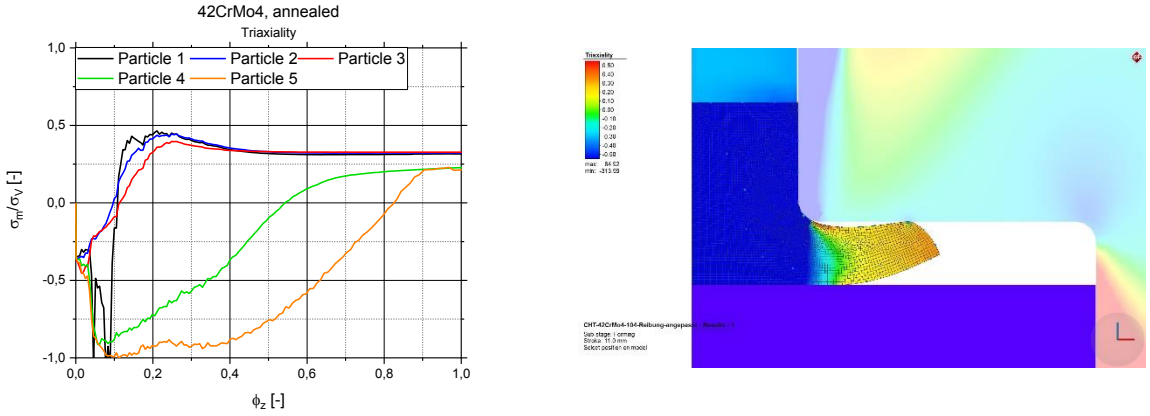

Figure 70: Simulation results for triaxiality σ_m/σ_V – 42CrMo4, annealed
(a) simulation results, (b) image of the simulation

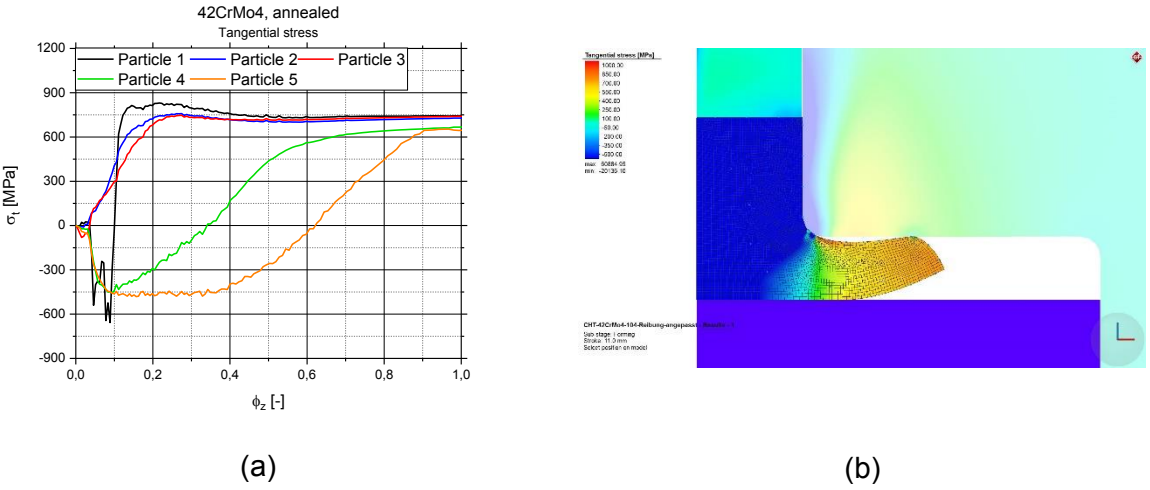

Figure 71: Simulation results for tangential stress σ_t – 42CrMo4, annealed
(a) simulation results, (b) image of the simulation

With the Oyane/Ayada ductile damage model, the area of damage initiation can be estimated in more detail. If the simulation and experimental results are compared, the calculated data shown in Figure 72, (b) display a good correlation. At the end of deformation at a strain of $\varphi_z = 0{,}8$, a damage factor of $C \sim 0{,}23$ is calculated. This factor can be used to predict the damage behaviour of the Q&T steel, but it has to be taken into account that this results are only valid for each material individually.

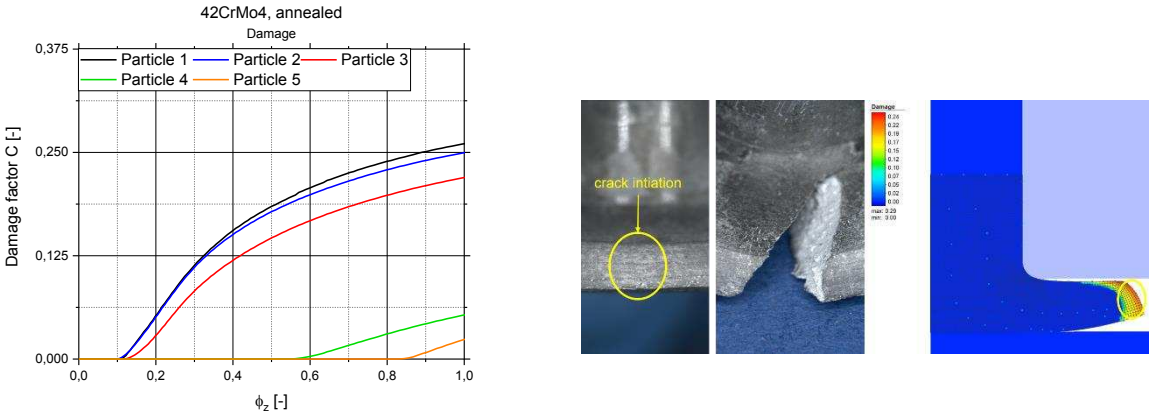

(a) (b)

Figure 72: Simulation results for Damage factor C – 42CrMo4, annealed
(a) simulation results, (b) comparison of simulation with experiments

An overview of the results of the finite element simulation is shown in Table 16. Compared to the PH-FP steel, the effective stresses are reduced in the same magnitude as the UTS in the tensile tests conducted in chapter 3. The multi-axial stress state in the sample during deformation is shown in the mean stress values calculated for the lateral surface and the inside of the specimen. Due to the high degree of deformation until crack formation on the outer diameter, the stress state at particles 4 and 5 shifts to mostly tensile stress. This behaviour is also validated by the triaxiality values, which shows a tensile stress state at the outer diameter (T_T ~ 0,3 at high strain, as shown in Figure 5) and a shift from compressive to tensile behaviour at particles 4 and 5. The evolution of tangential stresses σ_t during cold heading testing enable the depiction of cracking of the specimen at the point of failure, a crack all the way through the flange. Due to the high tangential stresses on the inside of the sample at high strains, the supporting effects of compressive stresses decrease with increased deformation, which leads to abrupt crack propagation through the flange. The damage factor C increases with increasing strains up to a value of $C = 0{,}23$ at the lateral surface. However, the damage factor is valid only for the investigated steel grade and production charge.

Table 16: Overview of simulation results for 42CrMo4, annealed

Strain φ_z [-]	σ_V [MPa]	σ_m [-]	$T_T = \sigma_m/\sigma_V$ [-]	σ_t [MPa]	C [-]
Lateral surface (particles 1-3, average)					
0,2	705	287	0,41	752	0,05
0,4	723	249	0,35	731	0,14
0,6	727	233	0,32	717	0,19
0,8	740	238	0,32	730	0,23
Inside of specimen (particles 4 & 5, average)					
0,2	812	-572	-0,83	-388	0
0,4	791	-491	-0,63	-113	0
0,6	764	-173	-0,24	271	0
0,8	746	63	0,08	558	0,02

In conclusion, if combined with microstructural evaluation (chapter 6.1.1) and finite element simulation, the cold heading test (CHT) delivers valuable information concerning the forming and damage behaviour of a material in heading operations. Furthermore, due to the tensile stress state at the lateral surface of the extruded flange (tangential stresses at the outer diameter of the flange, parallel to the face side of the specimen), a comparison with standard tensile testing is possible. With the support of finite element calculations concerning the stress state inside of the specimen, the exaggerated tangential stress values measured during forming (shown in Figure 55 and Figure 56) are defined and can be used for the design of new materials. With the presented approach for investigations of forming behaviour, the CHT can be used as a tool for the determination of the material behaviour during multiaxial stress states and the comparison of different heading materials.

7. Investigation of influences on forming behaviour using CHT

The application-oriented investigation of the material behaviour during forming using the cold heading test (CHT) has been presented in chapter 6. It is shown, that this optimized testing method provides valuable information concerning the stress-state during deformation of materials and therefore results can be compared to standard approaches such as tensile experiments. Therefore, the CHT can be used for investigation of different influences on the material behaviour. In this chapter, the influence of variations in testing setups, strain rate and microstructure due to heat treatment is examined in detail. Finally, the behaviour of different steel grades used for the manufacturing of screws and fasteners during cold heading will be shown and discussed.

7.1. Influence of variations in testing setups

To investigate the influence of strain rate on the material behaviour a different testing setup is used, as the machine deployed for the experiments in chapter 6 is limited to a maximum strain rate of $\dot{\varphi} = \frac{0,1}{s}$. Therefore, a new servo-hydraulic machine system with the same experimental setup, manufactured by Servotest, was used, with a maximum of $\dot{\varphi} = \frac{10}{s}$. A comparison of the machine parameters is shown in Table 17.

Table 17: Comparison of the different testing setups

Machine type	Initial force F_{init} [N]	Max. force F_{max} [N]	Strain rate $\dot{\varphi}$ [1/s]	Max. punch stroke s_{max} [mm]
w+b LFV-T	200	275000	0,1	15
Servotest	40000	330000	0,1; 1; 10	15

The same materials as used in chapter 6, 27MnSiVS6, as-rolled, and 42CrMo4, annealed, are investigated with the new machine type. The results are shown in Figure 73 and Table 18. In comparison, the Servotest setup shows a higher measured punch stroke as well as punch force over the course of the experiment. For the PH-FP-steel as well as the Q&T steel, the difference is in the range of ΔF ~ 10 kN. If the flow stress and strain data at the lateral surface of the extruded flange is calculated, the difference in strain is minimal, but the stress shifts to higher values during the experiment. These results occur due to the increased initial force at the Servotest setup compared to the w+b LFV-T setup ($F_{Servotest}$: F_{LFV-T} = 40 000 N : 200 N). This approach decreases the accuracy of measurements during elastic deformation, but

increases the precision of plastic deformation data, as the experiment is started at the beginning of the extrusion process.

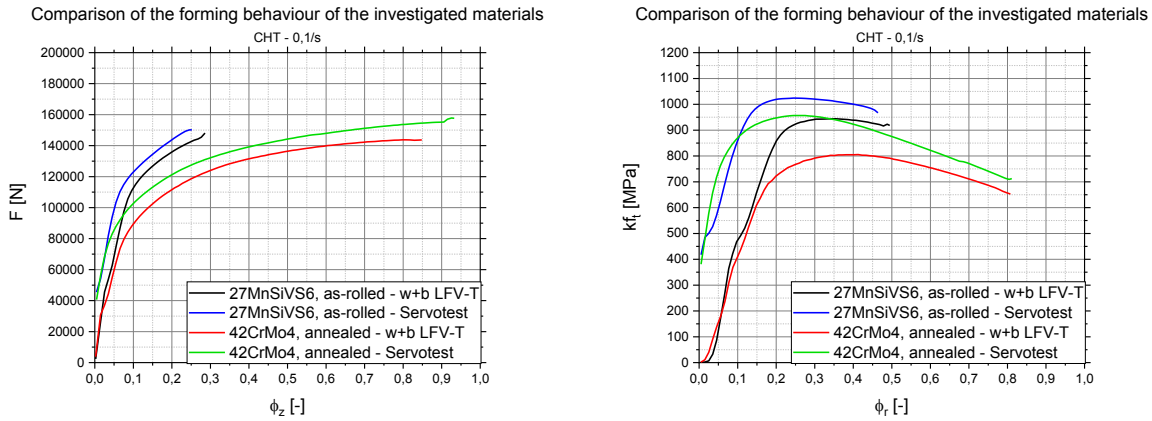

(a) (b)

Figure 73: Influence of the testing setup on the forming behaviour of the investigated materials
(a) punch force F plotted against strain in punch direction φ_z,
(b) tangential stress $k_{f,t}$ plotted against radial strain φ_r

Table 18: Comparison of the two testing setups

Material	**Test setup**	**φ_z [-]**	**F_{max} [N]**	**$\varphi_{r,max}$ [-]**	**$k_{f,t}$ [MPa]**	**φ_r [-]**	**$k_{f,t,max}$ [MPa]**
27MnSiVS6, as-rolled	w+b LFV-T	0,29	148100	0,49	918	0,35	943
	Servotest	0,25	150200	0,46	967	0,25	1024
42CrMo4, annealed	w+b LFV-T	0,85	143700	0,81	653	0,40	805
	Servotest	0,93	157600	0,81	712	0,27	957

The results of the comparison of two selected testing setups (Table 18) show a significant difference if the flow stress and strain are investigated. In conclusion, the cold heading test shows a high sensitivity concerning the initial condition of the experiment and setup. This has to be taken into account if only the material behaviour is investigated. Therefore, for the following experiments, the Servotest setup is used, as the range of plastic deformation is presented in more detail.

7.2. Influence of strain rate on formability

After the selection of the testing setup, the investigation of influences on material behaviour is conducted in detail. As an industrial cold heading process is typically conducted at strain rates of $\dot{\varphi} > \frac{1}{s}$, CHT experiments are executed at strain rates of up to $\dot{\varphi} = \frac{10}{s}$ [8; 99]. The increase in strain rate normally leads to an increase in flow stress in combination with a decrease in maximum strain at failure [110]. If the force-strain behaviour in punch direction is investigated, PH-FP-steel shows only a small influence of a strain rate increase, as seen in Figure 74, (a) and Table 19. If the flow stress and radial strain at the lateral surface is examined (Figure 74, (b)), the maximum measured flow stress increases with higher strain rate followed by a decrease at $\dot{\varphi} = \frac{10}{s}$. The maximum radial strain is not influenced by a strain rate increase.

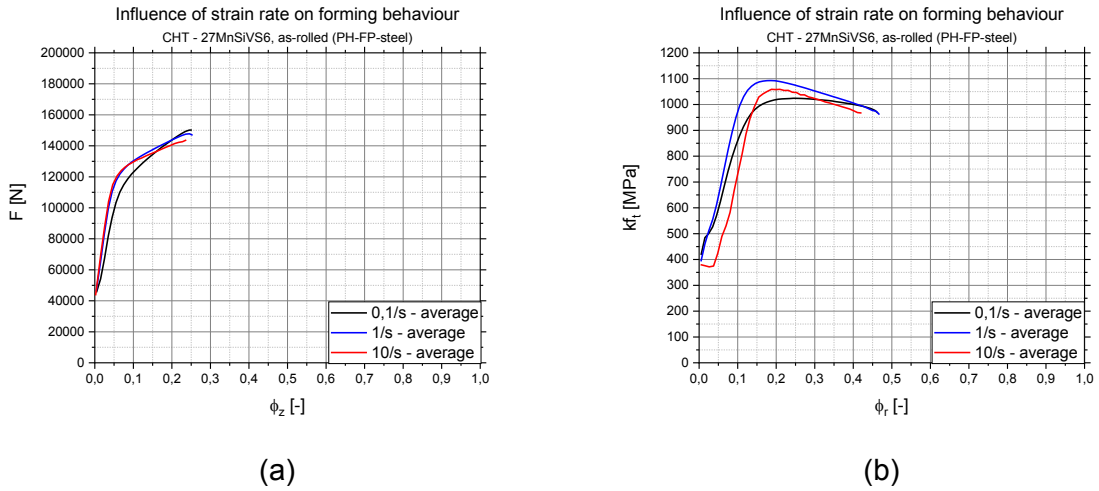

(a) (b)

Figure 74: Influence of strain rate on the forming behaviour – 27MnSiVS6, as-rolled
(a) punch force F plotted against strain in punch direction φ_z,
(b) tangential stress $k_{f,t}$ plotted against radial strain φ_r

The investigated Q & T steel displays an overall decrease of materials strength as well as maximum measured strain in forming and radial direction, as shown in Figure 75 and Table 19. These results show a contradicting behaviour as is presented in literature [110]. Therefore it can be assumed, that a temperature increase, which is not measured during the experiment, may lead to the recorded decrease in flow stress and strain.

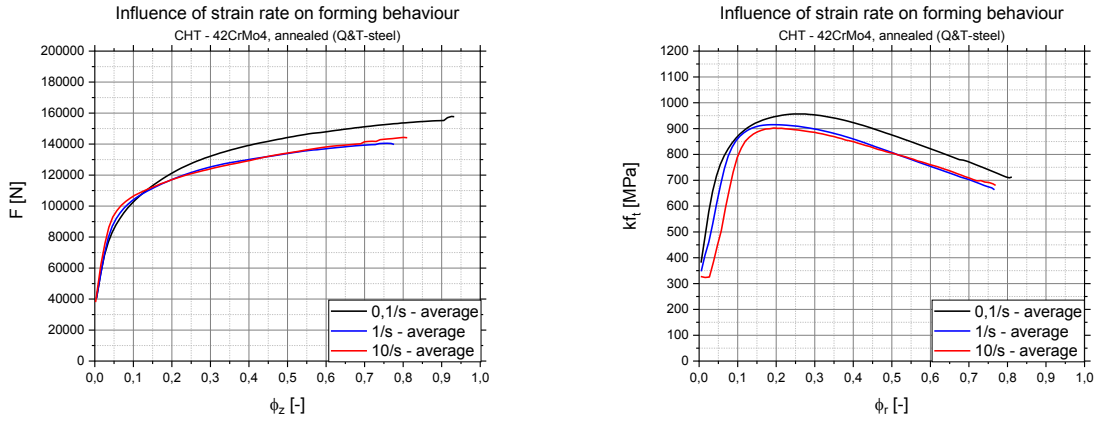

(a) (b)

Figure 75: Influence of strain rate on the forming behaviour – 42CrMo4, annealed
(a) punch force F plotted against strain in punch direction φ_z,
(b) tangential flow stress $k_{f,t}$ plotted against radial strain φ_r

Table 19: Influence of strain rate on the investigated materials – 27MnSiVS6, as-rolled and 42CrMo4, annealed

Material	$\dot{\varphi}$ **[1/s]**	$\varphi_{z,\,max}$ **[-]**	F_{max} **[N]**	$\varphi_{r,max}$ **[-]**	$k_{f,t}$ **[MPa]**	φ_r **[-]**	$k_{f,t,max}$ **[MPa]**
27MnSiVS6, as-rolled	0,1	0,25	150200	0,46	967	0,25	1024
	1	0,25	146900	0,47	961	0,19	1093
	10	0,23	143700	0,42	967	0,21	1059
42CrMo4, annealed	0,1	0,93	157600	0,81	712	0,27	957
	1	0,78	139800	0,76	663	0,19	915
	10	0,81	144100	0,77	680	0,21	901

The results of the experiments show a divergent behaviour of the investigated materials. Precipitation hardening ferritic-pearlitic steel (PH-FP steel) shows a slight increase of the maximum flow stress in combination with a decrease of maximum strain at higher deformation speed. On the other hand, annealed steel (Q & T steel) displays a differing behaviour, with a decrease in flow stress and radial strain. Both investigated materials display a shift of the maximum flow stress at higher strains, with the maximum of $k_{f,t}$ occurring at lower radial strains with increasing deformation velocity.

The CHT shows a high degree of accuracy concerning the maximum measured force/stress during deformation, as seen in Figure 75. From these results it can be concluded that the cold heading test setup is suitable for the determination of the influence of strain rate increases on the forming behaviour of materials.

7.3. Influence of variations in microstructure through heat treatment

The main task of the cold heading test setup is to investigate influences, e.g. strain rate or microstructure, on the forming behaviour of different materials. In preceding chapters, the optimization and the development of the testing setup have been discussed in detail. In a further investigation of the accuracy of the cold heading setup, the influence of different microstructure formations on the material behaviour is examined using the CHT. Therefore, different heat treatments are conducted for the main investigated materials, 27MnSiVS6, as-rolled, and 42CrMo4, annealed. The heat treatments are as follows [109; 116; 138]:

- 27MnSiVS6, as-rolled condition
    - Heat treatment 1 – austenitisation at 850 °C for 1800 s, followed by cooling with a cooling rate of ΔK = 0,01 K/s
    - Heat treatment 2 – austenitisation at 850 °C for 1800 s followed by cooling with a cooling rate of 1 K/s
- 42CrMo4, annealed condtition
    - Heat treatment 1 – austenitisation at 850 °C for 1200 s followed by quenching in water (ΔK ~ 100 K/s) and a tempering step with treatment at 710 °C for 25200 s followed by furnace cooling (ΔK ~ 0,1-1 K/s)
    - Heat treatment 2 – austenitisation at 850 °C for 1800 s, followed by cooling with a cooling rate of ΔK = 0,01 K/s
    - Heat treatment 3 – austenitisation at 850 °C for 1800 s followed by furnace cooling (ΔK ~ 0,1-1 K/s) to 650 °C, held for 1500 °C finished by cooling in air (ΔK ~ 5 K/s)

The details are shown in chapter 4.4, with the results of tensile and cold heading testing presented below.

For PH-FP steel, the heat treatments, compared to the reference condition, show an overall reduction in ultimate tensile strength (UTS) as well as maximum elongation at failure, as shown in Figure 76, (a) and Table 20. This occurs due to a variation in pearlite lamella distance, which has been adjusted in the heat treatment. For the Q & T steel, comparable results are measured, with a reduction in elongation but a slight increase in UTS. Additionally, compared to the annealed condition, the heat treated microstructures show a pronounced yield strength (Figure 76, (b)). This behaviour is due to the forming of a pearlitic-ferritic microstructure at heat treatment as opposed to the annealed microstructure with globular formed carbides (Fe_3C) in the reference material.

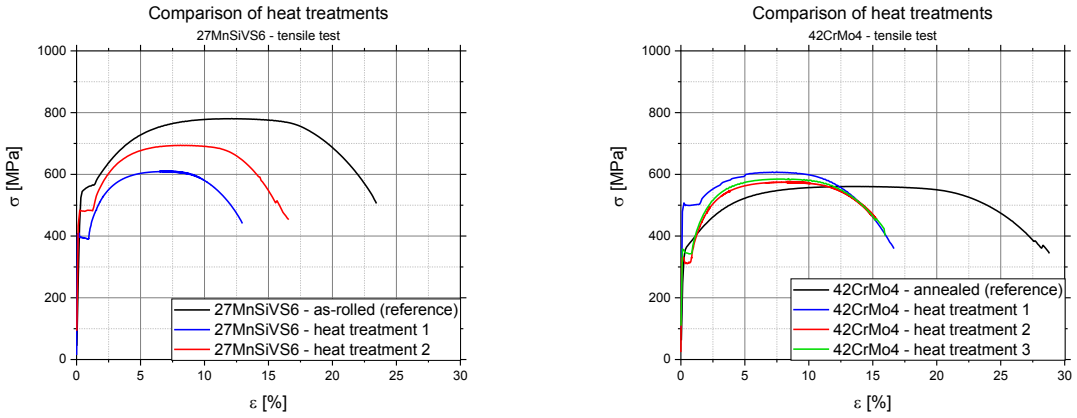

(a) (b)

Figure 76: Influence of heat treatments – tensile testing
(a) 27MnSiVS6, (b) 42CrM4

Table 20: Tensile test – influence of heat treatments – 27MnSiVS6 and 42CrMo4

Material	**$R_{p0,2}$ [MPa]**	**R_m [MPa]**	**A_g [%]**	**A [%]**
27MnSiVS6 reference	546	780	11,5	23,3
27MnSiVS6 heat treatment 1	406	611	6,5	12,9
27MnSiVS6 heat treatment 2	484	694	8,2	16,6
42CrMo4 reference	360	561	13,2	28,2
42CrMo4 heat treatment 1	507	607	7,2	16,7
42CrMo4 heat treatment 2	331	577	8,2	15,3
42CrMo4 heat treatment 3	353	584	7,9	15,9

The cold heading experiments for 27MnSiVS6 are conducted at strain rates ranging from $\dot{\varphi} = \frac{0,1}{s}$ to $\dot{\varphi} = \frac{10}{s}$ and present a comparable material behaviour as examined in the tensile test. The reference condition shows the highest punch force and lowest maximum strain before failure. With increasing pearlite lamellar distance (Distance HT 1 > Distance HT 2) the material strength decreases, with an increase in maximum deformability as shown in Figure 77. When the tangential flow stress at the lateral surface of the extruded flange and the radial strain is measured, the forming behaviour shows high correlation with the results of the tensile test. At

higher strain rates, the experimental results are comparable to the investigations in chapter 7.2, with an increase in flow stress at $\dot{\varphi} = \frac{1}{s}$, followed by a decrease at $\dot{\varphi} = \frac{10}{s}$. This result is caused by a possible heating up of the specimen inside the die during forming. The order of material strength influenced by heat treatments does not change with increasing strain rate.

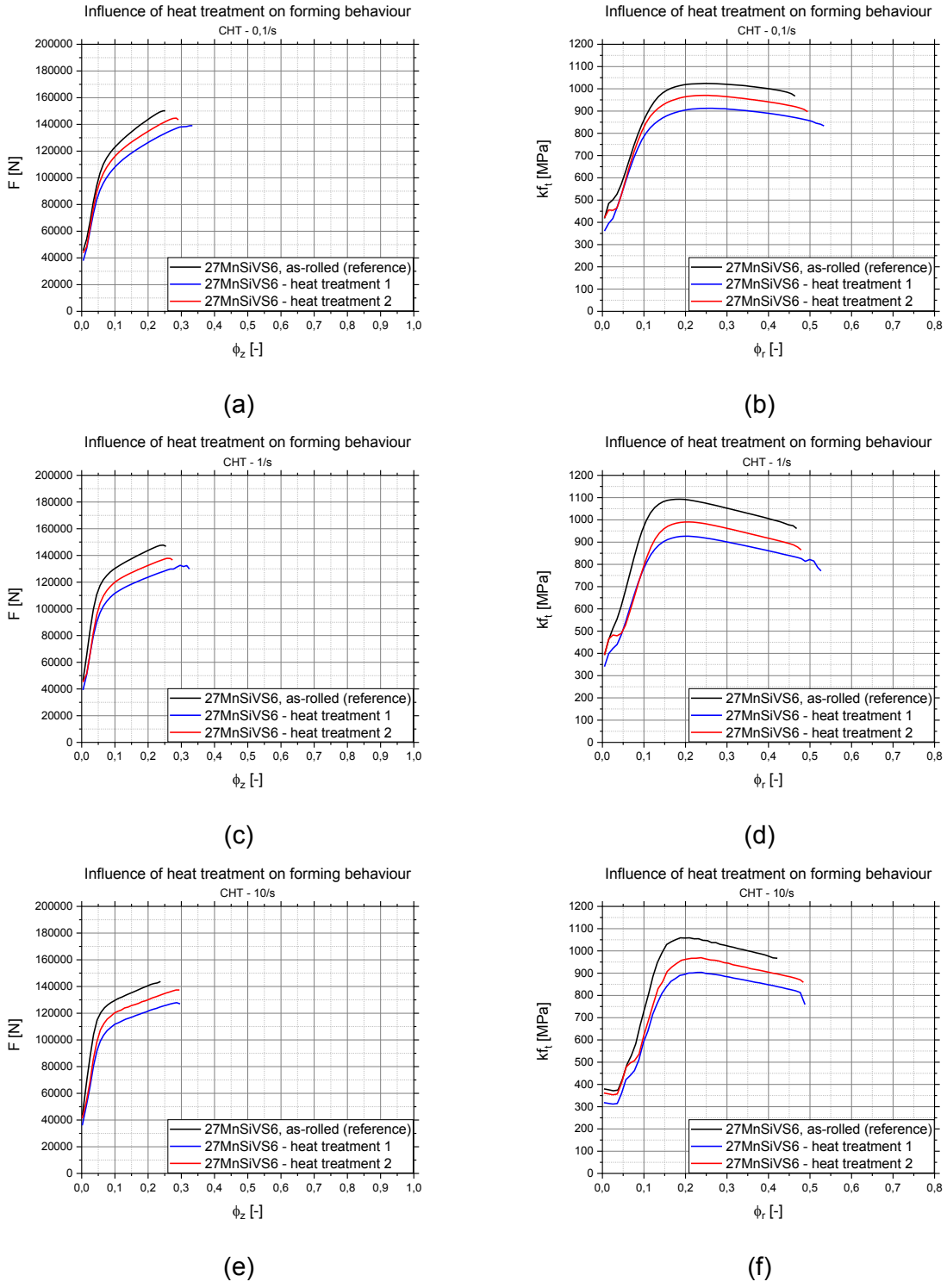

Figure 77: Influence of heat treatment on the forming behaviour – 27MnSiVS6
(a), (c), (e) punch force F plotted against strain in punch direction φ_z with $\dot{\varphi} = \frac{0,1}{s}, \frac{1}{s}$ *and* $\frac{10}{s}$,
(b), (d), (f) tangential flow stress $k_{f,t}$ plotted against radial strain φ_r with $\dot{\varphi} = \frac{0,1}{s}, \frac{1}{s}$ *and* $\frac{10}{s}$

Table 21: CHT – influence of heat treatments – 27MnSiVS6, as-rolled (PH-FP-steel)

Material	$\dot{\varphi}$ [1/s]	$\varphi_{z,\,max}$ [-]	F_{max} [N]	$\varphi_{r,max}$ [-]	$k_{f,t}$ [MPa]	φ_r [-]	$k_{f,t,max}$ [MPa]
Reference	0,1	0,25	150200	0,46	967	0,25	1024
	1	0,25	146900	0,47	961	0,19	1093
	10	0,23	143700	0,42	967	0,21	1059
Heat treatment 1	0,1	0,33	13900	0,53	833	0,25	912
	1	0,32	129900	0,53	770	0,21	927
	10	0,30	127000	0,49	759	0,24	904
Heat treatment 2	0,1	0,29	143300	0,49	897	0,25	971
	1	0,27	136600	0,48	865	0,21	990
	10	0,29	137400	0,48	859	0,24	969

The cold heading tests for 42CrMo4 are conducted the same way as for the PH-FP steel with strain rates ranging from $\dot{\varphi} = \frac{0,1}{s}$ to $\dot{\varphi} = \frac{10}{s}$. At low deformation speed, the quenched and tempered microstructure shows the highest strength as well as maximum strain. Concerning measured punch force, heat treatment 2 and 3 are comparable with the reference condition but with a strong decrease in maximum strain at failure, as is shown in Figure 78 and Table 22. At higher strain rates, the different microstructures show a deformation behaviour similarly to the reference structure with a decrease in punch force at $\dot{\varphi} = \frac{1}{s}$ and a slight increase at $\dot{\varphi} = \frac{10}{s}$. The maximum strain at failure decreases overall with increasing strain rate. The calculated values for tangential stress and radial strain display the same material behaviour as examined at the experiments in chapter 7.2.

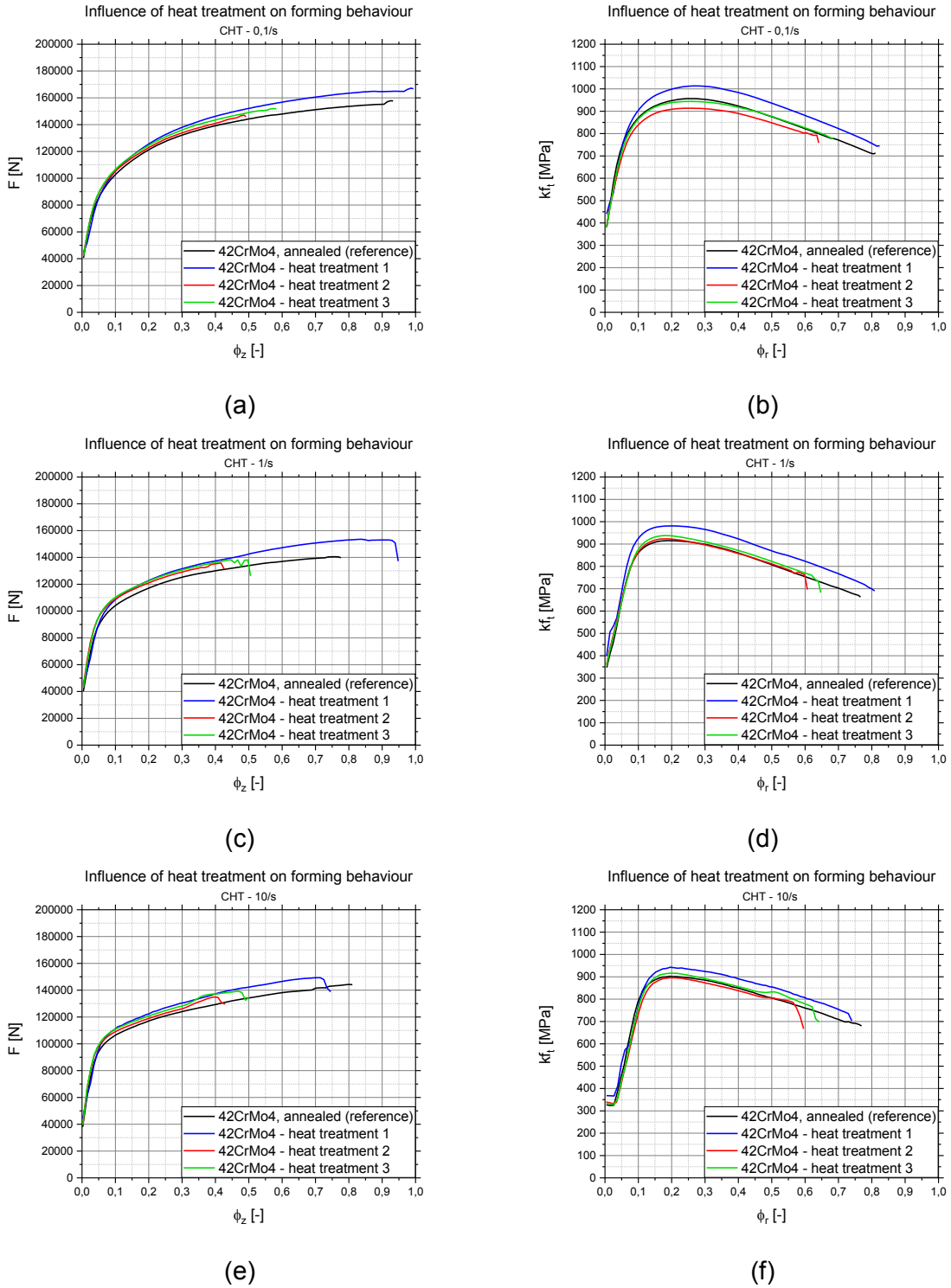

Figure 78: Influence of heat treatment on the forming behaviour – 42CrMo4
(a), (c), (e) punch force F plotted against strain in punch direction φ_z with $\dot{\boldsymbol{\varphi}} = \frac{0{,}1}{s}, \frac{1}{s}$ ***and*** $\frac{10}{s}$,
(b), (d), (f) tangential flow stress $k_{f,t}$ plotted against radial strain φ_r with $\dot{\boldsymbol{\varphi}} = \frac{0{,}1}{s}, \frac{1}{s}$ ***and*** $\frac{10}{s}$

Table 22: CHT – influence of heat treatments – 42CrMo4, annealed (Q&T steel)

Material	$\dot{\varphi}$ [1/s]	$\varphi_{z,max}$ [MPa]	F_{max} [N]	$\varphi_{r,max}$ [-]	$k_{f,t}$ [MPa]	φ_r [-]	$k_{f,t,max}$ [MPa]
Reference	0,1	0,93	157600	0,81	712	0,27	957
	1	0,78	139800	0,76	663	0,19	915
	10	0,81	144100	0,77	680	0,21	901
Heat treatment 1	0,1	0,99	166800	0,82	745	0,28	1013
	1	0,95	137200	0,81	690	0,20	981
	10	0,75	138800	0,74	703	0,20	943
Heat treatment 2	0,1	0,49	145900	0,64	758	0,26	913
	1	0,43	131300	0,61	696	0,19	923
	10	0,43	129700	0,60	667	0,20	896
Heat treatment 3	0,1	0,58	151700	0,68	779	0,26	944
	1	0,51	126200	0,65	683	0,19	938
	10	0,50	134500	0,64	698	0,21	916

The cold heading test (CHT) can be used as a precise tool for the investigation of different influences on the forming behaviour of different materials. The impact of strain rate, microstructure as well as material concepts is shown in great detail with comparable results to standard experimental methods such as tensile testing. Therefore, the CHT can be used to experimentally review materials used for the application of cold heading operations. To conclude the investigation of the usability of the newly developed testing method, different steel grades generally used for the manufacturing of high strength screws and fasteners are examined in the following chapter.

7.4. Investigation of steel grades used for cold forming operations

In the manufacturing of screws and fasteners by cold forming operations, a wide variety of steel grades are used. In this work, the cold heading test (CHT) has been used for the characterization of two steel types, which are deployed for the production of high strength components, the precipitation-hardening ferritic-pearlitic (PH-FP) steel 27MnSiVS6, in as-rolled condition and the quenching and tempering (Q & T) steel 42CrMo4, in annealed condition. The accuracy of the CHT in the depiction of the formability of materials has been shown in the previous chapters, therefore, the testing setup is used to characterize the forming behaviour of a wide range of steels intended for cold heading, the composition of which are shown in Table 23. The chemical composition was measured using an arc spectrometer at the chair of non-ferrous metallurgy (NEM) at the MU Leoben.

Table 23: Composition of materials used for investigations (AR…as-rolled, A…annealed, P…patented)

Material	C wt%	Si wt%	Mn wt%	P wt%	S wt%	Cr wt%	Ni wt%	Mo wt%	V wt%	B wt%
Reference materials										
27MnSiVS6, AR	0,30	0,68	1,25	0,01	0,02	0,15	0,04	0,00	0,11	0,000
42CrMo4, A	0,38	0,07	0,73	0,01	0,01	1,04	0,03	0,18	0,00	0,000
Materials in as-rolled (AR) condition										
23MnB4, AR	0,26	0,12	0,97	0,01	0,01	0,33	0,17	0,00	-	0,004
30MnB4, AR	0,31	0,13	0,95	0,01	0,01	0,25	0,04	-	-	0,004
30MoB1, AR	0,30	0,06	0,85	0,01	0,01	0,20	0,05	0,09	-	0,002
32CrB4, AR	0,32	0,08	0,74	0,01	0,01	1,20	0,03	-	0,00	0,003
Materials in annealed (A) condition										
32CrB4, A	0,32	0,08	0,74	0,01	0,01	1,20	0,03	-	0,00	0,003
46CrMoV4-7, A	0,40	0,23	0,80	0,01	0,01	0,99	0,52	0,92	0,12	0,001
Material in patented (P) condition										
C82, P	0,81	0,26	0,63	0,01	0,01	0,01	0,02	-	-	0,000

The materials investigated are split into four groups: (i) reference materials which have been used for the main experiments in this work, (ii) steels in as-rolled condition, which contains case-hardening steels and Q & T-steels with alloyed boron (B) for increased hardenability, (iii) steels in annealed condition and (iv) a patented high-strength pearlitic steel used for wire drawing to test the limits of the CHT [1; 2].

The cold heading steels are investigated using tensile tests with round specimen conforming to standard DIN 50125 (ISO 6892-1), method B, to determine the ultimate tensile stress (UTS) [103]. Additionally, the Vickers hardness values conforming to standard DIN EN ISO 6507-1

are determined using a EMCO-Test unit at the chair of metal forming at MU Leoben [139]. The measured UTS and hardness values, as well as the grain size measured using optical light microscopy and Olympus Stream analysing software are shown in Table 24. The steel grades are assorted by UTS from highest to lowest. The grain size of annealed and patented materials cannot be determined using optical light methodology but can be measured using, e.g. EBSD imaging.

Table 24: Overview of hardness and strength values of the investigated materials

Material	Hardness [HV]	UTS [MPa]	Grain size GS [µm]
C82, P	354,4 ± 1,9	1209	patented
27MnSiVS6, AR	229,6 ± 2,2	780	5,9
46CrMoV4-7, A	196,6 ± 1,3	679	annealed
32CrB4, AR	186,6 ± 2,3	665	6,9
30MnB4, AR	176,2 ± 2,2	639	7,3
30MoB1, AR	187,0 ± 1,0	633	6,8
23MnB4, AR	158,2 ± 2,8	581	7,5
42CrMo4, A	150,8 ± 0,8	561	annealed
32CrB4, A	130,0 ± 1,2	493	annealed

After determination of the material properties using uniaxial tensile testing, the materials are prepared for cold heading testing, as described in chapter 4. The samples are tested using the w + b LFV-T setup at a strain rate of $\dot{\varphi} = \frac{0,1}{s}$, and the experimental parameters specified in chapter 4.2. The results of the tests are shown in Figure 79, where the punch force F is plotted against the strain in punch direction φ_Z. The calculated values for flow stress $k_{f,t}$ and radial strain φ_r are shown in Figure 80. The patented, fully pearlitic steel C82 displays the lowest formability and the highest necessary punch force. However, in the chosen testing setup (w + b LFV-T) it is not possible to reach failure of the material, as the maximum punch force is capped at ~200 kN. But, compared with the other investigated materials, the cold heading test shows a good correlation with the uniaxial tensile test, with C82, patented showing the highest strength and lowest formability, and 32CrB4, annealed condition with the highest ductility and lowest recorded deformation force.

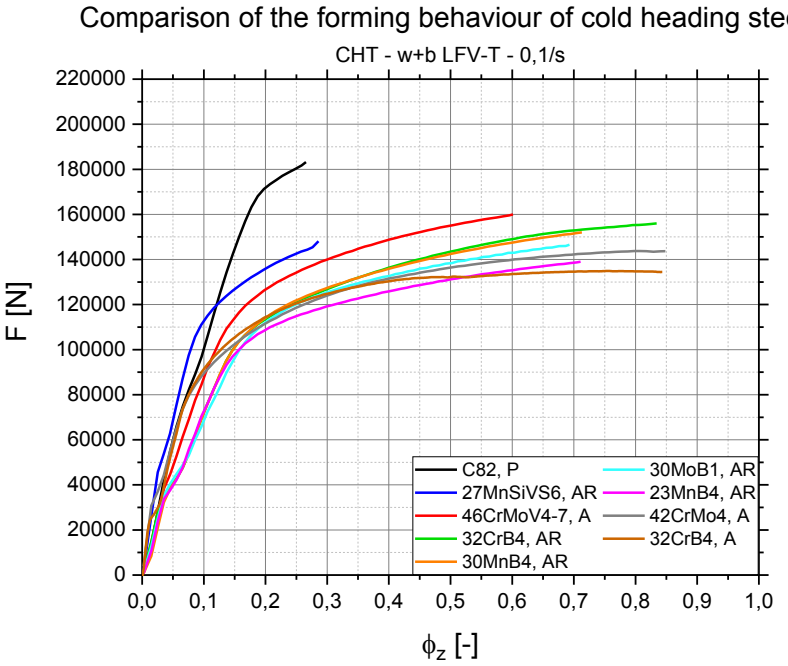

Figure 79: Cold heading test – comparison of materials used for cold forming, punch force F plotted against strain in punch direction φ_z

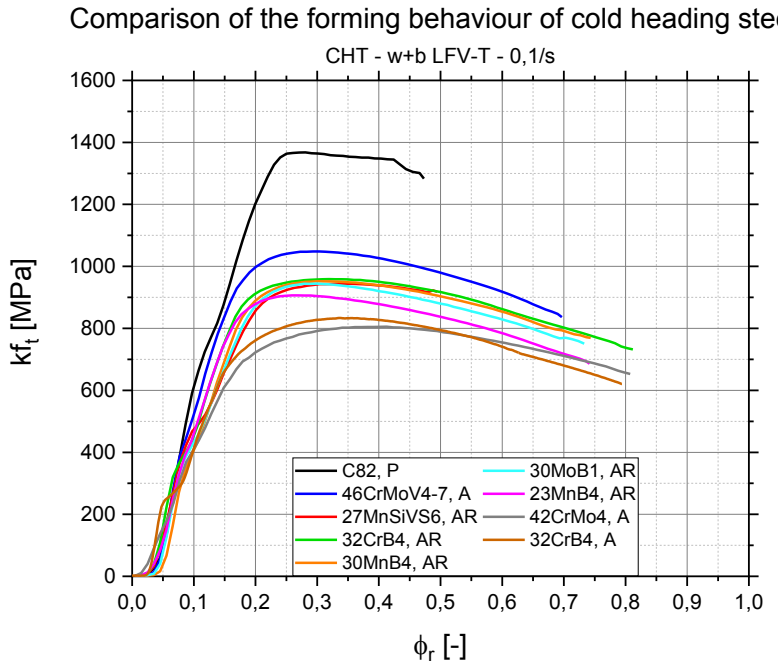

Figure 80: Cold heading test – comparison of materials used for cold forming, tangential stress $k_{f,t}$ plotted against radial strain φ_r

A detailed summary of the measured and calculated force/stress and strain values compared to the UTS recorded by tensile testing is shown in Table 25. The results of the cold heading experiments can be evaluated by the influence of (i) the microstructure or heat treatment and (ii) the alloyed elements of the investigated steel grades. The fully pearlitic grain structure of

C82, patented is apparent due to the highest measured UTS as well as the highest force/stress values, as well as the lowest strain. Ferritic-pearlitic steel grades in as rolled condition show a decreasing maximum force *F* and strain $k_{f,t,max}$ with decreasing carbon content. The precipitation-hardening ferritic pearlitic (PH-FP) material 27MnSiVS6, displays a diverging behaviour with an overall reduced formability, due to the alloying of V [1]. Annealed materials show the highest formability and lowest maximum strain, due to the homogeneous grain structure with globular formed Fe_3C dispersions. This behaviour of homogeneous deformation has also been illustrated in the in-situ experiments in chapter 5. When the influence of alloyed elements is examined, steel types alloyed with chromium (42CrMo4 and 32CrB4) show the highest formability followed by systems alloyed with manganese (Mn) and molybdenum (Mo). This results show the accuracy of the cold heading test in determining the workability of materials and a comparability to standard testing methods, for example tensile testing.

Table 25: Summary of the cold heading test results

Material	$\varphi_{z,\,max}$ [-]	F_{max} [N]	$\varphi_{r,max}$ [-]	$k_{f,t}$ [MPa]	φ_r [-]	$k_{f,t,max}$ [MPa]	UTS [MPa]
C82, P	0,27	183177	0,47	1283	0,28	1368	1209
27MnSiVS6, AR	0,29	148126	0,49	918	0,35	944	780
46CrMoV4-7, A	0,60	159978	0,70	836	0,29	1048	679
32CrB4, AR	0,83	155990	0,81	732	0,32	959	665
30MnB4, AR	0,71	152005	0,74	769	0,30	952	639
30MoB1, AR	0,69	146651	0,73	751	0,30	944	633
23MnB4, AR	0,71	138984	0,74	686	0,27	907	581
42CrMo4, A	0,85	143687	0,81	653	0,41	805	561
32CrB4, A	0,84	134453	0,79	621	0,34	834	493

In conclusion, the conducted experiments indicate high accuracy of the developed cold heading test in depicting the formability of materials. The influence of different deformation velocities, variations in microstructure and alloying concepts can be represented using a simple experimental setup and sample preparation. Additionally, the CHT enables comparison of the results with standard testing methods such as tensile or compression testing, with the advantage of presenting an application-oriented testing setup. Therefore, the cold heading test presents the possibility of a comparison and evaluation of workability of different materials and microstructural properties. These test characteristics support the development of new alloying concepts for materials intended for cold forming operations with application-oriented formability data.

8. Conclusion

In this work, cold heading materials used in the production of screws and fasteners, have been investigated concerning their deformation behaviour. To achieve a thorough characterisation of the influences, such as microstructure, strain rate and heat treatment, several novel approaches have been utilised.

To determine the effect of microstructure and material concept at a universal scale, standard testing methods, tensile and compressive tests, are conducted in combination with an innovative method of measuring strains at a microstructural level using digital image correlation (DIC). On an application-oriented scale, a new and optimized testing setup simulating the stresses and strains occurring during cold heading operations, the cold heading test (CHT), is used. In combination, these methods enable a precise description of material behaviour during deformation during cold forming operations, e.g. lateral extrusion. An overview of the applied methods is shown in Figure 81.

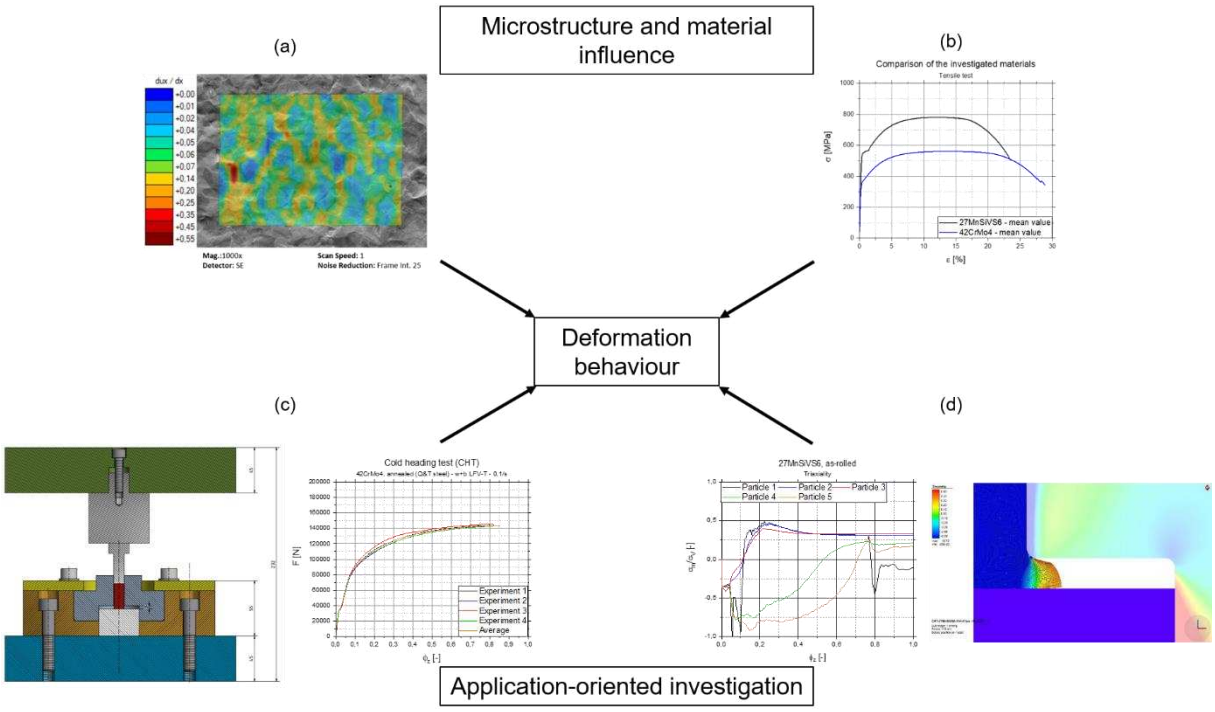

Figure 81: Overview of the investigation of deformation behaviour of materials –
(a) DIC measurements, (b) tensile testing, (c) cold heading testing (CHT), (d) FE-simulation

The steel grades mainly used in this work are 27MnSiVS6, a precipitation hardening ferritic-pearlitic (PH-FP) steel, in as-rolled condition, and 42CrMo4, a quenching and tempering (Q&T) steel, annealed to examine the accuracy of the experimental methods. The in-situ tensile methods using DIC enable the characterization of the influence of microstructure on the deformation behaviour. The ferritic-pearlitic material displays a strong localization of strains mainly in ferrite areasa, with the annealed steel grade developing a more homogeneous strain

distribution over the investigated area. Due to these results, the influence of localization effects on the formability can be evaluated using simple sample surface preparation methods.

However, to depict the workability as well as the damaging behaviour of materials at a macroscopic scale, a cold heading test method, which reproduces the final forming step in cold forming operations, has been developed and optimized. This experimental setup allows for investigation of the influence of multi-axial stress states as well as surface conditions during deformation. To support the experimental investigations of the CHT, finite element (FE) simulation of the testing setup is built up to better describe the stress-state during deformation.

The cold heading test is used for the characterization of a wide array of materials with different alloying concepts, microstructures as well as heat treatments. The results enable the depiction of formability of different steel grades and comparison with standard testing methods, for example tensile and compression tests. However, with the advantage of depicting stress-states and surface influences during industrial applications, this newly developed setup, in combination with the investigation of materials on a microstructural level using DIC methods, enables the characterization of formability of materials intended for cold heading. Due to the optimized experimental setup and simple sample preparation, the CHT supports the development of new material types intended for cold forming operations.

Literature

[1] W. Bleck, E. Moeller: Handbuch Stahl, Hanser, München, 2018.

[2] ASM International Handbook Committee: Properties and Selection, ASM International, 1990.

[3] J. R. Davis: Metals handbook, ASM International, Materials Park, OH., 1998.

[4] ASM International Handbook Committee: Metals Handbook - Desk Edition.

[5] Deutsches Institut für Normung: DIN EN 10060:2004-02, Warmgewalzte Rundstäbe aus Stahl- Maße, Formtoleranzen und Grenzabmaße; Deutsche Fassung EN_10060:2003.

[6] W. P. Krejdovsky, D. M. Jones, B. V. Kiefer: Improved wire rod properties resulting from controlled cooling in modern water box and Stelmor® conveyor cooling system. Wire Journal International, 40, S. 56–61, 2007.

[7] K. G. Swift, J. D. Booker: Manufacturing Process Selection Handbook, Butterworth-Heinemann, Oxford, 2013.

[8] Carpenter Specialty Alloys: Heading Hints, 2001, https://www.cartech.com/globalassets/literature-files/carpenterheadinghintscoldforming.pdf.

[9] R. Barrett: Getting a grip on fasteners. Metal Bulletin Monthly, 27, S. 38–43, 1997.

[10] A. Sabih, J. Nemes: Internal ductile failure mechanisms in steel cold heading process. Journal of Materials Processing Technology, 209, S. 4292–4311, 2009.

[11] F. Klocke: Manufacturing Processes 4 - Forming, Springer, Heidelberg, 2013.

[12] G. Gottstein: Physikalische Grundlagen der Materialkunde, Springer, Berlin [u.a.], 2007.

[13] G. E. Dieter, H. A. Kuhn, S. Semiatin: Handbook of workability and process design, ASM International, Materials Park, 2003.

[14] R. Sowerby, N. Chandrasekaran: The cold upsetting and free surface ductility of some commercial steels. Journal of Applied Metalworking, 3, S. 257–263, 1984.

[15] H. Jafarzadeh, G. Faraji, A. F. Dizaji: Analysis of lateral extrusion of gear-like form parts. Journal of Mechanical Science and Technology, 26, S. 3243–3252, 2012.

[16] G. Brethenoux, E. Bourgain, G. Pierson, et al.: Cold forming processes. Journal of Materials Processing Technology, 60, S. 555–562, 1996.

[17] Y. Fu, H. Yu: Application of mathematical modeling in two-stage rolling of hot rolled wire rods. Journal of Materials Processing Technology, 214, S. 1962–1970, 2014.

[18] R. Sowerby, I. O'Reilly, N. Chandrasekaran, et al.: Materials Testing for Cold Forging. Journal of Engineering Materials and Technology, 106, S. 101, 1984.

[19] F. Schongen, F. Klocke, P. Mattfeld, et al.: FEM/BEM Simulation of Cold Forging Process Considering Press-tool-workpiece Interaction. Procedia Engineering, 81, S. 2403–2408, 2014.

[20] R. Kuziak, S. Zajac, R. Kawalla, et al.: Cold heading quality low-carbon ultra-high-strength bainitic steels (Coheadbain), RFCS publications, Brussels, 2008.

[21] N. E. Dowling: Mechanical Behavior of Materials, Pearson Education Limited, Essex, 2013.

[22] H.-J. Bargel, G. Schulze: Werkstoffkunde, Springer, Berlin [u.a.], 2012.

[23] H. Berns, W. Theisen: Eisenwerkstoffe - Stahl und Gusseisen, Springer-Verlag Berlin Heidelberg, Berlin [u.a.], 2008.

[24] D. Breuer: Bestimmung des Formänderungsvermögens bei der Kaltmassivumformung, Aachen.

[25] D. Banabic: Formability of metallic materials, Springer, Berlin, London, 2000.

[26] F. Roters: Crystal plasticity finite element methods in materials science and engineering, Wiley-VCH, Weinheim, 2010.

[27] G. E. Taylor, C. F. Elam: Bakerian Lecture: The distortion of an aluminium crystal during a tensile test. Mathematical, Physical and Engineering Sciences, 102, S. 643–667, 1923.

[28] G. I. Taylor: Plastic strain in metals. Journal of the Institute of Metals, 62, S. 307–324, 1938.

[29] R. Hill: Generalized constitutive relations for incremental deformation of metal crystals by multislip. Journal of Mechanics and Physics in Solids, 14, S. 95–102, 1966.

[30] J. Segurado, R. A. Lebensohn, J. LLorca: Computational Homogenization of Polycrystals. Advances in Applied Mechanics, 51, S. 1–114, 2018.

[31] R. Hill, J. R. Rice: Constitutive analysis of elastic-plastic crystals at arbitrary strain. Journal of Mechanics and Physics in Solids, 20, S. 401–413, 1972.

[32] D. Peirce: Shear band bifurcations in ductile single crystals. Journal of the Mechanics and Physics of Solids, 31, S. 133–153, 1982.

[33] C. Tome, G. R. Canova, U. F. Kocks, et al.: The relation between macroscopic and microscopic strain hardening in F.C.C. polycrystals. Acta Materialia, 32, S. 1637–1653, 1984.

[34] J. L. Bassani, WuT.-Y.: Latent hardening in single crystals. II. Analytical characterization and predictions. Mathematical, Physical and Engineering Sciences, 435, S. 21–41, 1991.

[35] G. Cailletaud: A micromechanical approach to inelastic behaviour of metals. International Journal of Plasticity, 8, S. 55–73, 1992.

[36] L. Meríc, P. Poubanne, G. Cailletaud: Single Crystal Modeling for Structural Calculations: Part 1 - Model Presentation. Engineering Materials and Technology, 113, S. 162–170, 1991.

[37] E. Orowan: Zur Kristallplastizität. Zeitschrift für Physik, 89, S. 605–613, 1934.

[38] J. l. J.P. Hirth: Theory of dislocations, Wiley & Sons, New York, NY, 1982.

[39] U. F. Kocks, A. S. Argon, M. F. Ashby: Thermodynamics and kinetics of slip. Progress in Materials Science, 19, S. 1–291, 1975.

[40] Y. Estrin, H. Mecking: A unified phenomenological description of work hardening and creep based on one-parameter models. Acta Metallurgica, 32, S. 57–70, 1984.

[41] E. O. Hall: The Deformation and Ageing of Mild Steel: III Discussion of Results. Proceedings of the Physical Society B, 64, S. 747–753, 1951.

[42] N. J. Petch: The cleavage strength of polycrystals. Journal of the Iron and Steel Institute, 174, S. 25–28, 1953.

[43] J. Nye: Some geometrical relations in dislocated crystals. Acta Metallurgica, 1, S. 153–162, 1953.

[44] M. F. Ashby: The deformation of plastically non-homogenous materials. Philosophical Magazine, 21, S. 399–424, 1970.

[45] A. Ma, F. Roters, D. Raabe: A dislocation density based constitutive model for crystal plasticity FEM including geometrically necessary dislocations. Acta Materialia, 54, S. 2169–2179, 2006.

[46] C. F. Niordson, J. W. Kysar: Computational strain gradient crystal plasticity. Journal of the Mechanics and Physics of Solids, 62, S. 31–47, 2014.

[47] S. Mahajan, D. F. Williams: Deformation Twinning in Metals and Alloys. International Metallurgical Reviews, 18, S. 43–61, 1973.

[48] S. R. Kalidindi: Incorporation of deformation twinning in crystal plasticity models. Journal of the Mechanics and Physics of Solids, 46, 267-271, 273-290, 1998.

[49] J. Betten: Kontinuumsmechanik, Springer, Berlin, 2001.

[50] v. R. Mises: Mechanik der festen Körper in plastisch-deformablen Zustand. Nachr. d. Kgl. Ges. Wiss. Göttingen, 4, S. 582–592, 1913.

[51] H. Stenger: Über die Abhängigkeit des Formänderungsvermögens metallischer Stoffe vom Spannungszustand, Aachen.

[52] A. Amine Benzerga, J.-B. Lebland: Ductile Fracture by Void Growth to Coalescence. Advances in Applied Mechanics, 44, S. 169–305, 2010.

[53] H. Pugh: Mechanical behaviour of materials under pressure, Elsevier, Amsterdam, 1970.

[54] C. Silva, L. M. Alves, C. V. Nielsen, et al.: Failure by fracture in bulk metal forming. Journal of Materials Processing Technology, 215, S. 287–298, 2015.

[55] T. Nishimura, T. Sato, K. Hoke, et al.: A method for the evaluation of lubrication using injection upsetting. Journal of Materials Processing Technology, 53, S. 712–725, 1995.

[56] T. Mizuno, T. Mizuno, K. Kitamura: An experiment on injection upsetting. Journal of Materials Processing Technology, 96, S. 234–239, 1999.

[57] Y. Çan, T. Altınbalık, H. E. Akata: A study of lateral extrusion of gear like elements and splines. Journal of Materials Processing Technology, 166, S. 128–134, 2005.

[58] T. Altinbalik, Y. Can: An experimental study of lateral extrusion of splines. Materials & Design, 27, S. 727–734, 2006.

[59] C. M. A. Silva, P. A. R. Rosa, P. A. F. Martins: Innovative Testing Machines and Methodologies for the Mechanical Characterization of Materials. Experimental Techniques, 40, S. 569–581, 2016.

[60] S. Guk, R. Kawalla: Prozessnahe Beurteilung der Umformbarkeit beim Kaltfließpressen. Massivumformung, 3, S. 64–68, 2017.

[61] A. Pineau, A. A. Benzerga, T. Pardoen: Failure of metals I. Acta Materialia, 107, S. 424–483, 2016.

[62] M. W. Garrison, N. R. Moody: Ductile Fracture. Journal of Physical Chemistry of Solids, 48, S. 1035–1074, 1987.

[63] A. Sancho, M. Cox, T. Cartwright, et al.: Experimental techniques for ductile damage characterisation. Procedia Structural Integrity, 2, S. 966–973, 2016.

[64] M. N. Shabrov, C. L. Briant, A. Needleman, et al.: Void nucleation by inclusion cracking. Metallurgical and Materials Transactions A, 35, S. 1745–1755, 2004.

[65] H. Li, M. W. Fu, J. Lu, et al.: Ductile fracture. International Journal of Plasticity, 27, S. 147–180, 2011.

[66] M. G. Cockroft, D. J. Latham: Ductility and Workability of Metals. Journal of the Institute of Metals, 96, S. 33–39, 1968.

[67] M. Ayada, T. Higashino, K.-I. Mori: Central bursting in extrusion of inhomogenous materials. Proceeding sof the Second International Conference on Technology of Plasticity, 2, S. 552–558, 1987.

[68] A. M. Freudenthal: The Inelastic Behavior of Engineering Materials and Structures. Alfred M. Freudenthal. John Wiley & Sons Inc. New York. 1950. 587 pp. Figures. $7.50 net (60s.). The Journal of the Royal Aeronautical Society, 55, S. 657, 1951.

[69] M. OYANE: Criteria of Ductile Fracture Strain. Bulletin of JSME, 15, S. 1507–1513, 1972.

[70] J. Lemaitre, H. Lippmann: A Course on damage mechanics, Springer, Berlin, op. 1996.

[71] F. McClintock: A Criterion for Ductile Fracture by the Growth of Holes. Advances in Applied Mechanics, 35, S. 363–371, 1968.

[72] S. Hao, W. Brocks: The Gurson-Tvergaard-Needleman-model for rate and temperature-dependent materials with isotropic and kinematic hardening. Computational Mechanics, 20, S. 34–40, 1997.

[73] C. C. Chen, S. I. Oh, S. Kobayashi: Ductile Fracture in Axisymmetric Extrusion and Drawing—Part 1. Journal of Engineering for Industry, 101, S. 23–35, 1979.

[74] J. R. Rice, D. M. Tracey: On the ductile enlargement of voids in triaxial stress fields∗. Journal of the Mechanics and Physics of Solids, 17, S. 201–217, 1969.

[75] M. OYANE, T. Sato, K. Okimoto, et al.: Criteria for ductile fracture and their applications. Journal of Mechanical Working Technology, 4, S. 65–81, 1980.

[76] A. L. Gurson: Continuum Theory of Ductile Rupture by Void Nucleation and Growth: Part I - Yield Criteria and Flow Rules for Porous Ductile Media. J. Eng. Mater. Technol, 99, S. 2–15, 1976.

[77] V. Tvergaard: On localization in ductile materials containing spherical voids. International Journal of Fracture, 18, S. 237–252, 1982.

[78] V. Tvergaard, A. Needleman: Analysis of the cup-cone fracture in a round tensile bar. Acta Metallurgica, 32, S. 157–169, 1984.

[79] V. Tvergaard: Material Failure by Void Growth to Coalescence. Advances in Applied Mechanics, 27, S. 83–151, 1990.

[80] A. Needleman, V. Tvergaard: An analysis of dynamic, ductile crack growth in a double edge cracked specimen. International Journal of Fracture, 49, S. 41–67, 1991.

[81] S. Münstermann, U. Prahl, W. Bleck: Numerical Modelling of Toughness and Failure Processes in Steel Structures. steel research international, 78, S. 224–235, 2007.

[82] V. Uthaisangsuk, U. Prahl, W. Bleck: Micromechanical modelling of damage behaviour of multiphase steels. Computational Materials Science, 43, S. 27–35, 2008.

[83] P. Stögner: Modelling of Damage during Cold Heading of Metallic Materials. XXXVIII. Verformungskundliches Kolloquium der Umformtechnik, 38, S. 118–122, 2019.

[84] E. Siebel, S. Schwaigerer: Zur Mechanik des Zugversuchs. Archiv für das Eisenhüttenwesen, 19, S. 145–152, 1948.

[85] M. A. Sutton, W. J. Wolters, W. H. Peters, et al.: Determination of displacements using an improved digital correlation method. Image and Vision Computing, 1, S. 133–139, 1983.

[86] T. C. Chu, W. F. Ranson, M. A. Sutton: Applications of digital-image-correlation techniques to experimental mechanics. Experimental Mechanics, 25, S. 232–244, 1985.

[87] J. Hammacher, M. Dost, B. Seiler, et al.: Correlation based local measurement of small CTE for high temperature power electronics packaging. IEEE International Conference on Computer Science and Automation Engineering, S. 1–4, 2011.

[88] P. F. Luo, Y. J. Chao, M. A. Sutton, et al.: Accurate measurement of three-dimensional deformations in deformable and rigid bodies using computer vision. Experimental Mechanics, 33, S. 123–132, 1993.

[89] M. A. Sutton, N. Li, D. C. Joy, et al.: Scanning Electron Microscopy for Quantitative Small and Large Deformation Measurements Part I. Experimental Mechanics, 47, S. 775–787, 2007.

[90] M. A. Sutton, N. Li, D. Garcia, et al.: Scanning Electron Microscopy for Quantitative Small and Large Deformation Measurements Part II. Experimental Mechanics, 47, S. 789–804, 2007.

[91] A. D. Kammers, S. Daly: Digital Image Correlation under Scanning Electron Microscopy. Experimental Mechanics, 53, S. 1743–1761, 2013.

[92] S.-H. Joo, J. K. Lee, J.-M. Koo, et al.: Method for measuring nanoscale local strain in a dual phase steel using digital image correlation with nanodot patterns. Scripta Materialia, 68, S. 245–248, 2013.

[93] A. Guery, F. Latourte, F. Hild, et al.: Characterization of SEM speckle pattern marking and imaging distortion by digital image correlation. Measurement Science and Technology, 25, S. 15401, 2014.

[94] A. D. Kammers, S. Daly: Small-scale patterning methods for digital image correlation under scanning electron microscopy. Measurement Science and Technology, 22, S. 125501, 2011.

[95] W. A. Scrivens, Y. Luo, M. A. Sutton, et al.: Development of Patterns for Digital Image Correlation Measurements at Reduced Length Scales. Experimental Mechanics, 47, S. 63–77, 2007.

[96] T. E. J. Edwards, F. Di Gioacchino, H. P. Springbett, et al.: Stable Speckle Patterns for Nano-scale Strain Mapping up to 700 °C. Experimental mechanics, 57, S. 1469–1482, 2017.

[97] P. Löbmann, R. Jahn, S. Seifert, et al.: Inorganic Thin Films Prepared from Soluble Powders and Their Applications. Journal of Sol-Gel Science and Technology, 19, S. 473–477, 2000.

[98] A. D. Kammers, S. Daly: Self-Assembled Nanoparticle Surface Patterning for Improved Digital Image Correlation in a Scanning Electron Microscope. Experimental Mechanics, 53, S. 1333–1341, 2013.

[99] K. Lange, M. Kammerer, K. Pöhlandt, et al.: Fließpressen, Springer, Berlin [u.a.], 2008.

[100] M. P. Groover: Fundamentals of Modern Manufacturing: Materials, Processes, and Systems, Wiley & Sons, 2020.

[101] International Organization for Standardization: DIN EN ISO 898-1.

[102] E. Hornbogen, G. Eggeler, E. Werner: Werkstoffe, Springer-Verlag Berlin Heidelberg, Heidelberg, 2012.

[103] Deutsches Institut für Normung: DIN EN ISO 6892-1, 2020.

[104] T. Emde: Mechanisches Verhalten metallischer Werkstoffe über weite Bereiche der Dehnung, der Dehnrate und der Temperatur, Mainz, Aachen, 2009.

[105] A. Gilat, X. Wu: Plastic deformation of 1020 steel over a wide range of strain rates and temperatures. International Journal of Plasticity, 13, S. 611–632, 1997.

[106] M. Knobloch, J. Pauli, M. Fontana: Influence of the strain-rate on the mechanical properties of mild carbon steel at elevated temperatures. Materials & Design, 49, S. 553–565, 2013.

[107] B. Buchmayr, T. Hatzenbichler, R. Kienreich, et al.: Werkstoff- und verfahrenstechnische Optimierung bei der Herstellung hochfester Schrauben. BHM (Berg- und Hüttenmännische Monatshefte), 153, S. 423–429, 2008.

[108] Deutsches Institut für Normung: DIN EN 10247:2017-09, Metallographische Prüfung des Gehaltes nichtmetallischer Einschlüsse in Stählen mit Bildreihen; Deutsche Fassung EN_10247:2017.

[109] V. Läpple: Wärmebehandlung des Stahls, Verl. Europa-Lehrmittel Nourney, Vollmer, Haan-Gruiten, 2003.

[110] E. Doege, B.-A. Behrens: Handbuch Umformtechnik, Springer-Verlag Berlin Heidelberg, [New York], 2007.

[111] Böhler Edelstahl: S390 Microclean High Speed Steel - Data Sheet, 2010, https://www.bohler-edelstahl.com/app/uploads/sites/92/2019/02/S390DE.pdf.

[112] N. Bay: The state of the art in cold forging lubrication. Journal of Materials Processing Technology, 46, S. 19–40, 1994.

[113] P. Groche, C. Müller, A. Jahn: Effects of the Tool Lubrication in Cold Forging. Tribology Letters, 53, S. 599–605, 2014.

[114] Dr. Sommer Werkstofftechnik GmbH: Overview, 2019, https://werkstofftechnik.com/.

[115] Bernd Pfleger: Influence of thermal processing on microstructure, strength and ductility of steels for cold heading applications, Leoben.

[116] A. Eggbauer, M. Lukas, P. Prevedel, et al.: Effect of Initial Microstructure, Heating Rate, and Austenitizing Temperature on the Subsequent Formation of Martensite and Its Microstructural Features in a QT Steel. steel research international, 90, S. 1800317, 2019.

[117] E. Doege, H. Meyer-Nolkemper, I. Saeed: Fliesskurvenatlas metallischer Werkstoffe, Hanser, München, op. 1986.

[118] Y. Luo, J. Ruff, R. Ray, et al.: Vapor-Assisted Remodeling of Thin Gold Films. Chemistry of Materials, 17, S. 5014–5023, 2005.

[119] F. Di Gioacchino, J. Quinta da Fonseca: Plastic Strain Mapping with Sub-micron Resolution Using Digital Image Correlation. Experimental Mechanics, 53, S. 743–754, 2013.

[120] B. Winiarski, G. S. Schajer, P. J. Withers: Surface Decoration for Improving the Accuracy of Displacement Measurements by Digital Image Correlation in SEM. Experimental Mechanics, 52, S. 793–804, 2012.

[121] W. Y. Kwong, W. Y. Zhang: Electron-beam assisted platinum deposition as a protective layer for FIB and TEM applications. IEEE International Symposium on Semiconductor Manufacturing, 2005, S. 469–471, 2005.

[122] J. Hoefnagels, M. van Maris, T. Vermeij: One-step deposition of nano-to-micron-scalable, high-quality digital image correlation patterns for high-strain in-situ multi-microscopy testing. Strain, 55, e12330, 2019.

[123] F. Lagattu, F. Bridier, P. Villechaise, et al.: In-plane strain measurements on a microscopic scale by coupling digital image correlation and an in situ SEM technique. Materials Characterization, 56, S. 10–18, 2006.

[124] F. Di Gioacchino, J. Quinta da Fonseca: An experimental study of the polycrystalline plasticity of austenitic stainless steel. International Journal of Plasticity, 74, S. 92–109, 2015.

[125] A. Tatschl, O. Kolednik: A new tool for the experimental characterization of micro-plasticity. Materials Science and Engineering: A, 339, S. 265–280, 2003.

[126] K. Unterweger, O. Kolednik: The local deformation behaviour of MMCs – an experimental study. Zeitschrift Metallkunde, 96, S. 1063–1068, 2005.

[127] A. J. Wilkinson, G. Meaden, D. J. Dingley: High resolution mapping of strains and rotations using electron backscatter diffraction. Materials Science and Technology, 22, S. 1271–1278, 2013.

[128] M. Calcagnotto, D. Ponge, E. Demir, et al.: Orientation gradients and geometrically necessary dislocations in ultrafine grained dual-phase steels studied by 2D and 3D EBSD. Materials Science and Engineering: A, 527, S. 2738–2746, 2010.

[129] M. Ojima, Y. Adachi, S. Suzuki, et al.: Stress partitioning behavior in an fcc alloy evaluated by the in situ/ex situ EBSD-Wilkinson method. Acta Materialia, 59, S. 4177–4185, 2011.

[130] C. Mansilla, V. Ocelík, J. T. M. de Hosson: A new methodology to analyze instabilities in SEM imaging. Microscopy and microanalysis : the official journal of Microscopy Society of America, Microbeam Analysis Society, Microscopical Society of Canada, 20, S. 1625–1637, 2014.

[131] C. B. Montgomery, B. Koohbor, N. R. Sottos: A Robust Patterning Technique for Electron Microscopy-Based Digital Image Correlation at Sub-Micron Resolutions. Experimental Mechanics, 59, S. 1063–1073, 2019.

[132] J. Maciejewski: The Effects of Sulfide Inclusions on Mechanical Properties and Failures of Steel Components. Journal of Failure Analysis and Prevention, 15, S. 169–178, 2015.

[133] B. Sarkar, B. K. Jha, R. Datta, et al.: Investigation into the Cracking of Cross Members During Forming. Journal of Failure Analysis and Prevention, 8, S. 81–83, 2008.

[134] Temmel, Cornelius, Karlsson, Birger, Torresvoll, Ketil, Fallqvist, Christopher: Investigation on Manganese Sulfide Inclusion Sizes in 50CrMo4 Steels by means of Fractography, Micrograph Analysis and Immersion Ultrasound. Praktische Metallographie, 46, S. 123–136, 2009.

[135] A. Benzerga, J. Besson, A. Pineau: Anisotropic ductile fracture Part I: experiments. Acta Materialia, 52, S. 4623–4638, 2004.

[136] A. Benzerga, J. Besson, A. Pineau: Anisotropic ductile fracture Part II: theory. Acta Materialia, 52, S. 4639–4650, 2004.

[137] P. Christiansen, C. V. Nielsen, P. A. Martins, et al.: Predicting the onset of cracks in bulk metal forming by ductile damage criteria. Procedia Engineering, 207, S. 2048–2053, 2017.

[138] H. Puschmann: Atlas zur Wärmebehandlung der Stähle. Band 2. Herausgegeben vom Max-Planck-Institut für Eisenforschung. In Zusammenarbeit mit dem Werkstoffausschuß des Vereins Deutscher Eisenhüttenleute. Verlag Stahleisen mbH, Düsseldorf 1972. Format DIN A 4. Ca. 20 S. mit 150 ganzseitigen Schaubildern und 424 Schliffbildern. Ganzln. DM 186,—, 24, 1973.

[139] Deutsches Institut für Normung: DIN EN ISO 6507-1, 2018.

Figures

Tables

Acronyms

CHT ..... cold heaing test

DIC ..... digital image correlation

DP-steel ..... dual phase steel

EBSD .. electron back scattered diffraction

EDM ..... electrical discharge machining

FEB ..... focused electron beam

FE ..... finite element

FIB ..... focused ion beam

PVD ..... physical vapour deposition

YSZ ..... yttria stabilised zirconium

A ..... Oyane-paramter

α ..... heat transfer coefficient

c_p ..... heat capacity

D* ..... maximum diameter CHT

η ..... triaxiality

f ..... void volume fraction

f* ..... modified damage parameter

F_{Punch} ..... punch force CHT

$h_{extruded}$ ..... extruded height CHT

k_f ..... flow stress

$k_{f,t}$ ..... tangential flow stress CHT

μ ..... friction coefficient

m ..... friction parameter

M* ..... maximum extruded lateral area

$\dot{\varphi}$ ..... strain rate

φ_r ..... radial strain CHT

φ_V ..... equivalent strain

φ_z ..... strain in punch direction CHT

ρ ..... density

$R_{p0,2}$ ..... yield strength

σ_1, σ_2, σ_3 ..... principal stresses

σ_m ..... hydrostatic stress

σ_V ..... equivalent stress

$V_{extruded}$ ..... extruded volume CHT